

**Exchange Interaction of Soft and Hard Magnetic Phases in  
Exchange-Spring Magnet of  $\text{Nd}_3\text{Tb}_1\text{Fe}_{76}\text{Cu}_{0.5}\text{Nb}_1\text{B}_{18.5}$**

M. Phil Thesis

By

MD. ABU HANIF ANSARI



**DEPARTMENT OF PHYSICS  
KHULNA UNIVERSITY OF ENGINEERING & TECHNOLOGY  
KHULNA-9203, BANGLADESH  
DECEMBER 2010**

**Exchange Interaction of Soft and Hard Magnetic Phases in  
Exchange-Spring Magnet of  $\text{Nd}_3\text{Tb}_1\text{Fe}_{76}\text{Cu}_{0.5}\text{Nb}_1\text{B}_{18.5}$**

M. Phil Thesis

By

Md. Abu Hanif Ansari  
Roll No: 0555551  
Session: July 2005



A THESIS SUBMITTED TO THE DEPARTMENT OF PHYSICS,  
KHULNA UNIVERSITY OF ENGINEERING & TECHNOLOGY IN  
PARTIAL FULFILLMENT OF THE REQUIREMENT FOR DEGREE  
OF MASTER OF PHILOSOPHY



**DEPARTMENT OF PHYSICS  
KHULNA UNIVERSITY OF ENGINEERING & TECHNOLOGY  
KHULNA-9203, BANGLADESH  
DECEMBER 2010**

KHULNA UNIVERSITY OF ENGINEERING & TECHNOLOGY  
DEPARTMENT OF PHYSICS  
CERTIFICATION OF THESIS WORK





A THESIS ON

**Exchange Interaction of Soft and Hard Magnetic Phases in Exchange-Spring Magnet of  $\text{Nd}_3\text{Tb}_1\text{Fe}_{76}\text{Cu}_{0.5}\text{Nb}_1\text{B}_{18.5}$**

By

**Md. Abu Hanif Ansari**

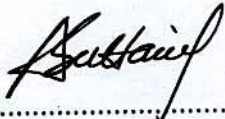
has been accepted as satisfactory in partial fulfillment for the degree of Master of Philosophy in Physics and certified that the student has demonstrated a satisfactory knowledge on the field covered by this thesis in an oral examination held on 18 December, 2010.

1. Prof. Dr. Shibendra Shekher Sikder  
Department of Physics  
Khulna University of Engineering & Technology  
  
.....  
Chairman & Supervisor
2. Dr. Sheikh Manjura Hoque  
Principal Scientific Officer  
Materials Science Division  
Atomic Energy Centre, Dhaka-1000  
.....  
Member & Co-Supervisor
3. Head  
Department of Physics  
Khulna University of Engineering & Technology  
  
.....  
Member
4. Prof. Dr. Mahbub Alam  
Department of Physics  
Khulna University of Engineering & Technology  
  
.....  
Member
5. Dr. Sheikh Md. Yunus  
Chief Scientific Officer  
Reactor and Neutron Physics Department  
Atomic Energy Research Establishment  
G. P. O. Box-3797, Savar, Dhaka  
Bangladesh  
  
.....  
Member ( External)



## CANDIDATE'S DECLARATION

It is here by declared that this thesis or any part of it has not been submitted elsewhere for the award of any degree or diploma.



.....  
Signature of the candidate

MD. ABU HANIF ANSARI

.....  
Name of the candidate





## CERTIFICATE

This is to certify that this thesis which the candidate has presented for M. Phil. Degree has been done by the candidate himself and does not contain any material extracted from else where or from a work published by anybody else. The work of this thesis has not been presented for another degree or diploma in any other University or Institute. No other person's work has been used without due acknowledgement .

*Abubakir*

.....  
Candidate

*Dr. M. A. M. M.*

.....  
Co-supervisor

*S. S. S.*

.....  
Supervisor

**DEDICATED**

TO

**ARTHY MONY & TOSHY MONY**

# CONTENTS

CANDIDATE'S DECLARATION	i
CERTIFICATE	ii
DEDICATION	iii
CONTENTS	iv
LIST OF FIGURES	viii
LIST OF SYMBOLS	xi
ACKNOWLEDGEMENTS	xii
ABSTRACT	xiv

## CHAPTER -1 INTRODUCTION

1.0 Introduction	1
------------------	---

## CHAPTER – 2 SOFT AND HARD EXCHANGE-BIASED SYSTEM

2.1 Introduction	6
2.2 The Exchange- Spring Magnet- One Dimensional Model	8
2.3 Effect of Exchange Coupling on the Macro-Magnetic Properties	13
2.3.1 Volume Fractions of Phases	14
2.3.2 Effect of Remanence Enhancement	15
2.3.3 Effect of Coercivity Reduction	16
2.3.4 Effect of Exchange Coupling on the Demagnetizing Curve	17
2.3.5 Spring – Magnet Behavior	17



2.4	Hysteresis loop and Demagnetization Curve	18
2.4.1	Saturation Remanence Ratio	20
2.4.2	Nucleation Field and Coercive Field	22
2.5	Magnetic Properties in the Optimum State	23

### **CHAPTER – 3 AN OVERVIEW OF NANOCRYSTALLINE MATERIALS**

3.1	History of amorphous and nanocrystalline materials	29
3.2	Kinds of nanocrystalline alloys	30
3.3	Fe-based Soft Nanocomposite Magnetic Material	32
3.3.1	Formation of Nanocrystalline State	33
3.3.2	Conditions for the formation of Nanocrystalline alloys	37
3.3.3	Grain Size and Coercive force of Nanocrystalline alloys	38
3.4	Various Kinds of Energies in the Formation of Magnetic Domains	39
3.4.1	Magnetostatic Energy	40
3.4.2	Magnetostrictive Energy	40
3.4.3	Anisotropy in Ferromagnetic Materials	40
3.4.4	Anisotropy energy	40
3.4.5	Zeeman Energy	40
3.5	Magnetization and Magnetic Induction	41
3.6	Susceptibility and Permeability	42
3.7	Theory of Permeability	42
3.8	Coercivity	44



3.9	Various Kinds of Magnetism	44
3.10	Origin of Magnetism (Quantum Mechanical View)	46
3.11	Magnetism of the Electron	48
3.12	Orbital Angular Momentum and Magnetic Moment	50

## CHAPTER – 4    PREPARATION OF NANOCRYSTALLINE ALLOY

4.1	Methods used for Preparation of Nano-crystalline Alloy	53
4.1.1	The Fast Cooling of the Melt	53
4.2	Sample Preparation	54
4.2.1	Master alloy Preparation	54
4.2.2	Preparation of ribbon by Melt Spinning Technique	55
4.3	Important Factors to Control the Thickness of Ribbons	56
4.4	Confirmation of Amorphousness of Ribbons	57
4.5	X-ray Diffraction (XRD)	57
4.5.1	X-ray Powder Method	58
4.5.2	Experimental Technique for X-ray Diffractometer	59
4.5.3	Analysis of XRD Data	62
4.6	Thermal Treatment of the Amorphous Ribbon	65
4.7	SQUID Magnetometers	65
4.7.1	Basic Components	66
4.7.1.1	Superconducting Magnet	66
4.7.1.2	Superconducting Detection Coil	67
4.7.1.3	SQUID	67
4.7.1.4	Superconducting Magnetic Shield	67
4.7.2	Applications	67



4.7.3	Improved Sensitivity	69
4.7.4	Extended Temperature Capability	69
4.7.5	Enhanced Thermometry and Temperature Sweep Operation	71
4.7.6	Software Control / Automation	71
4.8	Magnetization Measurement	72
4.8.1	Principle of Vibrating Sample Magnetometer	72
4.8.2	Description and brief Working Principle of Hirst VSM02	73
4.8.3	Working Principle of Vibrating Sample Magnetometer	75
4.9	Applications	77

## **CHAPTER – 5 RESULTS AND DISCUSSION**

5.1	X-ray Diffraction (XRD) Analysis	79
5.1.1	Time Annealing Effect of Structural Properties of $\text{Nd}_3\text{Tb}_1\text{Fe}_{76}\text{Cu}_{0.5}\text{Nb}_1\text{B}_{18.5}$	79
5.1.2	Effect of Different Annealing Time of Hysteresis Parameter of $\text{Nd}_3\text{Tb}_1\text{Fe}_{76}\text{Cu}_{0.5}\text{Nb}_1\text{B}_{18.5}$ at Constant Annealing Temperature	90

## **CHAPTER – 6 CONCLUSIONS** 102

## **REFERENCES** 105

## **PUBLICATION** 110

## LIST OF FIGURES

Fig-2.1	The history of $(BH)_{\max}$ since 1880 to 2000	6
Fig.2.2.	Schematic one-dimensional model of the microstructure and the exchange-coupled composite material	11
Fig.2.3	Typical demagnetization curves $M(H)$ (schematic).	19
Fig.-2.4	Demagnetization curve $M(H)$ measured after previous saturation in the opposite direction in the field $H = 1200 \text{ kA/m}$ on the alloy.	24
Fig.-2.5	Analysis of the total magnetization change, along the demagnetization curve $M(H)$	25
Fig.-2.6	Demagnetization curve $M(H)$	27
Fig.-2.7.	Coercive force $\mu_0 H_{CM}$ versus temperature $T$ .	28
Fig. 3.1	Microstructure and soft magnetic properties with the annealing temperature.	34
Fig.3.2	Schematic illustration of the formation of the nanocrystalline structure in Fe-Cu-Nb-Si-B alloys.	35
Fig. 3.4	Relation between grain diameter ( $D_g$ ) and coercive force ( $H_c$ ).	38
Fig.3.5	Spin arrangement in a crystal or domain illustrating (a) Paramagnetism, (b) Ferromagnetism, (c) Antiferromagnetism and (d) Ferrimagnetism.	45
Fig.-3.6	Splitting of energy levels of d orbital in an octahedral crystal field	51
Fig .-3.7	The shape of the $d_{x^2-y^2}$ and $d_{z^2}$ orbital.	52
Fig. 4.1	Vacuum arc Melting Machine	54
Fig. 4.2	Melt-Spinning Machine.	55
Fig.4.3	Bragg's diffraction pattern.	58

Fig.4.4	Reflection and Transmission geometry of powder diffraction	59
Fig. 4.5	Block diagram of the PHILIPS PW 3040 X'Pert PRO XRD system	60
Fig.4.6	A Philips PW 3040 X'Pert PRO X-ray diffractometer.	61
Fig.4.7	SQUID Magnetometer Principle.	66
Fig 4.8.	Cut view of a typical Superconducting pick-up coils	68
Fig 4.9	Second-order gradiometer magnet	68
Fig 4.10	Illustration of an RSO measurement with a small amplitude.	70
Fig. 4.11	Block diagram of a VSM system	74
Fig. 4.12	Hirst VSM system arrangements	74
Fig. 4.13	Vibration and measurement unit	74
Fig. 4.14	Block diagram of vibrating sample magnetometer	76
Fig. 5.1	X-ray diffraction patterns for the samples annealed at 923 K for the annealing time of 1 minute	80
Fig.5.2	X-ray diffraction patterns for the samples annealed at 923 K for the annealing time of 3 minute	81
Fig 5.3	X-ray diffraction patterns for the samples annealed at 923 K for the annealing time of 5 min.	82
Fig 5.4	X-ray diffraction patterns for the samples annealed at 923 K for the annealing time of 10 minute	83
Fig 5. 5	X-ray diffraction patterns for the samples annealed at 923 K for the annealing time of 20 minute	85
Fig 5.6	X-ray diffraction patterns for the samples annealed at 923 K for the annealing time of 1 minute	86
Fig 5.7	X-ray diffraction patterns for the samples annealed at 923 K for the annealing time of 5 minute	87
Fig 5.8	X-ray diffraction patterns for the samples annealed at 923 K for the annealing time of 10 minute	88



Fig 5. 9	X-ray diffraction patterns for the samples annealed at 923 K for the annealing time of 20 minute	89
Fig 5.10	Hysteresis loops for the samples annealed at 923 K for different annealing time	91
Fig 5.11	Hysteresis loops for the samples annealed at 923 K for different annealing time.	92
Fig 5.12	Comparison of hysteresis loops for the samples annealed at 923 K for annealing time of 5 minute	93
Fig 5.13	Comparison of hysteresis loops for the samples annealed at 923 K for annealing time of 10 minute	94
Fig 5. 14	Recoil hysteresis loops for the sample annealed at 923 K for 3 minutes.	98
Fig 5. 15	Variation of irreversible component of magnetization $D(H)$ with reverse field.	99
Fig 5.16	Variation of normalized recoil area with reverse field.	100

## LIST OF SYMBOLS

$T_C$  = Curie temperature.

$M_r$  = Remanent magnetization.

$M_s$  = Saturation magnetization.

$B$  = Magnetic Induction.

$\mu_0$  = Permeability in the free space.

$J_s$  = Saturation polarization.

$K$  = Magneto crystalline anisotropy constant.

$E_{ym}$  = Energy density of the soft phase.

$E_{yok}$  = Energy density of the hard phase.

$V_k$  = Volume of the Hard Phase (k-phase).

$V_m$  = Volume of the Soft Phase (m-phase).

XRD = X-ray diffraction.

FWHM = Full Width Half Maximum.

HRE = Heavy Rare earth Element.



## ACKNOWLEDGEMENTS

First and foremost, I take my opportunity to express my veneration and the heartfelt gratitude to my supervisor Professor **Dr. Shibendra Shekher Sikder**, Professor, Department of Physics, Khulna University of Engineering & Technology, Khulna, for his excellent supervision, salutary instruction and valuable suggestions throughout the progress of the work.

I pay my profound reverence and gratitude to my honorable Co-supervisor **Dr. Sheikh Manjura Hoque**, Principal Scientific Officer, Materials Science Division, Atomic Energy Centre, Dhaka, Bangladesh, for her constant encouragement, inspirations, indispensable guidance and brilliant suggestions in my thesis work and introducing me to the exciting field of the exchange spring magnetic properties of the material.

I convey my heartfelt thanks and gratitude to **A. K. M. Abdul Hakim**, Chief engineer and Head, Materials Science Division, Atomic Energy Centre, Dhaka, for his generous support in doing my work.

I am very much grateful to Professor Dr. Md. Mahbub Alam, Head, Department of Physics, Khulna University of Engineering & Technology, for allowing me as a thesis student and providing all the facilities related to this work.

Obviously, I am grateful to the director, Atomic Energy Centre, Dhaka, Bangladesh, for his kind permission to work in the laboratory of Materials Science Division at AECD, Bangladesh. I express sincere thanks to **Dr. Dilip Kumar Saha and Shireen Akhter**, Chief Scientific Officers and **Harinarayan Das**, Scientific Officer, and other personals of Materials Science Division, Atomic Energy Centre, Dhaka, for their generous support in doing measurements.

I gratefully acknowledge Mr. Md. Abdullah Elias Akhter & Dr. Jolly Sultana, Associate Professor, Department of Physics, and Mr. Enamul Hoque Bhuiyan & Mr.

Toriqul Islam, Lecturer, Department of Physics, Khulna University of Engineering & Technology for their co-operation and inspiration during this work.

I would like to extend my greatfulness specially to all of my Principals like Prof Saidul Hasan, Prof Shadhan Ranjan Ghosh, Prof. Nazir Uddin Ahmed and Prof Minoty Rani Mondal for their memorable cooperation and consistent encouragement.

I like to offer my gratitude to all my esteemed teachers of Department of Physics of Govt. B.L. College and also other Govt. Colleges in Khulna, specially to Saroaut Noor, Robiul Islam and Pritish Kumar Roy for their inspiration and cooperative attitude towards me.

I would like to thank all of my friends, well wishers , my mother and above all my beloved wife for giving me all kind of supports throughout my academic career.



## ABSTRACT

This thesis describes the experimental investigation of an ingot of composition  $\text{Nd}_3\text{Tb}_1\text{Fe}_{76}\text{Cu}_{0.5}\text{Nb}_1\text{B}_{18.5}$  was prepared by arc melting the constituent elements in an argon atmosphere. The purity and origin of the materials were more than above 99.99% from Johnson Mathey (Alfa Aesar). Amorphous ribbons were prepared from the ingot using a melt spin machine with a wheel speed of 25 m/s in an Ar atmosphere. The resulting ribbons were heat treated in an evacuated quartz tube of  $10^{-5}$  mbar pressure at different temperature and times to observe the effect of annealing condition on the magnetic properties. Differential Scanning Calorimetry was used to determine the crystallization temperature and X-ray diffraction ( $\text{CuK}\alpha$ ) was used to identify the phases present in the samples at different stages of the crystallization process. The magnetization measurements were made by Quantum Design MPMSXL5 Superconducting Quantum Interference Device (SQUID) magnetometer.

Hard Nanocomposite samples of the composition  $\text{Nd}_3\text{Tb}_1\text{Fe}_{76}\text{Cu}_{0.5}\text{Nb}_1\text{B}_{18.5}$  exhibited exchange spring behavior for a wide range of annealing temperature and time. Amorphous flakes have been synthesized by melt spinning system and annealed in the quartz tube under a vacuum of  $10^{-5}$  m bar pressure to observe the variation of magnetic properties with annealing condition. Highest value of coercivity around 4.76 kOe has been obtained for the sample annealed at 923 K for 5 minutes. Recoil hysteresis loops have been measured along the major demagnetization curve to observe the extent of springness of the sample annealed at 923 K for 3 minutes. Recoil loops are small having high recoil permeability. Irreversible component of magnetization was found to have very small value below the critical field.

Nd – deficient  $\text{Nd}_2\text{Fe}_{14}\text{B}/\text{Fe}_3\text{B}$  based nanocomposite alloys are characterized by their exchange-spring behavior resulting in remanent ratio greater than 0.5, which is highly desirable for permanent magnetic materials. Magnetic properties of exchange spring magnets are governed by the soft and hard magnetic phases that develop under appropriate annealing condition. High reduced remanence characteristics to these materials arise from exchange coupling of magnetic moments across the interface between two phases. Besides high reduced remanence such systems possess high energy product  $(\text{BH})_{\text{max}}$  and a reversible demagnetization curve, which has been called as exchange-spring behavior .

**CHAPTER -1**  
**INTRODUCTION**

---

## 1.0 INTRODUCTION

This thesis focuses on Fe-based soft and hard nanocomposite magnetic materials, nanostructured phase of  $\alpha$ -Fe(Si) evolved from amorphous precursor contain grains having dimension within 10-15nm. Nanomaterials are generally materials that can have one dimension, two dimensions or three dimensions and can be specified within a size of 100 nanometer (  $1\text{nm} = 10^{-9}\text{meter}$ ). Application area of inorganic nano particles are abrasives, catalysts, pigments/coatings, optical devices, electronic devices, magnetic and structural materials. In Fe-based soft nanocomposite magnetic materials nanograins are dispersed within the amorphous matrix. Since, nanograins are exchange-coupled through residual amorphous matrix, magnetic anisotropy is averaged out as a result of which permeability value is enhanced by the order of  $10^4$ , which is extraordinary soft compared to conventional soft magnetic materials <sup>(1.1-1.2)</sup>.

In Fe-based soft nanocomposite magnetic materials, temperature dependence of permeability is governed by the composition of the residual amorphous and nanostructured phases. When the sample is annealed below the crystallization temperature, increase of initial permeability is attributed to the stress relief, increase of packing density of atoms by annealing out micro-voids and changing the degree of chemical disorder. Temperature dependence of permeability curve passes through a maximum just before a sharp fall to near zero with the manifestation of Hopkinson effect characterizing the ferro-paramagnetic transition of the amorphous phase. When the sample is annealed above crystallization temperature, the sharpness of the fall to lower values of permeability is progressively smeared out with the appearance of a fall in the high temperature region.

The crucial role of exchange interaction is clearly evident when the measuring temperature exceeds the Curie temperature of the amorphous matrix ( $T > T_c^{\text{max}}$ ) in the temperature dependence of permeability of these biphasic alloys. For  $T > T_c^{\text{amor}}$ , the intergranular amorphous matrix become paramagnetic within which  $\alpha$ -Fe(Si) ferromagnetic nanograin are embedded. The exchange coupling between the nanograin



largely ceases to exist. Thus for the measuring temperature  $T > T_c^{amorph}$ , the initial permeability drops down by almost two orders of magnitude and the coercivity increase correspondingly. When the sample annealed above the second crystallization temperature obtained from thermal analysis, temperature dependence of permeability is governed by the presence of  $Fe_2B$  phase<sup>(1.3-1.5)</sup>. Some times, presence of brode phase cannot be dected by X-ray diffraction. Since the anisotropy constant of  $K_1$  of  $Fe_2B$  ( $430 \text{ kJ/m}^3$ ) is five order of magnitude higher than the average anisotropy  $\langle K \rangle$  of  $\alpha\text{-Fe(Si)}$  nanograins ( $4\text{J/m}^3$ ), minor evolution of  $Fe_2B$  phase can cause significant damage to exchange interaction. Temperature dependence of  $\mu'$  reveals are the presence of  $Fe_2B$ , which is not possible to detect. by X-ray diffraction. Since  $K_1$  of  $Fe_2B$  phases from negative to positive value at 523K dramatic rise of  $\mu'$  from a very low value by an order of magnitude at room temperature is expected at 523K for the samples annealed about 873K and above.

Isotropic nanocrystalline magnetic materials with uniaxial anisotropy have been found to have a remanence to saturation magnetization ratio above the value of  $\frac{M_r}{M_s} = 0.5$  predicted by Stoner-Wohlfarth model. This romance enhancement is attributed to intergrain exchange interactions<sup>(1.6-1.8)</sup> and it has been observed both in single phase<sup>(1.6,1.9)</sup> and nanocomposite materials consistong of a fine mixture of soft and hard phases<sup>(1.10-1.12)</sup>. Exchange coupling between the phases allows one to optimize the magnetic properties of nanocomposite magnets by combing the high magnetization due to the presence of the soft phase with the high anisotropy of the hard phase. Nanocomposite materials show the characteristic 'exchange spring' behavior, which results from the reversible rotation of the soft magnetic component for field not large enough to reverse the hard magnetic phase<sup>(1.12)</sup>.

In Fe-based hard nanocoposite magnetic materials, magnetic properties are characterized by exchange-biased soft and hard nanocomposite phases<sup>(1.12)</sup>. Presence of soft nanostructured phase would lead to high value of remanence, which is expected to be

greater than 0.5 while presence of hard nanostructured phase would lead to high value of coercivity, which is expected to be greater than 3kOe in the optimized annealing condition. Remanent ratio is greater than 0.5 is highly describable for development of permanent magnet. Magnetic properties of exchange spring magnets are governed by the soft and hard magnetic phases that develop under appropriate annealing condition. High reduced remanence characteristic to these materials arises from exchange coupling of magnetic moments across the interface between two phases. Besides high reduced remanence such systems possess high energy product  $(BH)_{\max}$  and a reversible demagnetization curve, which has been called as exchange-spring behavior. The theoretical limit for the maximum energy product of a given magnetic material [The magnetic induction is written as  $B = \mu_0(H + M) = \mu_0 H + J$ , with  $\mu_0 = 4\pi \times 10^{-7} \text{ Vs/Am}$ , Thus giving B and the polarization J in T, and the magnetic field H and the magnetization M in A/m]

$$(BH)_{\max} \leq \frac{J_s^2}{4\mu_0} \quad (1.1)$$

depends explicitly only on its saturation polarization  $J_s = \mu_0 M_s$ , but is besides subject to the following conditions: saturation remanence  $B_r = J_s$  (solid ferromagnetic material, i.e. packing fraction  $\rho = 1$  and alignment of easy axes parallel to the field axis) and critical fields for irreversible magnetization reversible (nucleation fields)

$$H_n \geq \frac{J_s}{2\mu_0} = \frac{M_s}{2} \quad (1.2)$$

On account of these conditions, the limit equation(1.1) may in principle be reached only with materials that have a sufficiently high nonplanar (preferentially uniaxial) magneto crystalline anisotropy  $K \gg \frac{J_s^2}{4\mu_0}$ , where K is the magneto crystalline anisotropy constant. More generally speaking, the magnitude of the ratio

$$k = \frac{J_s^2}{4\mu_0} = \frac{4K}{\mu_0 M_s^2} \quad (1.3)$$



Equation(1.3) are characterizes the basic magnetic behavior of the material . If  $k \gg 1$ , the behavior is dominated by magneto crystalline anisotropy; such materials are called hard magnetic (k-material). If  $k \ll 1$ , the behavior is governed by magnetostatic energy and such materials are called soft magnetic (m-material).  $J_s$  is for most k-materials considerably lower than for many common m-materials, whereas the coercivity  $H_{CM}$  of k-materials may exceed by far the value  $\frac{M_s}{2}$  necessary to reach the limit equation(1.1). Moreover, the best of the k-materials contain about 25 wt% or more of a rare earth metal, which adds to their price and raises serious problems with respect to chemical stability, while most m-materials are much less reactive and rather inexpensive.

Therefore it is tempting to consider composite materials consisting of two suitably dispersed and mutually exchange-coupled phases, one of which is of the k-type thus providing a high enough nucleation field for irreversible magnetization reversal, and other is an m-type material with  $M_s$  as high as possible, in order to attain a high average saturation. In addition the m-material may envelop the k-phase regions in order to prevent their corrosion. This causes the magnetic moments of both the phases to remain in the same direction. It has been demonstrated earlier by Kneller and Hawig<sup>(1,12)</sup> that the enhancement of remanence and coercivity by this mechanism is mainly governed by the crystallite sizes of both the phases in particular the soft phase, which can be controlled that treatment. Compared to single phase  $Nd_2Fe_{14}B/Fe_3B$  based alloys are economic and corrosion resistant. Various dopents and substituents have been used to enhance the value of coercivity. A partial substitution of Nd by heavy rare earth elements like Tb increases the anisotropy field,  $H_A$  which enhances the coercive field, but decreases strongly the remanence due to its antiferromagnetic coupling between rare earth and the transition metal<sup>(1,13)</sup>.

The demagnetization branch of the hysteresis loop is convex when the soft and hard phases of the samples are exchange coupled in the optimum condition of annealing. When the sample is over annealed, over-aging of the nanograins would lead to the demagnetization curve being concave. If there were no exchange coupling between

phases one would get constricted hysteresis loop. The recoil permeability of an exchange spring magnet is expected to be about 5 times as large as that of a conventional magnet with equal coercive field and saturation magnetization, which signifies reversibility of magnetic moment in the soft phase below certain critical field<sup>(1,14)</sup>. Reversibility of magnetization can be studied from dc field demagnetization technique known as DCD technique and recoil hysteresis loops. Temperature dependence of hysteresis loop parameters lead to the variation in the shape of hysteresis loop in low temperature region i.e. in the range of 5 – 150K due to spin reorientation of magnetic moment of  $\text{Nd}_2\text{Fe}_{14}\text{B}$  from  $30^\circ$  (from C-axis) to c-axis. By using the demagnetization remanence (DCD) technique it has been demonstrated that when a negative field ( lower than the critical field for magnetization reversal of the hard phase) is applied to a previously saturated sample, a near-reversible rotation of the soft phase magnetization is obtained when the field is decreased back to zero, giving rise to the high permeability.

In the present study the magnetization process in the nanostructured exchange-biased system. This is nanocomposite magnetic materials of the composition  $\text{Nd}_3\text{Tb}_1\text{Fe}_{76}\text{Cu}_{0.5}\text{Nb}_1\text{B}_{18.5}$ . The main objectives of the present work are to synthesize Fe-based alloys of the above mentioned compositions in the amorphous states by using rapid solidification technique and study their magnetic properties with the evolution of different phases by varying annealing conditions. Finally it is shown how this material of this kind may be realized technologically and that its magnetic behavior corresponds entirely to the predictions of the theory.

In this thesis, chapter-1 contains-introduction of my work, chapter-2 contains the description of soft and hard exchange-biased system, chapter-3 contains introductory theoretical aspects and brief literature review on these above mention system, chapter-4 contains the description of experimental set-ups used in this work and chapter-5 contains the experimental results and discussions on this system. Finally chapter contains the concluding remarks.



**CHAPTER – 2**  
**SOFT AND HARD EXCHANGE-BIASED SYSTEM**

---

## 2.0 SOFT AND HARD EXCHANGE-BIASED SYSTEM

### 2.1 Introduction

As we know from the history more than two thousand years ago, Chinese navigators were the first to use magnetic materials as compass. After a long period the dynamic uses of the magnetic materials were even unnoticed and the discovery of Faraday (British scientist) law made a history for the basis of the second industrial revolution because of the general availability of electric power. Since then it also started the exploration of better magnetic properties of the man made permanent magnets.

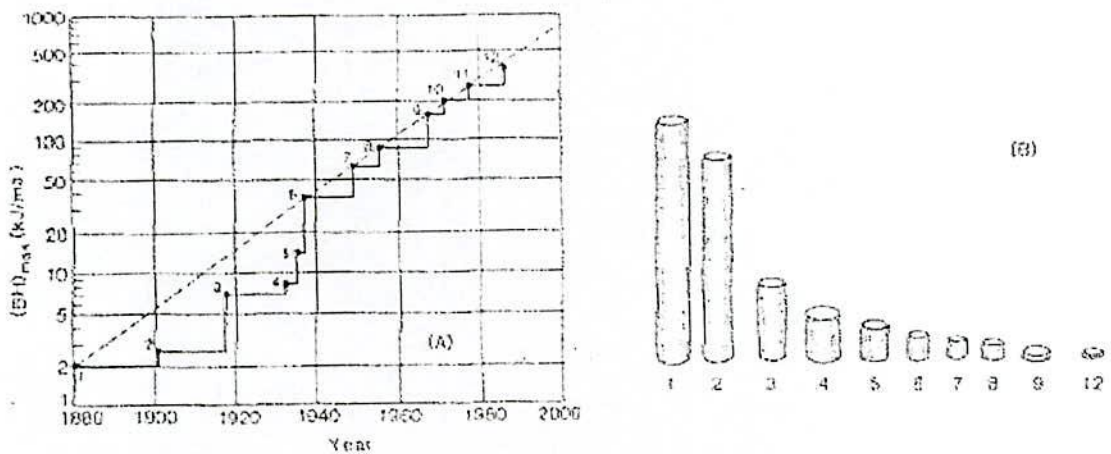


Fig 2.1 The history of  $(BH)_{max}$  since 1880. (A): (1) carbon steel, (2) tungsten steel, (3) cobalt steel, (4) MK steel, (5) "Ticonal II", (6) "Ticonal G", (7) "Ticonal GG", (8) "Ticonal XX", (9)  $\text{SmCo}_5$ , (10)  $(\text{SmPr})\text{Co}_5$ , (11)  $\text{SmCo}_7$ , (12)  $\text{NdFeB}$ . (B): Keeping  $B \times \phi$  and  $H \times L$  constant ( $B$  = magnetic induction,  $H$  = magnetic field strength,  $\phi$  = cross section of the magnet and  $L$  = length of the magnet), the volume of the magnets decreases with increasing  $(BH)_{max}$ . The numbers in (B) correspond to the numbers in (A).

A permanent magnet should possess two important properties. First, the magnetization should still be present when the external magnetizing field is removed.

Second, it should counteract a demagnetizing force due to a reversed magnetic field. A more comprehensive characterization is achieved by means of the maximum energy product  $(BH)_{\max}$ . On the other hand, it has been observed that for the same volume of the magnetic gap and the same strength of the magnetic field in the gap, a larger  $(BH)_{\max}$  of the permanent magnet results in a smaller volume of the permanent magnet. Therefore, the maximum energy product is a basic parameter for measuring the performance of the permanent magnets.

Since the eighties of the nineteenth century, the maximum energy product of permanent magnets has been improved by more than a factor of hundred which is summarized in Fig. 2.1. It is interesting to note how closely the curve approximates an exponential development. So far the permanent magnets with the best performance, concerning the energy product, are the rare-earth permanent magnets. Among all of the rare-earth permanent magnets, the  $(BH)_{\max}$  of Nd-Fe-B exceeds  $400\text{kJ/m}^3$  (50MGOe).

In the rare-earth permanent magnets, the magnetic moments on the transition-metal atoms, such as Fe or Co, are exchange coupled with the magnetic moments on the rare-earth atoms, which located at crystallographic sites with strong uniaxial anisotropy. The 3d atoms provide a high magnetic-ordering temperature by means of the 3d-3d exchange interaction. The exchange interaction between 3d and 4f moments results in the compounds with strong uniaxial anisotropy, and provides the intrinsic magnetic properties for high coercivity magnets.

Since the success of rare-earth permanent magnets, one as hoped to find a new kind of compound which would have better intrinsic properties and would be cheaper than  $\text{Nd}_2\text{Fe}_{14}\text{B}$ . Since 1983, when  $\text{Nd}_2\text{Fe}_{14}\text{B}$  was discovered, no real improvement has been achieved, despite the fact that some new compounds have been found, such as  $\text{Sm}_2\text{Fe}_{17}\text{N}_x$  that has a higher Curie temperature and stronger uniaxial anisotropy than  $\text{Nd}_2\text{Fe}_{14}\text{B}$ . However, its theoretical  $(BH)_{\max}$  value is smaller than  $\text{Nd}_2\text{Fe}_{14}\text{B}$  and the element Sm is even more rare than Nd. Now the question has arisen whether the  $(BH)_{\max}$  of permanent magnets can be increased appreciably in materials. Therefore, after a lot of





experimental performance being done it has been shown that, a much higher  $(BH)_{\max}$  may be obtained if a material with a low coercivity and high remanence can be properly combined in a composite material with a material with high coercivity and low remanence. In such a material, both materials can make up each other's deficiencies.

## 2.2 The Exchange- Spring Magnet- One Dimensional Model

Kneller and Hawig<sup>(2.1)</sup> used a one- dimensional model shown in Fig.-2.1 to represent the basic principles of the exchange coupling between the hard magnetic phase (k phase ) and the soft- magnetic phase (m phase) . The magneto crystalline anisotropy is assumed to be uniaxial in both phases, with the easy axis being parallel to the z- axis and perpendicular to the x -axis. Furthermore the composite material is assumed to be consists of a sequence of alternating k- and m- phase regions along the x- axis with widths of  $2b_k$  and  $2b_m$ , respectively, being crystallography coherent and exchange coupled through the phase boundaries<sup>(2.2)</sup>. The anisotropy energy density depends on the angle  $\varphi$  between  $\vec{M}$  and the easy axis as

$$E_k = K \sin^2 \varphi , \quad (2.1)$$

where  $K > 0$ . As per the definition mentioned earlier it may be mentioned that the ratio of the hard phase  $k_k = \frac{4K_k}{\mu_0 M_{sk}^2} \gg 1$  that for the soft phase,  $k_m = \frac{4K_m}{\mu_0 M_{sm}^2} \ll 1$ . The ratio  $\frac{k_k}{k_m}$  is of the order  $10^2$  to  $10^3$ , according to Table-2.1. This is due mainly to the magnitude of the ratio  $\frac{M_{sm}^2}{M_{sk}^2}$  not exceeding 10 in practical cases.

The exchange energy density may be written in the form

$$E_A = A \left( \frac{d\psi}{dx} \right)^2 , \quad (2.2)$$



Table 2.1: Room temperature values of magnetic properties of some magnetically hard (K-type) and some magnetically soft (M-type) materials (2.1)

Category	Material	Crystal symmetry	$T_C$ , °C / K	$M_s$ , °C / K	K ( $10^6 J/m^3$ )	$\bar{K} = \frac{4K}{\mu_0 M_s^2}$	$H_A$ $10^6 A/m$	$\mu_0 H_A$ , T	$J_s$ , T	$\frac{J_s^2}{4\mu_0}$ , $10^3 J/m^3$
K-type Hard ( $K \gg 1$ ) $H_A = \frac{2K}{\mu_0 M_s}$	BaO	hex	450/723	0.38	0.32	7.2	1.35	1.7	0.47	0.45
	$6Fe_2O_3$	tetr	360/633	0.58	1.16	9.2	2.94	3.7	0.72	1.30
	MnBi	tetr	312/585	1.25	9.40	19.0	12.00	15.1	1.57	4.90
	$Nd_2Fe_{14}B$ $Co_3Sm$	hex	730/103	0.84	11.90	54.0	23.00	28.6	1.05	2.20
$K \approx 1$ $\frac{M_s}{2}$ $\frac{2K}{\mu_0 M_s}$ M-type soft $K \ll 1$ $H_A = \frac{M_s}{2}$	Co	hex	1120/1393	1.40	0.53	0.48	0.70/0.60	0.88/0.75	1.76	6.2
	$\alpha Fe$	cub	760/1043	1.70	0.047	0.05	0.85	1.06	2.13	9.0
	$Fe_{23}B_6$	cub	425/698	1.35	0.01	0.03	0.67	0.86	1.70	5.7
	$Fe_3B$	tetr	570/783	1.28	$\approx 0.2$	0.39	0.64	0.80	1.60	5.1

where  $A$  is a constant of the order  $10^{-11}$  J/m at room temperature, but depends on the Curie temperature  $T_c$  and temperature  $T$  as  $A \propto T_c \left[ \frac{M_s(T)}{M(0)} \right]^2$ , and  $\psi$  is for the present model the angle in the  $yz$ -plane between  $M_s$  and the  $z$ -axis. With these quantities, the energy per unit area of a  $180^\circ$  Bloch wall in a homogeneous material may approximately as

$$\gamma(\delta) \approx \delta K + \delta A \left( \frac{\pi}{\delta^2} \right), \quad (2.3)$$

where  $\delta$  is the wall thickness,  $K$  is the magnetocrystalline anisotropy constant and  $A$  the exchange constant. The two terms in equ<sup>n</sup>(2.3) represent the anisotropy energy and the exchange energy respectively.

In equilibrium,  $\gamma(\delta)$  has a minimum  $\left( \frac{d\gamma}{d\delta} = 0 \right)$ , from where the equilibrium quantities  $\delta_0, \gamma_0$  are obtained

$$\delta_0 \approx \pi \left( \frac{A}{K} \right)^{1/2} \quad (2.4)$$

$$\gamma_0 \approx 2\pi \left( AK^{1/2} \right) \quad (2.5)$$

Critical dimensions for a high energy magnetization reversal in the one dimensional system in Fig.-2.2 are obtained from a consideration of the reversal process. Let us assume that the hard phase has a reasonable thickness,  $b_{k_0} \approx \delta_0 = \pi \left( \frac{A}{K} \right)^{1/2}$  corresponding to about its critical thickness. Starting from the saturation remanence along the easy direction  $+z$ -axis shown in Fig.-2.2(a), when the magnetization will invariably begin to change reversibly in the soft phase. It should be noted at this point that since  $k_m \ll k_k$  therefore;  $b_m \approx \delta_{0m} = \pi \left( \frac{A_m}{K_m} \right)^{1/2}$ .

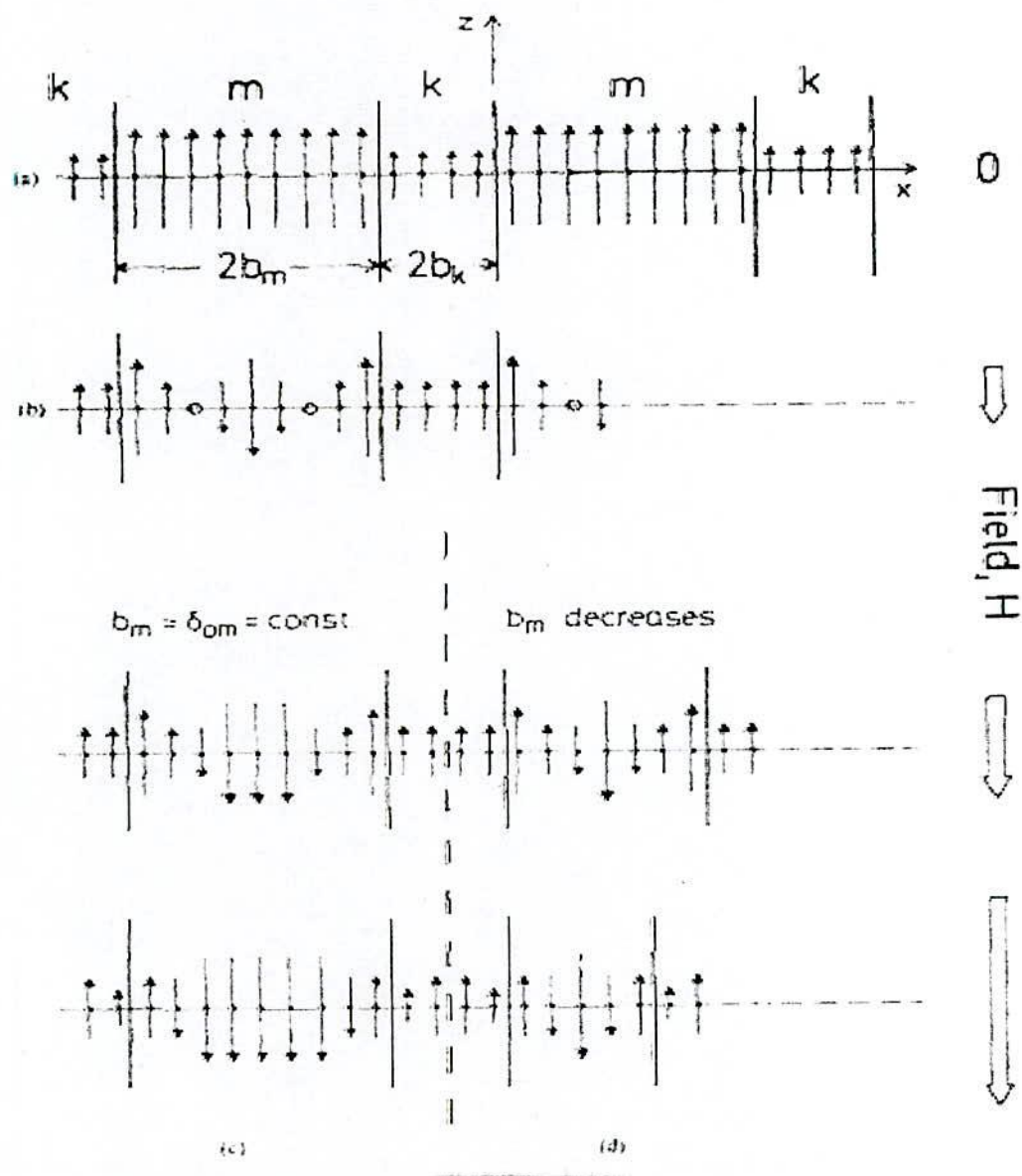


Fig.2.2. Schematic one-dimensional model of the microstructure and the micromagnetic structure of the exchange-coupled composite material as a basis for the calculation of the critical dimensions of the phase regions:

- (a) Saturation remanence.
- (b)-(c) Demagnetization in an increasing reverse field  $H$  at a constant overcritical width of the m-phase,  $b_m \gg b_{cm}$ ,
- (d) Demagnetization at decreasing width  $b_m \rightarrow b_{cm}$ .



In this condition, two equilibrium  $180^\circ$  walls will form reversibly in m-phase in Fig.-2.2(b). When  $\vec{H}$  is further increased in Fig.-2.2(c), these walls will be reversibly compressed towards the k-phase boundary, and the energy density in these walls will increase above its equilibrium value. The magnetization in the k-phase  $\vec{M}_{sk}$  remains essentially unchanged, as  $k_k \gg k_m$ . This process will continue until the energy density in the soft phase,  $E_{\gamma m}$  approaches the equilibrium energy density of the hard phase  $E_{\gamma ok}$ . In this case, the wall will invade into the k-phase regions. The corresponding critical field  $H_{no}$  is lower than the anisotropy field of the k-phase  $H_{no} < H_{Ak} = \frac{2k_k}{M_{sk}}$ , yet it will have about the same order of magnitude.

The coercive field  $H_{CM}$  is defined by  $M(H_{CM}) = 0$  and is much smaller,  $H_{CM} \ll H_{no}$  as  $M_{sm} > M_{sk}$  and because it has been assumed that  $b_m \gg b_k$ , and thus the demagnetization curve  $M_r(H=0)$  and  $M(H_{CM}) = 0$  is completely reversible. If  $b_m$  is now reduced to values  $b_m < \delta$ ,  $H_{no}$  remains unchanged, but  $H_{CM}$  increases because, for  $H < H_{no}$ , the thickness of the  $180^\circ$  walls in the m-phase is essentially confined  $\delta_m \approx b_m < \delta_{om}$ .

Hence the critical width of the m-phase  $b_{cm}$ , giving the maximum coercivity is determined in the following way. For small  $\delta_m$  ( $\delta_m \ll \delta_{om}$ ) from equ<sup>n</sup>(2.3),

$$\gamma_m(\delta_m) \approx \delta_m A_m \left( \frac{\pi}{\delta_m} \right)^2, \text{ from where the energy density}$$

$$E_{\gamma m} = \frac{\gamma_m}{\delta_m} \approx A_m \left( \frac{\pi}{\delta_m} \right)^2. \quad (2.6)$$

Increasing the result in  $\delta_m = b_{cm}$  yields the critical dimension of the m-phase

$$b_{cm} \approx \pi \left( \frac{A_m}{2k_k} \right)^{1/2}, \quad (2.7)$$



with representative values  $A_m = 10^{11} \text{ J/m}$ ,  $k_k = 2 \times 10^6 \text{ J/m}^3$ , one gets for  $b_{cm} \approx 5 \text{ nm}$ . For the k-phase a critical thickness cannot be derived theoretically. For practical purpose it seems reasonable to take  $b_{ck}$  about equal to the equilibrium wall thickness in the k-phase

$b_{ck} = \delta_{ok} = \pi \left( \frac{A_k}{k_k} \right)^{1/2}$ , as has been assumed initially. Since mostly  $A_k < A_m$  on account of the generally low Curie temperature of the K-materials, this gives for  $b_{ck}$  about the same magnitude as  $b_{cm}$ .

$$b_{ck} = b_{cm} \quad (2.8)$$

Because the model of Kneller and Hawig<sup>(2.1)</sup> is very simple, one may not expect that the calculated results will exactly represent reality. Nevertheless, the model qualitatively describes the basic relationships between the microstructure and the magnetic properties of a two phase exchange – coupled magnetic material. By means of equ<sup>n</sup>(2.7) one can understand that the larger the exchange constant  $A_m$  of the m phase is, the larger the exchange coupling length  $b_{cm}$  of the m- phase will be. On the other hand, the smaller the magnetocrystalline - anisotropy constant  $K_k$  of the k- phase, the larger the exchange – coupling length  $b_{cm}$  of the m- phase. The microstructure should consist of two suitably dispersed ferromagnetic and mutually exchange- coupled phases, one of which is hard magnetic in order to provide a high coercive field, while other may be soft magnetic, providing a high saturation magnetization. The grain size of the soft magnetic phase should be twice the domain wall width of the hard magnetic phase.

## 2.2 Effect of Exchange Coupling on the Macro-Magnetic Properties

Essential conditions for the microstructure of such materials are affine and regular dispersion of phases on a scale of the order 10nm ( $b_{ck} = b_{cm} = 5 \text{ nm}$ ) and exchange coupling between the k- and m-phase regions, which implies the crystallographically coherent formation of two phases with generally different structures, such conditions are known to arise during the continuous decomposition of a metastable supersaturated phase

that has crystallized from a glassy state<sup>(2.3)</sup>. This means that materials with the desired properties may be produced by liquid quenching of a suitable alloy to the glassy state and subsequent heating of the glass. In fact the usefulness of the glassy state as a precursor for producing permanent magnet materials has been widely recognized for over ten years<sup>(2.4 - 2.10)</sup>, mainly because very finely grained microstructures may be obtained by this method.

The first indication of typical features of such a mechanism was gathered from a recent publication of Coehoorn *et. al.*<sup>(2.10)</sup>, who reported that liquid quenching and subsequent heating of alloys in the vicinity of  $\text{Nd}_4\text{Fe}_{77}\text{B}_{19}$  leads to remarkable permanent magnet properties [up to  $H_{CM} = 280\text{kA/m}$ ,  $(BM)_{\max} = 95\text{kJ/m}^3$ ] in a state in which the material was found to consist of 85% definitely soft magnetic phases [73%  $\text{Fe}_3\text{B}$  and 12%  $\alpha\text{-Fe}$ ] and only 15% hard phase [ $\text{Nd}_2\text{Fe}_{14}\text{B}$ ]. Moreover, it was particularly noted in that publication that the material exhibits an unusually high isotropic remanence ratio  $m_r > 0.5$ . The further development begins with the decomposition into  $\text{Fe}_3\text{B}$  and  $\alpha\text{-Fe}$ , thereby increasing the until these transform into the hard phase  $\text{Nd}_2\text{Fe}_{14}\text{B}$ , i.e. the hard phase form here not as a primary precipitate in the  $\text{Fe}_{23}\text{B}_6$  phase, but from the Nd enriched remainder of the decomposition of  $\text{Fe}_{23}\text{B}_6$  into  $\text{Fe}_3\text{B}$  and  $\alpha\text{-Fe}$ .

A magnetically soft matrix containing very fine and rather homogeneously distributed inclusions of a hard phase. It is remarkable that the crystallographic coherency and consequently the exchange coupling between the phases is retained, as is evident from the magnetic properties. The exchange coupling between neighboring grains may result in some special types of magnetic behavior:

### 2.2.1 Volume Fractions of Phases

The optimum geometry of the microstructure minimizes the volume fraction of the k-phase

$$v_k = \frac{V_k}{V} \quad (2.9)$$

where  $V_k$  is the volume of the k-phase;  $V$  is the total volume of material under the conditions of about equal lateral dimensions of the two phases,  $b_{cm} = b_{ck}$  and the chemical protection of the k-phase by the m-phase. A mathematical solution of this problem would be of no practical value, because in technologically realizing such a material one must put up with the microstructure that nature produces with a suitable pair of phases.

However, that the type of microstructure to look for is a homogeneous precipitation of a k-phase in an m-phase, and not vice versa. With the reasonable assumptions that precipitates with diameters of the order of some nm are spherical (minimum surface to volume ratio) and are spatially distributed approximately according to an fcc lattice (equal diffusion paths). One obtains

$$v_k = \frac{\pi}{24\sqrt{2}} \approx 0.09. \quad (2.10)$$

Virtually the same result is obtained with bcc lattice:

$$v_k = \frac{\pi\sqrt{3}}{64} \approx 0.09. \quad (2.11)$$

Once  $v_k$  is known, the average saturation magnetization of the materials given by

$$M_s = v_k M_{sk} + (1 - v_k) M_{sm} \quad (2.12)$$

Under the initial assumption  $M_{sk} < M_{sm}$  and with  $v_k = 0.09$ , equ<sup>n</sup>(2.12) yields  $M_s \approx M_{sm}$ , whereas for platelets of alternating k- and m-phases as in the model Fig.-2.2,  $v_k \approx 0.5$  and  $M_s = \frac{M_{sk} + M_{sm}}{2}$ .

## 2.2.2 Effect of Remanence Enhancement

Within the frame work of the Stoner-Wohlfarth theory, the saturation remanence of an ensemble of non interacting and single-domain grains, with uniaxial



magneto-crystalline-anisotropy and with isotropic distribution of the easy axes, is given by  $J_r = 0.5J_s$  ( $J_s$  is the spontaneous polarization). In this case, the easy directions lying in the upper half-sphere are equally occupied. If, however, the neighbouring grains are coupled by exchange interaction, particularly in a two phase composite material, if  $b_m = b_{cm}$ , all magnetic moments of the soft-magnetic phase are coupled by exchange interactions originating from neighboring hard magnetic phase grains. In this situation, the magnetic moments of neighboring grains tend to align parallel to each other along the original saturation magnetization direction. Therefore, the remanence  $J_r$  will be larger than  $0.5J_s$ .

### 2.2.3 Effect of Coercivity Reduction

The demagnetizing field will reduce the magnetization by reversing the magnetic moments. The demagnetizing field at which the magnetization is reduced to zero is defined as the coercive field or the coercivity. One can assume that there is only a difference of microstructure between the two systems with same magnetic matrix phase, i.e., in one system, all magnetic grains are isolated by a paramagnetic layer, and in another system, the neighboring magnetic grains are coupled by exchange interaction through the grain boundaries. In the latter system, when the demagnetizing field reverses the moments in some grains, they tend to reverse the moments in the neighboring grains by exchange coupling. Therefore, there is an additional demagnetizing field due to the neighboring grains. The effective demagnetizing field in the exchange-coupled system is larger than in the "isolated system". Exchange coupling leads to a decrease of the coercivity.

In a two phase exchange-coupled system, the effective anisotropy field of the soft magnetic phase increases and the effective anisotropy field of the hard magnetic phase decreases due to the exchange-coupling between both kind of grains. Therefore, the coercivity of a two phase nano composite magnet should be in between the coercivities of the hard magnetic phase and the soft magnetic phase. The higher  $J_s$  of the soft magnetic phase, the lower the coercivity of two phase exchange coupled system, despite the enhancement of the remanence. Therefore remanence enhancement



originating from the exchange coupling can only be reached at the expense of the coercivity.

### 2.2.4 Effect of Exchange Coupling on the Demagnetizing Curve

If all magnetic moments of the soft magnetic phase in a two phase composite material are in the exchange-coupled region, i.e, if the mean grain size of the soft phase  $2b_m$  is equal to  $2b_{cm}$ , the demagnetizing curve after previous saturation will be convex in the second quadrant, like for single - phase material. If  $2b_m > 2b_{cm}$ , some of the magnetic moments in the central part of the soft magnetic phase will become decoupled from neighboring grains of the hard magnetic phase. When the demagnetizing field reaches the reversal field of the soft- phase, these decoupled moments will reverse which will lead to a large reduction of the magnetization. Thus the demagnetizing curve will have a concave shape in the second quadrant. In practice, there is a demagnetizing field originating from the magnetic charges at the surface or/and inside the magnetized sample. When the external magnetizing field is near zero, the demagnetizing field easily reverses the decoupled moments to give rise to a step in the demagnetizing curve around zero field.

### 2.2.5 Spring - Magnet Behavior

In the demagnetizing process which starts from the saturated remanent state, the reversal of magnetic moments is reversible when the demagnetizing field ( $H_d$ ) is smaller than the critical switching field ( $H_{no}$ ). However, when  $H_d > H_{no}$ , the reversal of the magnetic moments is irreversible. In a conventional hard magnet with single magnetic domain grains, the grains with orientation different from the demagnetizing field direction have different critical switching fields. For an assembly of rotated magnetic moments, some have experienced a reversible rotation some an irreversible rotation when the demagnetizing field is smaller than the largest critical field. When  $H_{no}$  is close to the coercivity ( $H_c$ ), the reversal is almost irreversible. In a two phase

exchange-coupled magnetic material the situation is different. For a sufficiently small demagnetizing field  $H_f$  most moments of the hard phase may not yet have reversed their direction, although much more moments of the soft phase have already done so. When the demagnetizing field is removed, the moments of the soft phase can return reversibly to their original direction owing to the exchange coupling to the neighboring hard grains. Thus the reversibility of two phase exchange coupled magnets is much larger than that of conventional hard magnets. This is partly due also to the fact that the saturation magnetization  $M_{sm}$  of the soft phase is larger than that of the hard phase  $M_s$ . The magnetic behavior sketched for the two phase magnet is, in a way, similar to that of a mechanical spring. Therefore, magnets with high reversibility are called spring magnets.

### 2.3 Hysteresis loop and Demagnetization Curve

According to the foregoing analysis, the demagnetization curve after previous saturation of such a material will be reversible in reverse fields  $H < H_{no}$  i.e., before the magnetization of the k-phase begins to switch, as is illustrated schematically in the Fig. 2.3(a) and Fig. 2.3(b). At  $H < H_{no}$  the material has unidirectional anisotropy<sup>(2.2)</sup>, on account of the exchange coupling between the two phases. This and the following statements with respect to reversibility hold independently whether the material is aligned or isotropic.

For a given pair of phases, the reversible range in  $M$ ,  $\Delta M_{rev}$  depends on the volume fraction of the hard phase  $v_k$  (or the soft phase  $v_m = 1 - v_k$ , respectively), on the ratio  $\frac{M_{sm}}{M_{sk}}$  and on the lateral dimension of the m-phase  $b_m$ . At fixed  $v_k$  and  $\frac{M_{sm}}{M_{sk}}$ ,  $\Delta M_{rev}$  is smallest for  $b_m \approx b_{cm}$ , (the optimum microstructure, Fig. 2.3(a)) and increases as  $b_m > b_{cm}$  [the overaged state, Fig. 2.3(b)], because  $H_{no}$  remains constant. At large  $v_m$ ,  $v_m = 0.8$ , for example,  $\Delta M_{rev}$  may well exceed the saturation remanence  $\Delta M_{rev} > M_r$  [Fig. 2.3(b)].

It is for this specific and quite typical magnetic behavior, in a sense resembling a mechanical spring that such magnets have been termed as exchange-spring magnets.

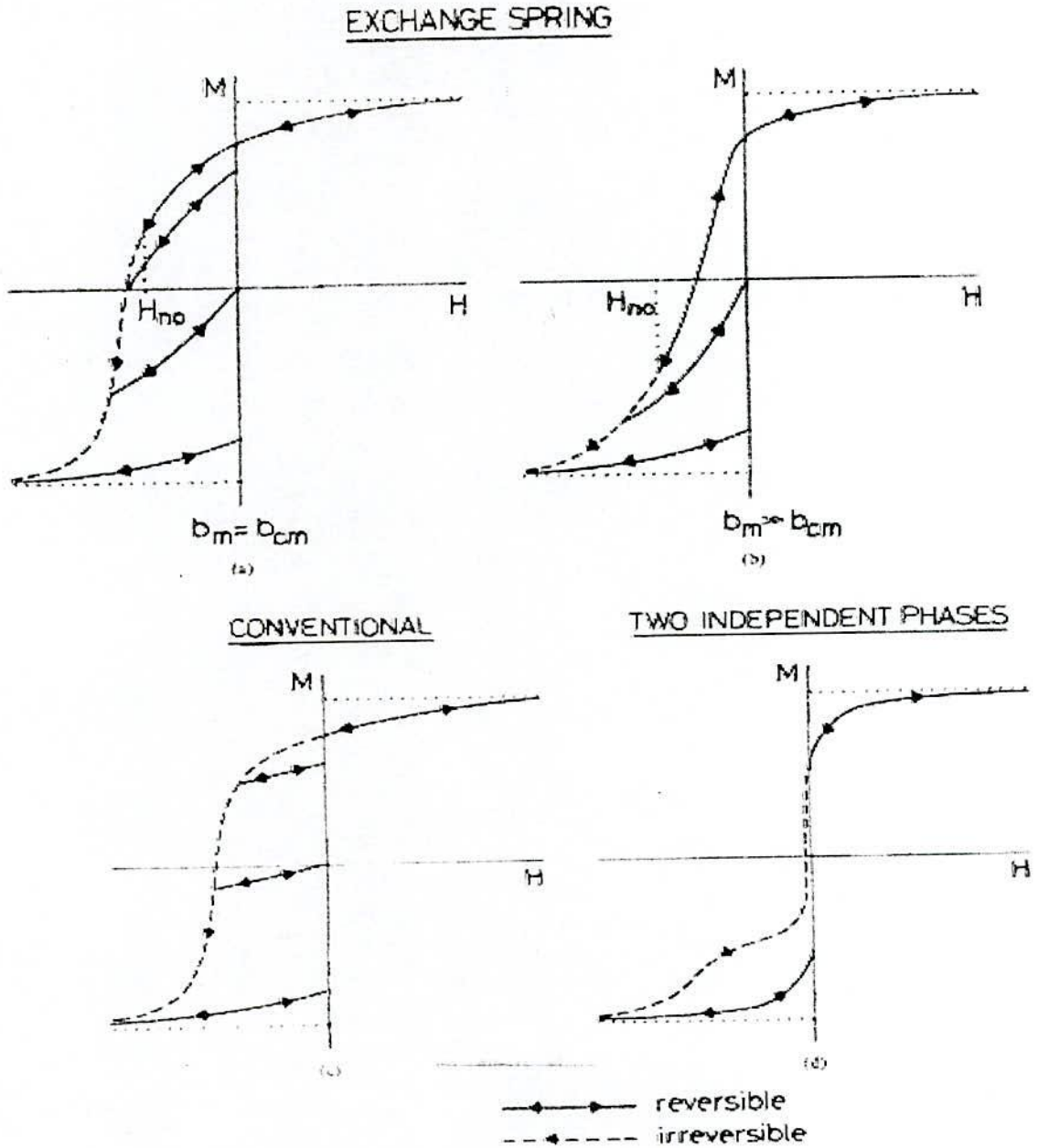


Fig.2.3 Typical demagnetization curves  $M(H)$  (schematic). (a) Exchange-spring magnet with optimum microstructure,  $b_m = b_{cm}$ . (b) As (a), but with averaged microstructure,  $b_m \gg b_{cm}$ . (c) Conventional single ferromagnetic phase magnet (d) Mixture of two independent ferromagnetic phases with largely different hardness (constricted loop).



Their striking reversibility in conjunction with a high remanence and a high coercivity distinguishes them uniquely from the conventional single ferromagnetic phase permanent magnets, where the demagnetization curves reflect essentially the distribution of the critical switching fields and are, therefore, mainly irreversible shown in Fig 2.3(c).

In order to further illustrate these features, some minor loops are drawn in the Fig. 2.3(a)-2.3(c), as they will be obtained upon reducing to zero and re-increasing the field at various points along the demagnetization curve. The recoil permeability  $\mu_r$  of an exchange spring magnet is expected to be about 5 times as large as that of a conventional magnet with equal coercive field and saturation magnetization..

As for the general shape of the demagnetization curve  $M(H)$ , it is immediately obvious from the exchange spring mechanism that an optimum microstructure ( $b_m = b_{cm}$ ) will yield a "normal" convex  $M(H)$  curve shown in Fig. 2.3(a) between  $M_r$  and  $M = 0$ , similar to a conventional permanent magnet shown in Fig. 2.3(c). Whereas an averaged microstructure ( $b_m \gg b_{cm}$ ) must lead to a quite characteristic shape of the demagnetization curve being concave throughout from short below the remanence on until saturation in the reverse direction. In any case, the exchange coupling between the phases produces a shape of the saturation loop like that of a uniform material showing no indication of the presence of two phases with extremely different magnetic hardness. If there was no exchange coupling, one would get a constricted loop as in Fig. 2.3(d).

### 2.3.1 Saturation Remanence Ratio

The value of  $m_r = \frac{M_r}{M_s}$  depends on the phases employed. A quantitative calculation of  $m_r$  for a given pair of phases is in general difficult, because it requires the micro magnetic treatment of complex many body magnetic systems. Therefore, this is describe here only the character of the problem and on that basis will derive approximate solutions for two simple cases in order to illustrate how the parameters of the systems determine the result.

It will be generally assumed that microstructure originates by precipitation of the k-phase in an m-matrix and thus corresponds in essence to the model and that a number

of k-precipitates in a single m-grain is large enough to apply statistics where appropriate. Moreover, it is assumed that the k-phase has a uniaxial crystal structure, e.g. tetragonal or hexagonal, with the  $c_k$ -axis being the easy magnetic axis, whereas the m-phase may have any symmetry, in particular cubic symmetry.

Since there must be magnetic exchange coupling between the k-phase and m-phase regions, the phases must be crystallographically coherent. This implies that the orientations of the  $c_k$ -axes (easy axis of the k-precipitates) in the m-matrix are not arbitrary, but must be parallel to specific crystallographic axes  $[h_0 k_0 l_0]$  of the m-crystal lattice. Since the precipitate will generally form at a temperature above the Curie temperatures of both phases, it may be presumed that the  $c_k$ -axes of the k-precipitates are distributed equally among these distinguished orientations  $[h_0 k_0 l_0]$ .

Now consider a single spherical (in order to exclude shape anisotropy) m-grain and disregard demagnetization effects <sup>(2.11)</sup>. Since  $k_k \gg k_m$ , the resulting saturation remanence of the k-precipitates in the grain  $\vec{M}_{rk}$  will then point in the direction  $[h_s k_s l_s]_0$ , which is symmetric with respect to the  $c_k$ -axes,  $[h_0 k_0 l_0]$  and forms the smallest angle  $\theta$  with the previously applied saturation field  $\vec{H}$ . Hence  $\vec{M}_{rk}$  is in general not parallel to  $\vec{H}$ . For simplicity, this assume for the following that all of these symmetry axes  $[h_s k_s l_s]$  with respect to  $[h_0 k_0 l_0]$  are crystallographically equivalent and form the same angle  $\alpha_k$  with all possible  $c_k$ -axes  $[h_0 k_0 l_0]$ . In such cases the relative magnitude of  $\vec{M}_{rk}$  becomes

$$\frac{M_{rk}}{M_{sk}} = m_{rk} = \cos \alpha_k \quad (2.13)$$

The magnetization of the soft m-matrix is exchange coupled with the magnetization of the k-precipitates along their mutual phase boundaries. Therefore, the resulting remanence of the m-matrix  $\vec{M}_{rm}$  will be parallel to  $\vec{M}_{rk}$ . The relative size of  $\vec{M}_{rm}$ ,  $\frac{M_{rm}}{M_{sm}} = m_{rm}$  will, however, be greater than  $m_{rk} = \cos \alpha_k$ , because the exchange coupling within the m-matrix will smooth out the local magnetization  $\vec{M}_{sm}(\vec{r})$  between



the nearly fixed because  $K_k \gg K_m$ ) magnetization directions in the surrounding k-precipitates in such a way that the total free energy is minimized. Thus the magnetization  $\vec{M}_{sm}(\vec{r})$  of the m-matrix in the remanent state will be, in general, inhomogeneous, and the resultant  $m_{rm}$  must be calculated micro magnetically from the condition of minimum total energy, which may be complicated.

Consequently there exist in each grain of the material j, depending on the crystal symmetry of the m-phase and the crystallographic coherency conditions for the k-precipitates, one or several equivalent axes  $[h_s k_s l_s]$  for the total resultant saturation remanence vector  $\vec{M}_{rj}$ , whose relative magnitude

$$m_{rj} = \frac{M_{rj}}{M_s} = \left( \frac{1}{M_s} \right) \left[ v_k m_{sk} M_{sk} + (1 - v_s) m_{rm} M_{sm} \right] \quad (2.14)$$

is the same for all grains.

For a polycrystalline sample of magnetically independent grains with their crystallographic axes oriented at random, the relative remanence  $m_r$  is then obtained by averaging over the angles  $\theta$  between the direction of the previous saturation field  $\vec{H}$  and the corresponding direction  $[h_s k_s l_s]_\theta$  of  $\vec{M}_{rj}$  in the grains:

$$m_r = \frac{M_r}{M_s} = m_{rj} \langle \cos \theta \rangle \quad (2.15)$$

Any numerical evaluation of equ<sup>n</sup> (2.15) requires the knowledge of the crystal symmetry of the m-phase, the crystallographic orientations  $[h_0 k_0 l_0]$  of the  $c_k$ -axes, and the volume fractions and saturations of the phases.

### 2.3.2 Nucleation Field and Coercive Field

The characteristic properties of an exchange-spring magnet, the nucleation field ( $H_{no}$ ) for irreversible magnetization reversal and likewise the coercive field ( $H_{cm}$ ) are the most complex and least reliably predictable quantities. Only rough estimates will be attempted. One would get for a completely aligned microstructure as in Fig.-2.2

$$H_{no} = \frac{2K_k}{\mu_0 M_{sm}}, \text{ and for an isotropic polycrystal about one half of this value}$$



$$H_{no} = \frac{K_k}{\mu_0 M_{sm}} \quad (2.16)$$

With representative quantities  $K_k = 2 \times 10^6 \text{ J/m}^3$ ,  $\mu_0 M_{sm} = 1.8T$ , this would give for  $H_{no}$  the order  $10^6 \text{ A/m}$ , which seems rather high and may be considered an upper limit to  $H_{no}$ .

For an optimum microstructure,  $b_m = b_{cm}$ , one would expect  $H_{cM} \approx H_{no}$ . For averaged microstructure, i. e. ,  $b_m > b_{cm}$ ,  $H_{cM}$  will depend on  $b_m$  as

$$H_{cM} = \frac{A_m \pi^2}{2 \mu_0 M_{sm}} \frac{1}{b_m^2} \quad (2.17)$$

For  $b_m = b_{cm} = \pi \left( \frac{A_m}{2K_k} \right)^{1/2}$ , equ<sup>n</sup>(2.17) transforms into equ<sup>n</sup>(2.18),  $H_{cM} = H_{no}$ . With representative values  $A_m \approx 10^{-11} \text{ J/m}$ ,  $\mu_0 M_{sm} = 1.8T$ , equ<sup>n</sup>(2.17) becomes

$$H_{cM} = \frac{3 \times 10^{-11}}{b_m^2} \text{ A/m}, \text{ giving with, e.g., } b_m = 10 \text{ nm}, H_{cM} = 3 \times 10^5 \text{ A/m}.$$

With regard to equ<sup>n</sup>(2.16),  $H_{no}$  and similarly  $H_{cM}$  must vary with temperature about as  $\frac{K_k}{M_{sm}}$ . In particular, if the Curie temperature of the k-phase is substantially lower than that of the soft m-phase  $T_{ck} < T_{cm}$  (see table-2.1),  $H_{cM}$  will decrease rapidly with rising temperature and at  $T_{ck}$  will reach the low value of the soft phase.

## 2.4 Magnetic Properties in the Optimum State

Both Fig.-2.4(a) and Fig.-2.4(b) are shows the typical characteristics of the exchange-spring mechanism, namely a high (isotropic) remanence ratio  $m_r > 0.5$  and a high degree of reversibility in fields below  $H_{cM}$ , the recoil permeability  $\mu_r = 1 + \frac{M}{H}$  being of the order of 5.

It is interesting to analyze the dc demagnetization curve  $M(H)$  between the saturation remanence  $M_r$  and the reverse saturation  $-M_s$ , in terms of the reversible and

the irreversible portions of the total magnetization change as a function of the reverse field.

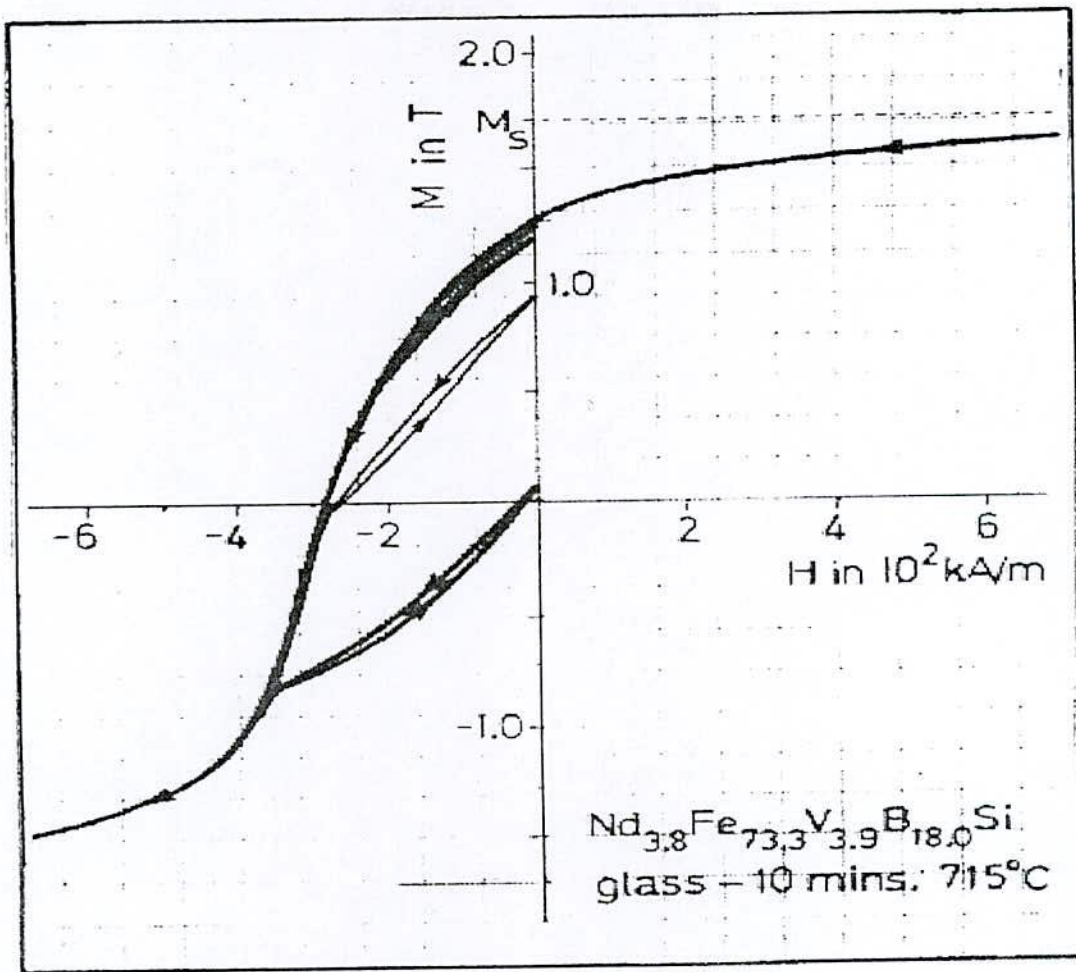


Fig.-2. 4 Demagnetization curve  $M(H)$  measured after previous saturation in the opposite direction in the field  $H = -1200 \text{ kA/m}$  on the alloy. (a) in the optimum magnetic state  $b_m = b_{cm}$  (b) in an averaged state.  $b_m > b_{cm}$

The irreversible portion is described by the dc field demagnetization remanence  $M_d(H)$ , being the remanence acquired after saturation in one direction and subsequent application of a dc field  $H$  in the opposite direction. Fig.-2.5(a) shows a plot of the reduced quantity  $D(H) = \frac{M_r - M_d(H)}{2M_r} = -\frac{\Delta M_{irrev}(H)}{2M_r}$  versus  $H$  as measured on the

alloy in the optimum state. The derivative  $\frac{dD(H)}{dH} = f(H_n)$  is the distribution function of critical fields  $H_n$  for irreversible magnetization reversals.

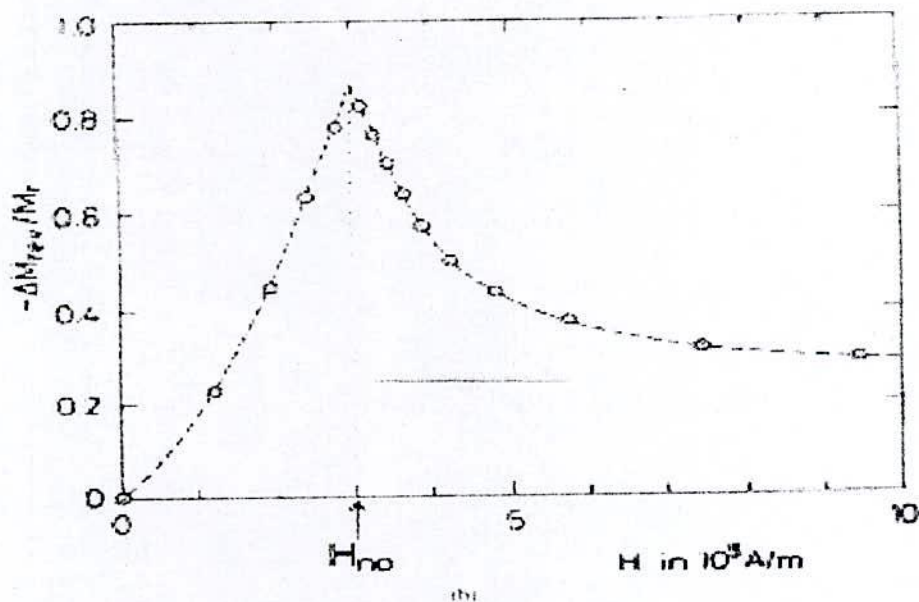
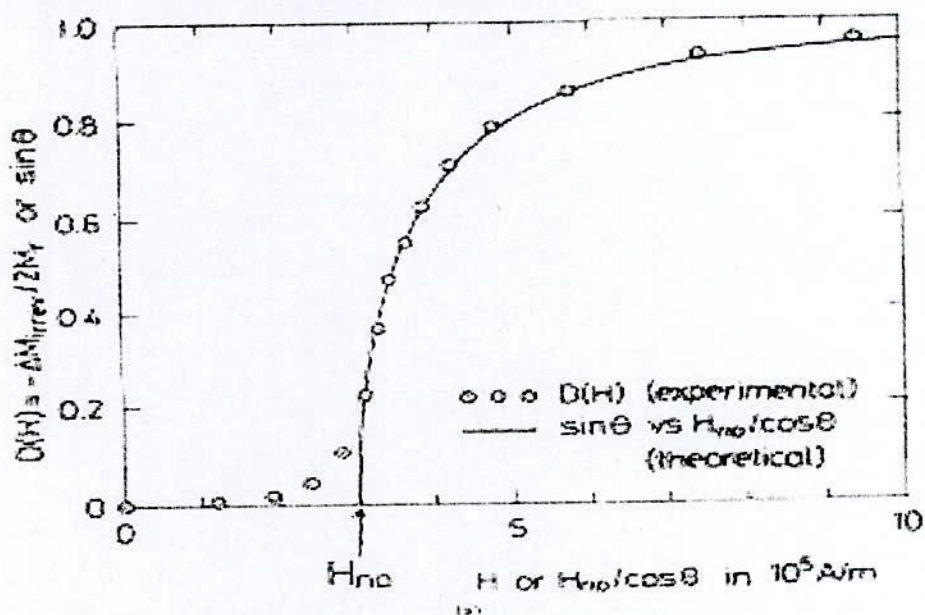


Fig.-2.5. Analysis of the total magnetization change  $-\Delta M(H) = -\Delta M_{irrev}(H) - \Delta M_{rev}(H)$ , along the demagnetization curve  $M(H)$ , after previous saturation in the opposite direction in the field  $H = 1200 \text{ kA/m}$  of the alloy in the optimum magnetic state. (a) Measurements of the irreversible portion



$D(H) = -\frac{\Delta M_{irrev}(H)}{2M_r}$ , versus  $H$ . The theoretical curve  $\sin \theta$  versus  $\frac{H_{no}}{\cos \theta}$

corresponds to the Kondorskij model of completely inhomogeneous rotation.  $H_{no} = 300$  kA/m from the best fit of the theoretical curve to the experimental data.  $\theta$  is the angle between the field axis and the z axis.

(b) Measurements of the reversible part  $-\frac{\Delta M_{rev}(H)}{M_r}$ , showing a sharp peak at  $H = H_{no} = 300$  kA/m. The reduction with  $M_r$ , serves the correlation with (a) and has no theoretical background.

The experimental curve  $D(H)$  may be interpreted according to the model in Fig. 2.2, i.e., by purely inhomogeneous magnetization rotation Kondorskij mechanism<sup>(2.12)</sup>, assuming equal probabilities of angles  $0 \leq \theta \leq 90^\circ$  in the xz-plane between the field  $H$  and the z axis. In that case,  $H_n(\theta) = \frac{H_n(0)}{\cos \theta} = \frac{H_{no}}{\cos \theta}$ . When the reverse field  $H$  increases from  $H = 0$ , no irreversible magnetization reversal occurs as long as  $H < H_{no}$ . When  $H$  increases further to some value  $H_1 = \frac{H_{no}}{\cos \theta_1}$ , for example, all regions with  $0 \leq \theta \leq \theta_1$ , have reversed, and the total irreversible change in magnetization is  $-\Delta M_{irrev} = 2M_r \int_0^{\theta_1} \cos \theta d\theta = 2M_r \sin \theta_1$ , from where  $D(H_1) = \frac{H_{no}}{\cos \theta_1}$ . The best fit of a

corresponding plot of  $\sin \theta$  versus  $\frac{H_{no}}{\cos \theta}$  to the experimental curve  $D(H)$  is obtained with the value  $H_{no} = 3.0 \times 10^5$  A/m. This curve is drawn in Fig.- 5(a). Hence most of the distribution  $f(H_n)$  is due to the distribution of angles  $\theta$ , whereas the mechanism of the irreversible magnetization reversal and the k- and m phases involved in it are the same throughout the sample.



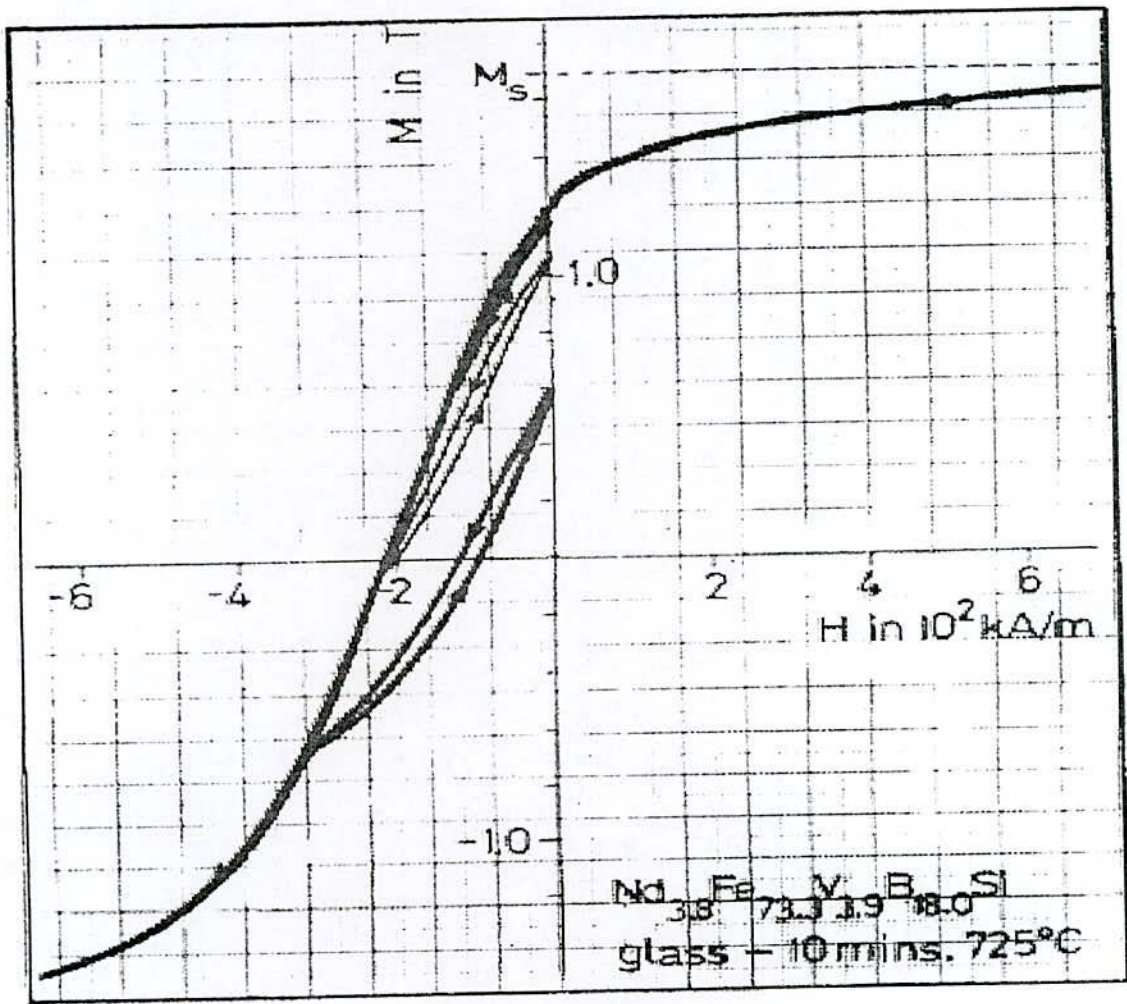


Fig. 6.1 (Continued.)

Measurements of the reversible portion  $-\frac{\Delta M_{rev}(H)}{M_r}$  versus  $H$  are given in Fig-

2.5(b) for the same sample as Fig.- 2.5(a). The reduction with  $M_r$  serves only the correlation with Fig. -2.5(a) and has no theoretical background. The initial (below the maximum) and final (high  $H$ ) parts of the curve in conjunction with shown in Fig. -2.5(a) reflects in an obvious manner properties of the hysteresis loop. The most remarkable feature of the curve is the sharp maximum at  $H = H_{no}$ , i.e., precisely where it is to be expected on account of the proposed magnetization mechanism.

Fig.2.7 shows the coercivity  $H_{cM}$  of the alloy in the optimum state as a function of the temperature  $T$ . As is seen, the "extra coercivity" that is gained by the exchange coupling of the soft  $m$ -phase to the hard  $k$ -phase decreases with rising  $T$  and vanishes at the Curie temperature of the hard phase  $Nd_2Fe_{14}B$  ( $T_{cK} = 580$  K, see Table-2.1).

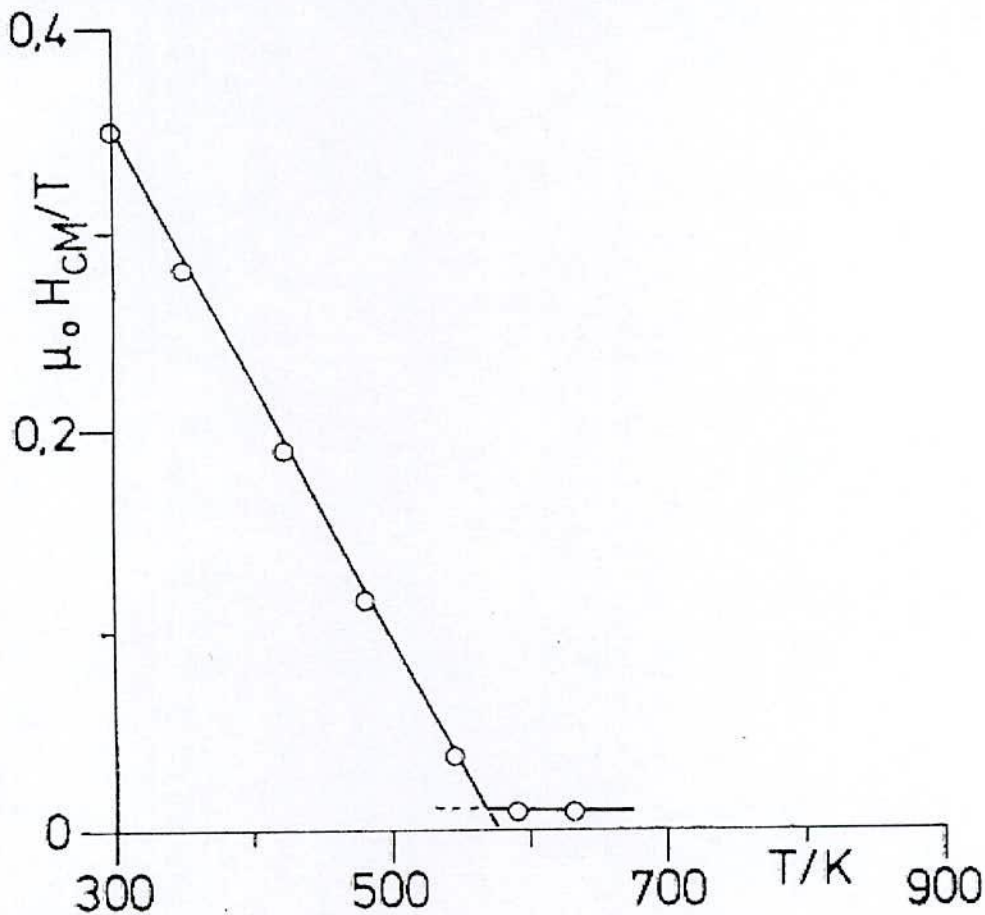


Fig.-2.7. Coercive force  $\mu_0 H_{cM}$  versus temperature  $T$  as measured on the alloy in the optimum magnetic state. The end of the steep decrease in  $H_{cM}(T)$  corresponds to the Curie temperature of the hard phase  $Nd_2Fe_{14}B$ ,  $T_{cK} = 580$  K. The low coercive force at  $T > 580$  K is that of the soft magnetic phases  $Fe_{23}B$ , ( $T_c = 698$  K) and  $Fe_3B$  ( $T_c = 783$  K). The curve is completely reversible.



**CHAPTER – 3**  
**AN OVERVIEW OF NANOCRYSTALLINE MATERIALS**

---

### 3.0 An Overview of Nanocrystalline Materials

#### 3.1 History of amorphous and nanocrystalline materials

The nanotechnology has its roots date back to a 1959 talk given by Richard Feynman ([http://nano, Xerox.com/nanotech/feynman.html](http://nano.Xerox.com/nanotech/feynman.html)) in which he said, "The principles of physics, as far as I can see, do not speak against the possibility of maneuvering things atom by atom. It is not an attempt to violate any laws; it is something in principle, that can be done; but in practice it has not been done because we are too big". But with the tremendous advancement of science and technology for the last two decades the idea that we should be able to economically arrange atoms in most of the ways permitted by physical law has gained fairly general acceptance. The recent advances in materials synthesis, characterization techniques and methods of advance measurement facilities on the nanometer scale have greatly assisted the expansion of nanotechnology.

These are various methods of preparing nanoparticles and / or nanostructured materials which include: (i) Plasma Processing<sup>(3.1, 3.2)</sup> (ii) desposition technique<sup>(3.3, 3.4)</sup> and (iii) rapid quenching and subsequently crystallized to nanometric grains embedded in a remaining amorphous matrix<sup>(3.5)</sup>. In the present work nanocrystalline alloys have been prepared by the last method.

Amorphous soft magnetic alloys are now well accepted and mature materials. At first the great interest in amorphous metals stems from reports by Duwaz *et al.*<sup>(3.6)</sup> on the preparation and properties of amorphous metallic alloys. Simpson and Brandley<sup>(3.7)</sup> appear to have been the first to point out that the amorphous alloys are expected to have no magnetocrystalline anisotropy and should have very low coercivity. Progress in this field is often characterized by further improvement according to specific requirements of particular applications. The first example for soft magnetic behavior in the nanocrystalline state was given by O' Handley *et al.*<sup>(3.8)</sup> for a devitrified glassy Co-based alloy. However, the soft magnetic properties were inferior than their amorphous counterpart. The most promising properties so far have been found in Fe-based alloys.



Therefore, the Co-based alloys after nanocrystallization by thermal treatment failed to show promising soft magnetic properties.

Amorphous alloys have enormous scientific and technological interest because they do not have any long-range atomic order. As a result these materials have high resistivities, low magnetocrystalline anisotropy and no microstructural inhomogeneities. As a result, these materials are observed to have small hysteretic and eddy current losses. Amorphous alloys are typically formed by rapid solidification processing rules; though more conventional solidification rules are possible for bulk amorphous alloys. The study of metallic glasses dates back to the pioneering work of Pol Duwez at Caltech in the 1950s. Duwez employed atomization<sup>(3.9)</sup> and gun techniques<sup>(3.10)</sup> prior to splat quenching<sup>(3.11-3.12)</sup>. Ferromagnetic amorphous alloys were first reported by Mader and Nowik<sup>(3.13)</sup>. Soon after, Tsuei and Duwez<sup>(3.14)</sup> reported splat quenched amorphous ferromagnets with interesting soft magnetic properties. Rapid solidification processing is reviewed only in a cursory manner here, citing techniques, which have been employed to produce materials.

### 3.2 Kinds of nanocrystalline alloys

Nanocrystalline amorphous ribbons can be considered as an off-shoot of amorphous materials. Infact nanocrystalline amorphous ribbons are composite materials where nanocrystals are embedded in an amorphous matrix. Nanocrystalline materials represent one of the most active research areas in recent times for the atomic tailoring of materials with specific properties and property combinations. However, it is still in its infancy since its emergence as potential materials has just begun at this stage of development.

Nanocrystalline alloys can be described in general as  $TL_{1-x}[TE, M, NM]_x$ , where TL denotes a late ferromagnetic transition metal element, TE is an early transition metal element, M is a metalloid and NM is a noble metal. This composition usually has  $x < 0.20$  i.e. with as much late ferromagnetic transition metals (TL of Co, Ni, or Fe) as



possible. The remaining early transition metals ( $TE = Zr, Nb, Hf, Ta$  etc.) and metalloids ( $M = B, P, Si$  etc.) are added to promote glass formation in the precursor. The noble metal elements ( $NM = Cu, Ag, Au$  etc.) serve as nucleating agents for the ferromagnetic nanocrystalline phase. The compositions are limited by where glass formation can occur prior to the nanocrystalline route. These alloys may be single phase (Type-I) but are generally two-phase materials with a nanocrystalline ferromagnetic phase and a residual amorphous phase at the grain boundaries (Type-II). The Type-II nanocrystalline alloys might have general properties:

- (i) Relatively high resistivity ( $50-80 \mu\Omega\text{-cm}$ )
- (ii) Low magnetocrystalline anisotropy and
- (iii) Increase mechanical strength. With properties such as these, nanocrystalline alloys have great potential as soft magnetic properties.

Nanocrystalline Fe-Cu-Nb-Si-B alloys have been patented by Yoshizawa *et al.* under the trade name FINEMET <sup>®</sup>TM<sup>(3.15, 3.16)</sup>. Soft materials based on Fe-M-Cu-B have been patented by Kojima *et al.*<sup>(3.17)</sup> under the trade name NANOPERM <sup>®</sup>TM. This Fe-M-Cu-B [ $M = Zr, Nb, Hf \dots$ ] nanocrystalline alloys have all been optimized to achieve small magnetostrictive coefficients and concomitant large permeabilities. More recently (Fe,Co)-M-Cu-B [ $M = Nb, Hf$  or  $Zr$ ] nanocrystalline alloys, called HITPERM have been shown to have attractive induction (1.6-2.1 Tesla) combined with high permeabilities and high Curie temperature. In FINEMETS  $\alpha$ -FeSi nanoparticles with a  $DO_3$  structure are observed and in NANOPERM  $\alpha$ -Fe particles with bcc structures are formed. In HITPERM alloys nanocrystalline  $\alpha$ -bcc and  $\alpha'$ -bcc, B2-FeSi (B2)-FeCo are formed with significantly improved high temperature magnetic properties than in the former two.

Nanocrystalline soft magnetic alloys have received considerable attention due to their excellent soft magnetic properties<sup>(3.18)</sup>. Small addition of Cu and Nb into Fe-Si-B amorphous materials changes considerably their crystallization process, which is executed under appropriately controlled conditions and the specific purpose of these addition are:

- The element Cu is used for helping the formation of nuclei of ultra fine grains and

- The element Nb is used to impede the growth of the crystallites.

In this material, the nanocrystalline state is composed of a fine structure of  $\alpha$ -Fe(Si) and is usually around 10 nm. For such an average grain size the exchange interaction dominates the magnetic behavior of randomly oriented crystallites guided by random anisotropy<sup>(3.19)</sup>.

### 3.3 Fe-based Soft Nanocomposite Magnetic Material

A new class of Fe-based alloys exhibiting superior soft magnetic properties has been discovered for the first time by Yoshizawa *et. al.*<sup>(3.15)</sup>. Nanocrystalline structure of these alloys offers a new opportunity for tailoring soft magnetic materials. The particular characteristic of these types of alloys is its ultrafine microstructure of b.c.c. Fe-Si with grain sizes of 10-15 nm for which their soft properties are derived and after which they were named nanocrystalline.

It is well known that the microstructure, especially, the grain size, essentially determines the hysteresis loop of ferromagnetic materials. The present understanding of the coercivity,  $H_c$ , in the whole range of structural correlation lengths starting from atomic distances in amorphous alloys over grain sizes,  $D$ , in the nanometer regime up to macroscopic grain sizes<sup>(3.20)</sup>. The permeability shows an analogous behavior being essentially inversely proportional to  $H_c$ . The  $\frac{1}{D}$  dependence of coercivity for large grain sizes reflects the conventional rule that good soft magnetic properties require very large grains ( $D > 100 \mu\text{m}$ ). Thus the reduction of particle size to the regime of the domain wall width increases the coercivity  $H_c$  towards a maximum controlled by the anisotropies of materials. Lowest coercivities, however, are again found for smallest structural correlation lengths like in amorphous alloys ("grainsize" of the order of atomic distances) and in nanocrystalline alloys for grain sizes  $D < 20 \text{ nm}$ . The new nanocrystalline material fills in the gap between amorphous metals and conventional poly-crystalline alloys.



### 3.3.1 Formation of Nanocrystalline State

A typical nanocrystalline structure with good soft magnetic properties occurs if the amorphous state is crystallized provided the primary crystallization of bcc Fe takes place prior to the formation of secondary inter metallic phases like Fe-B. Both an extremely high nucleation rate and slow growth of the crystalline precipitates are needed in order to obtain a nanoscaled microstructure. Such crystallization characteristic seems to be rather an exception case than the conventional rule. Thus, crystallization of conventional metallic glasses optimized for soft magnetic applications usually yield a relatively coarse grained microstructure of several crystalline phases and correspondingly, deteriorates the soft magnetic properties.

It has been established that controlled crystallization of the amorphous alloys in the form of their ribbons prepared by rapid solidification technique using melt-spinning machine appeared to be the most suitable method available until now to synthesize nanocrystalline alloys with attractive soft magnetic properties. The basic principle for the crystallization method from amorphous solids is to control the crystallization kinetics by optimizing the heat treatment conditions such as annealing temperature and time, heating rate, etc. The nanocrystalline state is achieved by annealing at temperatures typically between about 500°C and 600°C, which leads to primary crystallization of bcc Fe. Fig-3.1 summarizes the evolution of the microstructure and the soft magnetic properties with the annealing temperature. The resulting microstructure is characterized by randomly oriented, ultra fine grain of bcc Fe-Si, 20 at. % with typical grain size of 10-15 nm embedded in a residual amorphous matrix which occupies about 20-30 % of the volume and separates the crystallites at a distance of about 1-2 nm. These features are basis of the excellent soft magnetic properties indicated by the high values of the initial permeability of about  $10^5$  and corresponding low coercivities of less than 1 A/m. The nanocrystalline microstructure and the accompanying soft magnetic properties are rather insensitive to the precise annealing conditions within a wide range of annealing temperature ( $T_a$ ) = 525°C ~ 580°C which covers a temperature range  $\Delta T_a = 50^\circ\text{C} - 100^\circ\text{C}$ . This develops in a relatively short period of time (about 10-15 minutes) and do not improve much even



after prolonged heat treatment of several hours<sup>(2,21)</sup>. A typical heat treatment like 1h at 540°C in most cases yields a nanocrystalline microstructure to the quasi-equilibrium state and characteristic for the individual alloy composition.

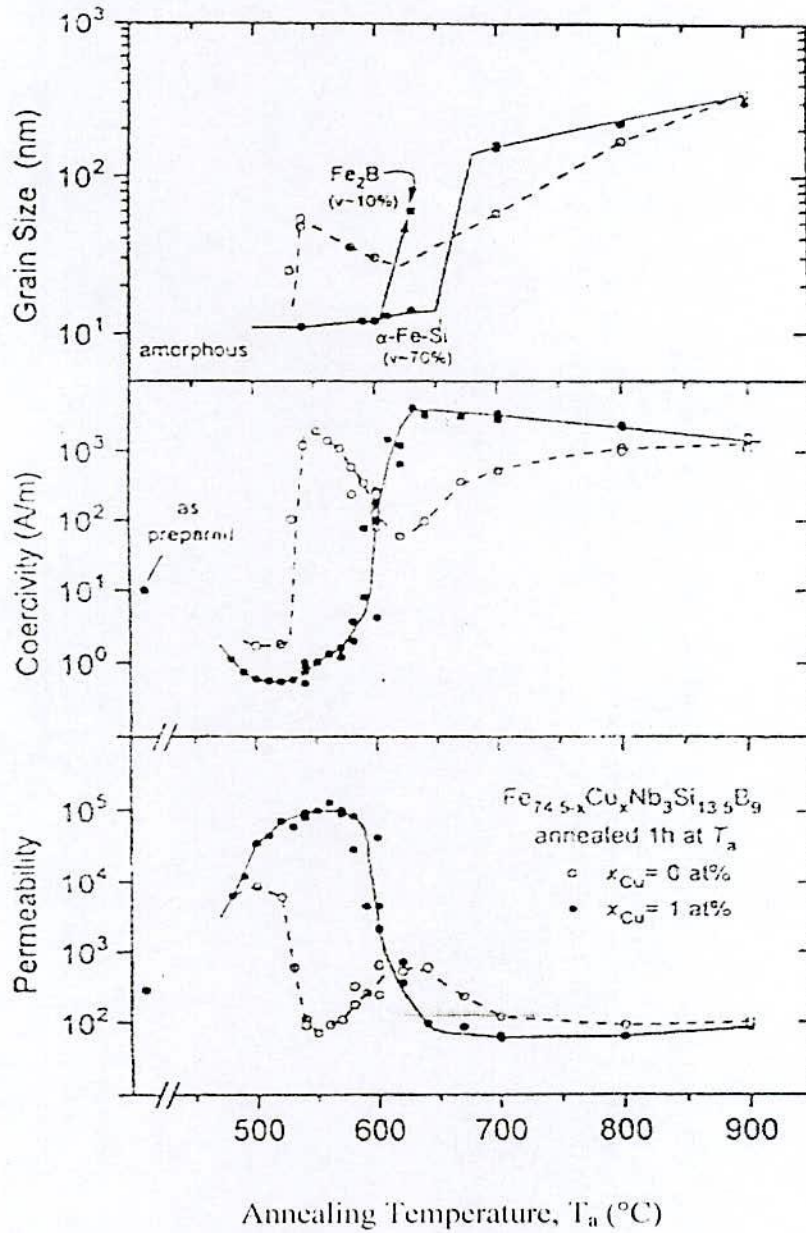


Fig. 3.1 Microstructure and soft magnetic properties with the annealing temperature

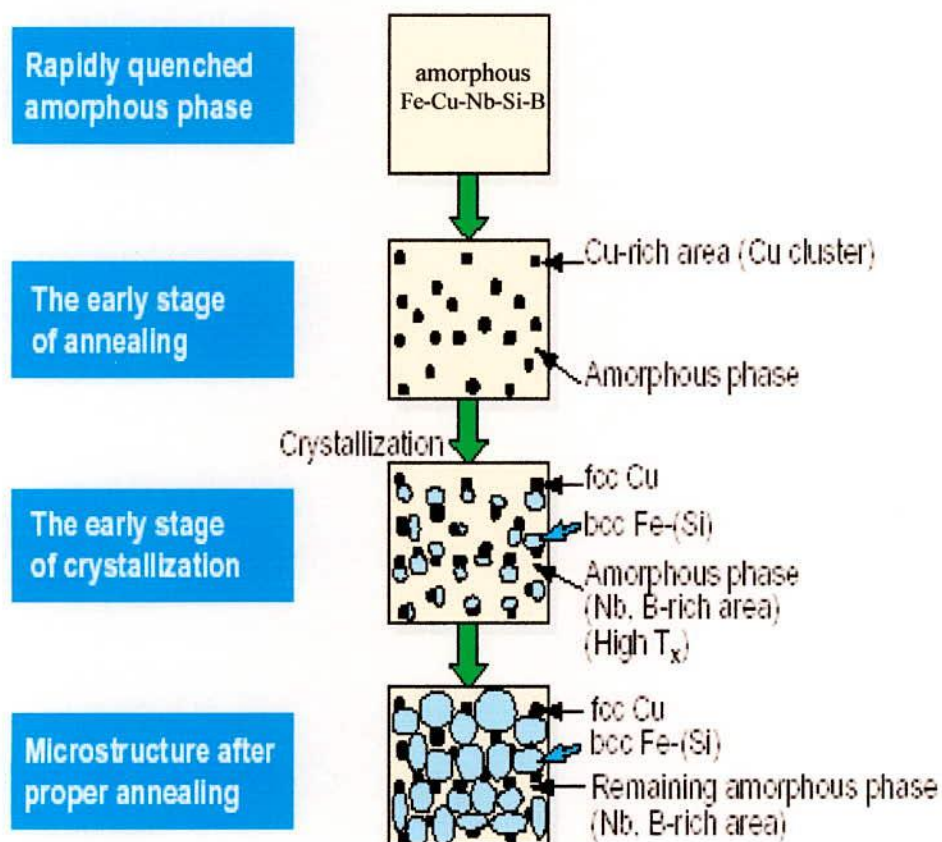


Fig.3.2 Schematic illustration of the formation of the nanocrystalline structure in Fe-Cu-Nb-Si-B alloys

Only annealing at more elevated temperature above about 600°C leads to the precipitation of small fractions of boride compounds like  $Fe_2B$  or  $Fe_3B$  with typical dimensions of 50 nm to 100 nm, while the ultra fine grain structure of bcc Fe-Si still persists. Further increase of the annealing temperature above about 700°C finally yields grain coarsening. Both the formation of Fe borides and grain coarsening deteriorates the

soft magnetic properties significantly. The evolution of microstructure during annealing is depicted schematically in Fig. 3.2 and summarized as follows according to Hono *et al.* (3.22-3.23)

At the initial stage of the annealing, Cu rich clusters are formed by either a spinodal process or nucleation in the amorphous state. Each cluster formation causes a concentration fluctuation of Fe also, since Cu substitutes for Fe. Because of this concentration fluctuation, the density for the nuclei of the bcc crystalline phase is increased significantly although the evidence of concentration fluctuation in the fully amorphous state has not been observed because the investigators<sup>(2.24)</sup> observed the Cu clusters and bcc phase simultaneously at the early stage of the nanocrystallization. Annealing slightly at higher temperature at the initial stage of crystallization  $\alpha$ -Fe(Si) phase forms. At this stage Nb and B are excluded from  $\alpha$ -Fe(Si) and are enriched in the remaining amorphous phase, because they are insoluble in the  $\alpha$ -Fe(Si) phase. This happens when the annealing treatment is carried out at around 550°C when Cu clusters are formed with a few nanometer diameters.

Thus the regions in between the Cu rich clusters provide a significantly increased density of nucleation sites for the crystallization of bcc Fe. The consequence is an extremely fine nucleation of bcc Fe-Si crystallites at a high rate, which subsequently grow in a diffusion-controlled process<sup>(2.25)</sup> as the annealing proceeds further. As annealing goes on the grain size of the  $\alpha$ -Fe (Si) increases. At the same time the Si content of this phase keeps increasing since Si tends to be partitioned to the bcc  $\alpha$ -Fe(Si) phase. Since the Nb and B enrichment in the amorphous phase stabilizes the remaining the amorphous phase, the grain growth of the bcc phase eventually stops. The presence of Nb at the same time inhibits the formation of Fe-B compounds. The Cu concentration of the clusters also increases as the crystallization proceeds.

At the optimum stage, three distinct phases are present based on the chemical compositions. As the bcc Fe-Si phase forms, Nb and B are excluded from the crystallites because of their low solubility in bcc Fe and are enriched in the residual amorphous matrix. At the same time effectively all Si tends to be partitioned into the bcc Fe-Si phase<sup>(2.25-2.26)</sup>. The enrichment with B and in particular, with Nb increasingly stabilizes the



residual amorphous matrix and, thus, hinders coarsening of the bcc grains. The presence of Nb at the same time inhibits the formation of Fe boride compounds. The transformation finally ceases in a metastable two-phase microstructure of bcc Fe-Si embedded in an amorphous Fe-Nb-B matrix. The significance of the Cu addition becomes apparent from Fig. 3.1.

### 3.3.2 Conditions for the formation of Nanocrystalline alloys

The essential conditions for preparing nanocrystalline materials are:

- (i) The magnetic properties are highly dependent on grain size; if the grain size is larger; the magnetic anisotropy would be very high, which in turn will have diverse effect on the soft magnetic properties specially the permeability.
- (ii) There should be nucleation centers initiated for the crystallization process to be distributed throughout the bulk of amorphous matrix.
- (iii) There must be a nucleation for stabilizing the crystallites.
- (iv) Nanocrystalline materials obtained from crystallization must be controlled so that the crystallites do not grow too big. The grain growth should be controlled so that the grain diameter is within 15-20 nm.
- (v) The size of the grains can be limited to nanometer scale by doping group-II metals are

→ Cu (Au.....)

→ Nb, W, Mo, Cr, Ta etc.

- (vi) The stability must be lower and the crystallization must be higher.

In addition to the understanding of the unusual properties possessed by nanophase materials, there are three other associated areas, which need serious attention:

- Identification and development of suitable preparation methods, especially those, which are capable of providing large industrial quantities of nanometer scale materials.
- Development of processing methods for manufacturing these materials into useful size and shapes without losing their desirable nanometer size feature and

- Identification of proper characterization methods, where the nanometer size range of these materials falls just below or at the resolution limit of the conventional tools.

### 3.3.3 Grain Size and Coercive force of Nanocrystalline alloys

In the conventional soft magnetic materials, “whose grain size is far larger than  $1\mu\text{m}$ ”, it is well known that soft magnetic properties become worse and coercive force increases when crystal grain size becomes smaller. For example, coercive force is thought to be inversely proportional to  $D_g$ . Therefore, main efforts to improve the soft magnetic properties are directed to make the crystal grain size larger and / or to make the magnetic domain size smaller by annealing and working.

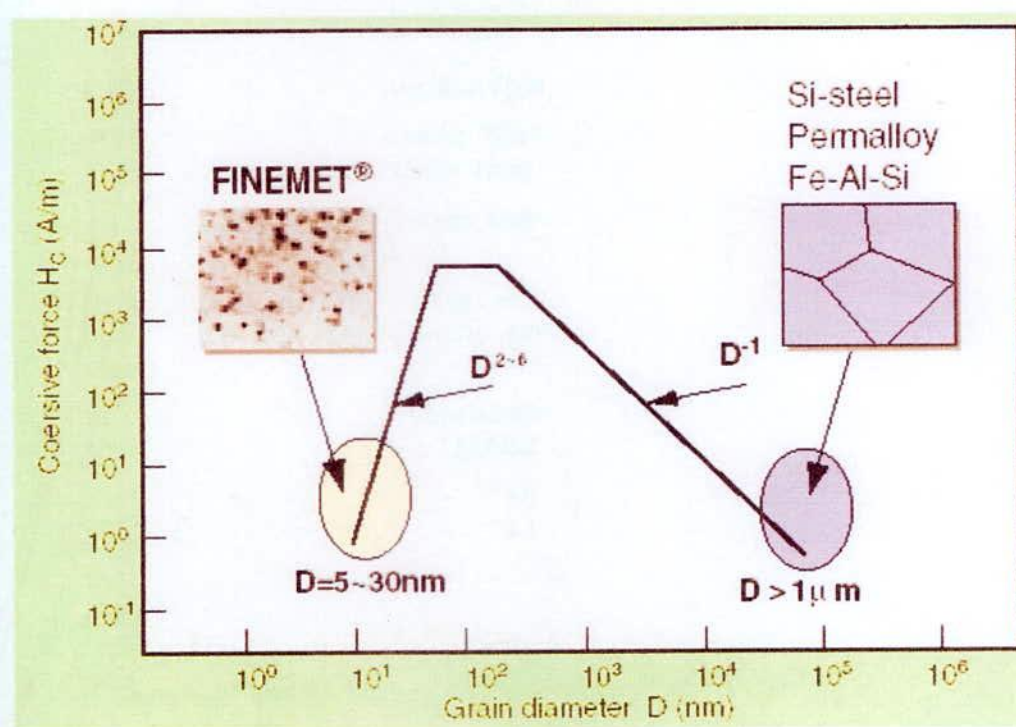


Fig. 3.4 Relation between grain diameter ( $D_g$ ) and coercive force ( $H_c$ )



However, FINEMET demonstrated a new phenomenon; reduction of grain size, "to a nano-meter level", improves the soft magnetic properties significantly. In this nano-world, the coercive force is directly proportional to grain size,  $D_g$  on the order of  $D_g^2$  to  $D_g^6$ .

### 3.4 Various Kinds of Energies in the Formation of Magnetic Domains

Domains are formed basically to reduce the magnetostatic energy which is the magnetic potential energy contained in the field lines connecting north and south poles outside of the material. When a large domain is split into  $n$  domains, the energy of the new structure is about  $\frac{1}{n}$ th of the single domain structure. In a ferromagnetic domain, there is parallel alignment of the atomic moments. Each domain becomes a magnet composed of smaller magnets. Domains contain about  $10^{12}$  to  $10^{15}$  atoms and their dimensions are on the order of microns ( $10^{-4}$  cm). Their size and geometry are governed by certain considerations.

The primary reason for the existence of domains within a crystal is that their formation reduces the magnetic free energy. In the simplest case for such a crystal, the energy,  $E$ , is the sum of several free energy terms:

$$E = E_{ex} + E_k + E_\lambda + E_D + E_H, \quad (3.1)$$

where  $E_{ex}$  is the exchange energy,  $E_k$  is the magnetocrystalline anisotropy energy,  $E_\lambda$  is the magnetoelastic energy,  $E_D$  is the magneto-static energy, and  $E_H$  is the energy of the domains in the presence of an applied field. There is also a wall energy  $E_w$ . However, since  $E_w$  comprises  $E_{ex}$  and  $E_k$ , it is not necessary to include  $E_w$  as a separate term in the equation [3.1].



### 3.4.1 Magnetostatic Energy

This is the energy contained in the magnetic field. It increases with the volume of the field. A piece of material consisting of a single domain would have a large magnetic field around it. The material could reduce its energy by splitting into domains oriented to allow the field lines to exist as loops inside the material, with little field outside. This is essentially the state of an unmagnetized ferromagnetic material.

### 3.4.2 Magnetostrictive Energy

This energy is due to the effect of magnetostriction, a slight change in the dimensions of the crystal when magnetized. This causes elastic strains in the lattice, and the direction of magnetization that minimizes these strain energies will be favoured.

### 3.4.3 Anisotropy in Ferromagnetic Materials

If any property or behavior of a crystalline material changes with to the directions in crystal it is termed anisotropic. Contrarily if the the property is unaffected by change in direction then it is isotropic. Ferromagnetic materials show considerable anisotropy in respect of magnetization. For example a crystal of iron which is b.c.c in nature will respond to a magnetic field differently when placed along  $\langle 111 \rangle$ ,  $\langle 110 \rangle$  or  $\langle 100 \rangle$  directions. In case of these materials the direction of easy magnetization is  $\langle 100 \rangle$  i.e, when crystal is so placed that H is acting along  $\langle 100 \rangle$  direction. The saturation will much earlier when it is placed with other two directions coinciding with the field. Thus directions  $\langle 111 \rangle$  and  $\langle 110 \rangle$  are hard magnetization directions in iron.

### 3.4.4 Anisotropy energy

The crystal lattice is 'easy' to magnetize in some directions and 'hard' to magnetize in others. Magnetization in the easy directions lowers this energy.

### 3.4.5 Zeeman Energy

Energy resulting from an externally applied field.

### 3.5 Magnetization and Magnetic Induction

Magnetization, or more completely, the intensity of magnetization  $I$ , is the total magnetic moment of dipoles per unit volume in units of  $\text{A.m}^2$  per  $\text{m}^3$  or  $\text{A.m}^{-1}$ . Considering a bar magnet of pole strength  $m$ , length  $l$  and cross-sectional area  $A$ , the vector quantity  $I$  has its direction pointing from the S pole to the N pole and its magnitude given by

$$I = \frac{M}{V} = \frac{m}{A} \quad (3.2)$$

So magnetization is also the pole strength per unit area in units of  $\text{A.m}^{-1}$ , which is equivalent to  $10^{-3}$  gauss ( $G$ ) in the CGS system.

Magnetic induction or magnetic flux density  $B$  is the flux per unit area and expressed in units of  $\text{Wb.m}^{-2}$  or tesla (T). By flux is meant the number of lines of induction crossing a given area at a right angle. The weber is the magnetic flux that, linking a circuit of one turn, produces in the circuit an electromotive force of one volt as the flux is reduced to zero at a uniform rate in one second. In free space a magnetic field produces a magnetic induction given by  $B = \mu_0 H$ . If the space filled with any magnetic substance in which the induced magnetization is  $\mu_0 I$ , the total induction now becomes

$$B = \mu_0 (H + I) \quad (3.3)$$

Thus both the magnetizing field and the magnetization contribute to the induction. For ferromagnetic materials, however, the contribution of  $I$  usually dominates  $B$ .

In the CGS system, since  $\mu_0 = 1$ , equ<sup>n</sup> (3.3) becomes

$$B = H + 4\pi I \quad (3.4)$$

The factor  $4\pi$  arises from the fact that a unit pole produces a unit field everywhere on the sphere of unit radius (1cm) enclosing the pole and the



surface area of this sphere is  $4\pi \text{ cm}^2$ . The unit of  $B$  in the CGS system is the popular gauss. One gauss is equal to one line of induction per  $\text{cm}^2$ . In the SI, as indicated by equ<sup>n</sup> (3.3),  $H$  and  $I$  have the same unit in  $\text{A.m}^{-1}$ . In the CGS system, since  $\mathbf{B} = \mathbf{H}$  in free space, gauss frequently is used to  $H$  in place of oersted. For conversion it is well to remember that one tesla is equivalent to  $10^4\text{G}$ .

### 3.6 Susceptibility and Permeability

To compare the magnetic response of various materials, we define the volume susceptibility, or susceptibility,  $\chi$  and the absolute permeability,  $\mu$  by

$$\chi = \frac{I}{H} \quad (3.5)$$

and

$$\mu = \frac{B}{H}, \quad (3.6)$$

where  $H$  is the applied magnetic field.



### 3.7 Theory of Permeability

Permeability is defined as the proportionality constant between the magnetic field induction  $B$  and applied intensity  $H$ ;

$$B = \mu H \quad (3.7)$$

This definition needs modification when magnetic material is subjected to an ac magnetic field given below;

$$H = H_0 e^{i\omega t} \quad (3.8)$$



In such a field the magnetic flux density experiences a delay with respect to  $H$ . The delay is used due to the presence of various losses and thus expressed as,

$$B = B_0 e^{i(\omega t - \delta)}, \quad (3.9)$$

where  $\delta$  is the phase angle and marks the delay of  $B$  with respect to  $H$ . The permeability is given by

$$\begin{aligned} \mu &= \frac{B}{H} = \frac{B_0 e^{i(\omega t - \delta)}}{H_0 e^{i\omega t}} \\ &= \frac{B_0 e^{-i\delta}}{H_0} \\ &= \frac{B_0}{H_0} \cos \delta - i \frac{B_0}{H_0} \sin \delta \\ &= \mu' - i\mu'' \end{aligned} \quad (3.10)$$

where 
$$\mu' = \frac{B_0}{H_0} \cos \delta \quad (3.11)$$

and, 
$$\mu'' = \frac{B_0}{H_0} \sin \delta \quad (3.12)$$

The real part  $\mu'$  of complex permeability,  $\mu$  as expressed in equ<sup>n</sup> (3.10) represents the component of  $B$ , which is in phase with  $H$  corresponds to the normal permeability. If there are no losses we should have  $\mu = \mu'$ . The imaginary part  $\mu''$  corresponds to that part of  $B$  which is delayed by phase angle  $90^\circ$  from  $H$ . The presence of such a component requires a supply of energy to maintain the alternating magnetization, regardless of the origin of delay. The ratio of  $\mu''$  to  $\mu'$  gives

$$\frac{\mu''}{\mu'} = \frac{\frac{B_0}{H_0} \sin \delta}{\frac{B_0}{H_0} \cos \delta} = \tan \delta \quad (3.13)$$

The  $\tan \delta$  is called the loss factor. The Q-factor or quality factor defined as the reciprocal of this factor, i.e.

$$Q = \frac{1}{\tan \delta} \quad (3.14)$$

### 3.8 Coercivity

In materials science, the **coercivity**, also called the **coercive field**, of a ferromagnetic material is the intensity of the applied magnetic field required to reduce the magnetization of that material to zero after the magnetization of the sample has been driven to saturation. Coercivity is usually measured in oersted or ampere/meter units and is denoted  $H_C$ .

When the coercive field of a ferromagnet is large, the material is said to be a **hard** or **permanent** magnet. Permanent magnets find application in electric motors, magnetic recording media (e.g. hard drives, floppy disks, or magnetic tape) and magnetic separation. A ferromagnet with a low coercive field is said to be **soft** and may be used in microwave devices, magnetic shielding, transformers or recording heads.

### 3.9 Various Kinds of Magnetism

We have stated at the outset that all substances display certain magnetic properties at all temperature, regardless of their composition and state. Now we shall review the various kinds of magnetism that have been observed in solids. Broadly speaking, there are five basic kinds of magnetism; namely, (i) diamagnetism, (ii) paramagnetism, (iii) ferromagnetism, (iv) ferrimagnetism and (v) antiferromagnetism. In simple terms, a solid is said to be diamagnetism if it is repelled by a permanent magnet and to be paramagnetic, ferromagnetic or ferrimagnetic if it is

attracted. A convenient way to define the first four kinds of magnetism is to use the susceptibility or relative permeability as follows:

**Table:-3.1 Susceptibility and relative permeability of four kinds of magnetism**

Criterion for classification	Diamagnetism	Paramagnetism	Ferro- or Ferrimagnetism
Susceptibility( $\chi$ )	$<0$	$\geq 0$	$\gg 0$
Relative Permeability ( $\mu$ )	$<1$	$\geq 1$	$\gg 1$

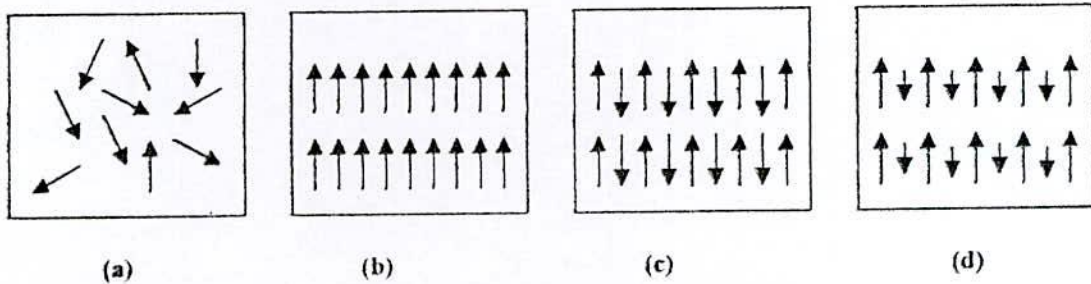


Fig.3.5 Spin arrangement in a crystal or domain illustrating (a) Paramagnetism, (b) Ferromagnetism, (c) Antiferromagnetism and (d) Ferrimagnetism

In the periodic table, various groups of elements are shown to display certain kinds of magnetism. For instance, inert gases and noble metals (Cu, Ag and Au) are diamagnetic, alkali metals (Li, Na, K and Rb) and all



transition metal except Fe, Co and Ni are paramagnetic, iron group transition metals and heavy lanthanide metals are ferromagnetic, etc. Ferrimagnetism exists only in compounds and alloys.

The spin arrangement in a crystal or domain illustrating (a) Paramagnetism, (b) ferromagnetism, (c) antiferromagnetism and (d) ferrimagnetism are shown in Figure 3.5

### 3.10 Origin of Magnetism (Quantum Mechanical View)

It is now recognized the magnetic behavior of atoms, molecules and solids is related to the orbital and spin motion of the negatively charged electrons. In the simplest case, (i.e. for hydrogen atom) the motion of the electron is governed by three quantum numbers: (i) principal quantum number  $n$ , where  $n = 1, 2, 3, \dots, (n-1)$ ; (ii) angular momentum (or orbital momentum) quantum number,  $l$ , where  $l = 0, 1, 2, \dots, (n-1)$ ; and (iii) magnetic quantum number  $m_l$ , where,  $m_l = 0, \pm 1, \pm 2, \dots, \pm l$ . While  $n$  determines the energy of the electron,  $l$  denotes the magnitude of the angular momentum vector  $\vec{L}$ ; the magnitude and orientation in space of the vector  $\vec{L}$  are determined by  $l$  and  $m_l$ . In other words, for a fixed value of  $n$ , different values of  $l$  and  $m_l$  describe the same energy state. The magnitude of the orbital angular momentum ( $L$ ) of the electron is quantized in terms of  $h$ , i.e.,

$$L = \sqrt{l(l+1)} \hbar \quad (3.15)$$

For,  $l = 0, 1, 2, \dots$  etc, the electrons are designated s, p, d, f etc. In the presence of a magnetic field, the z-component of  $\vec{L}$  is quantized such that,

$$L_z = m_l \hbar, \quad (3.16)$$

If  $\theta$  is the angle between  $\vec{L}$  and the magnetic field direction, which may be conveniently taken as the z-axis, then

$$\cos \theta = \frac{L_z}{L} = \frac{m_l \hbar}{\sqrt{l(l+1)\hbar}} = \frac{m_l}{\sqrt{l(l+1)}} \quad (3.17)$$

Equ<sup>n</sup>(3.16) and Equ<sup>n</sup>(3.17) indicate that  $L$  can have  $2l+1$  orientations in space, corresponding to the number of permissible values of  $m_l$ .

In addition to the orbital motion, an electron possesses spin angular momentum also, represented by the vector  $\vec{S}$ , whose magnitude is quantized in terms of  $\hbar$  such that,

$$|\vec{S}| = \sqrt{s(s+1)\hbar}, \quad (3.18)$$

where  $s = \frac{1}{2}$  is the spin quantum number. In the presence of an external field, the z-component of  $\vec{S}$  is also quantized such that

$$S_z = m_s \hbar, \quad (3.19)$$

where  $m_s = \pm \frac{1}{2}$  is the spin magnetic quantum number. The orientations in space of  $\vec{S}$ , with respect to z-axis (magnetic field direction), are determined by the relation,

$$\cos \phi = \frac{S_z}{S} = \frac{m_s \hbar}{\sqrt{s(s+1)\hbar}} = \frac{m_s}{\sqrt{s(s+1)}}. \quad (3.20)$$

Since,  $m_s = \pm \frac{1}{2}$ , there are only two permissible values of  $\phi$ .

If  $\vec{J}$  is the total angular momentum vector, then

$$\vec{J} = \vec{L} + \vec{S} \quad (3.21)$$

$$\text{and } J = \sqrt{j(j+1)\hbar}, \quad (3.22)$$

where,  $j$  is the total angular momentum quantum number. The z-component of  $\vec{J}$  is also quantized such that

$$J_z = m_j \hbar \quad (3.23)$$

and

$$\cos \alpha = \frac{J_z}{J} = \frac{m_j \hbar}{\sqrt{j(j+1)}\hbar} = \frac{m_j}{\sqrt{j(j+1)}} \quad (3.24)$$

Here  $m_j$  is the total magnetic quantum number and  $\alpha$  is the angle between  $\vec{J}$  and the magnetic field direction. Further, if  $\beta$  is the angle between  $\vec{L}$  and  $\vec{S}$  and the vectors couple to give  $\vec{J}$ , then

$$\cos \beta = \frac{j(j+1) - l(l+1) - s(s+1)}{2\sqrt{l(l+1)}\sqrt{s(s+1)}} \quad (3.25)$$

### 3.11 Magnetism of the Electron

The magnetic dipole moment ( $M_l$ ) associated with a circulating electron is given by,

$$\begin{aligned} M_l &= \text{permeability of free space} \times \text{current} \times \text{area of the circulating orbit} \\ &= \mu_0 \times I \times \pi r^2, \end{aligned} \quad (3.26)$$

where  $r$  is the radius of the orbit and  $I = \frac{ev}{2\pi r}$ . Here  $e$  and  $v$  are respectively the electronic charge and (linear) velocity.

Therefore,

$$M_l = \mu_0 \times \frac{ev}{2\pi r} \times \pi r^2 = \frac{\mu_0 evr}{2} \quad (3.27)$$

Since  $L = m_e vr$ , where is the electronic mass, we can show that

$$\vec{M}_l = -\left(\frac{\mu_0 e}{2m_e}\right)\vec{L}$$



$$\vec{M}_l = \frac{\mu_0 e \hbar}{2m_e} \sqrt{l(l+1)} \quad (3.28)$$

The negative sign in Eq (1.5.2(a) ) indicates that  $\vec{M}_l$  and  $\vec{L}$  are in opposite directions. A fixed quantity  $\frac{\mu_0 e \hbar}{2m_e}$  consisting of universal constants occurs on the right hand side of eq (1.5.2(b)) is called the **Bohr magneton** ( $\mu_B$ ) and is taken as a unit for magnetic moment. Its value is  $1.165 \times 10^{-29}$  weber-metre. Thus

$$\vec{M}_l = -\left(\frac{\mu_B}{\hbar}\right) \vec{L} \quad (3.30)$$

$$\text{or} \quad \frac{\vec{M}_l / \mu_B}{\vec{L} / \hbar} = -1 \quad (3.31)$$

The left hand side of eq (1.5.3) represent the ratio of the magnetic moment vector in terms of Bohr magnetons to the orbital angular momentum vector in terms of  $\hbar$ . This ratio is called the **gyromagnetic ratio** (is represented by  $g_l$ ). Then,

$$\frac{\vec{M}_l / \mu_B}{\vec{L} / \hbar} = g_l, \quad (3.31)$$

where,  $g_l$  is also called the **Lande g factor**. It has a value of -1 for orbital motion.

One can obtain similar expressions for magnetic moments associated with spin and total angular momenta of a valence electron in an atom;

$$M_s = g_s \mu_B \sqrt{s(s+1)} \quad (3.32)$$

$$M_j = g_j \mu_B \sqrt{j(j+1)}, \quad (3.33)$$

where is given  $g_j$  by ,

$$g_j = 1 + \frac{j(j+1) + s(s+1) - l(l+1)}{2j(j+1)} \quad (3.34)$$

Further,  $|g_l| = 2$  for the electronic spin motion.

We know that, when a coil of conductor carrying a current is placed in a uniform magnetic field, it is subjected to a torque given by  $\vec{M} \times \vec{H}$ . So the change in energy  $\delta E_l$  (due to the interaction with the field) is equal to  $-\vec{M}_l \cdot \vec{H} = -M_l H \cos \theta$ ; where  $\theta$  is the angle between  $\vec{M}_l$  and  $\vec{H}$ . The interaction leads to precession of  $\vec{M}_l$  around  $\vec{H}$  such that  $\theta$  and  $\delta E$  do not change. The precession obviously occurs only at discrete values of  $\theta$  and is called the *Larmor precession*, the uniform angular frequency of precession is known as the *Larmor frequency* ( $\omega_l$ ). Thus,

$$\omega_l = g_l \left( \frac{eB}{2m_e} \right) = g_l \left( \frac{e\mu_0 H}{2m_e} \right) \quad (3.35)$$

similarly, 
$$\nu_l = \frac{eB}{4\pi m_e} \quad (3.36)$$

where the linear frequency  $\nu_l$  is given by  $\omega_l = 2\pi\nu_l$ .

### 3.12 Orbital Angular Momentum and Magnetic Moment

The electronic spin angular momentum is unaffected by its environment and it can be 'quenched' only when a chemical bond is formed, in keeping with the Pauli exclusion principle.

The orbital angular momentum arises from rotational motion of the electron about the nucleus in the simple Bohr model. From the wave mechanical point of view, the orbital momentum is associated with the interchange (or transformation) of one orbital with another by rotation about an approximate axis. This is possible if (a) orbitals are degenerate, (b) orbitals are in the same shape, (c) both orbitals do not contain electrons of the same spin.

The above condition can be best understood by considering the free 3d ion case. It is observed that:

- (i) The  $d_{xy}$ ,  $d_{yz}$ ,  $d_{xz}$  orbital can transform into one another by rotations of  $90^\circ$  about the approximate axes.
- (ii) A  $45^\circ$  rotation of the  $d_{xy}$  orbital about the z- axis can transform it into the  $d_{x^2-y^2}$  orbital. Similar with the case with  $d_{yz}$  and  $d_{xz}$  orbital.
- (iii) For the high- spin  $d^5$  configuration, the orbital angular momentum will be 'quenched' since all the orbital will contain electrons of the same spin.

When a 3d metal ion is placed in a crystal field , say , octahedral field , then the degeneracy of the orbitals is lifted and splitting shown in fig below is observed.

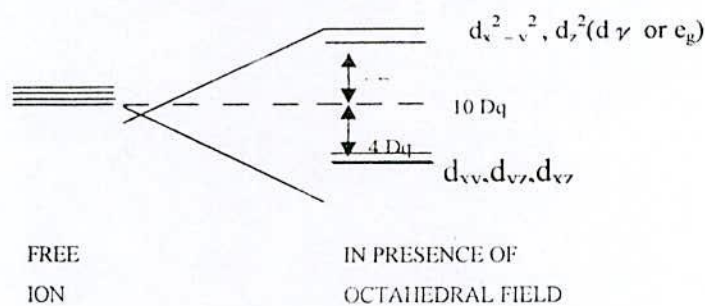


Fig.-3.6 Splitting of energy levels of d orbital in an octahedral crystal field

Now the interchange between the  $d_{x^2-y^2}$  and  $d_{z^2}$  orbitals is not permitted, since their shapes are different ( see fig 1.6). Similarly  $d_{x^2-y^2}$  and  $d_{xy}$  orbitals are no longer degenerate and their orbital contribution will be 'quenched'. However  $d_{xy}$ ,  $d_{yz}$ ,  $d_{xz}$  orbitals are still equivalent in energy ; but, for an ion with  $d^3$  configuration , no vacant equivalent , degenerate orbital of the same shape will be available. For  $d^1$  and  $d^2$  configurations, however , a finite , orbital angular momentum will exist .

For configurations  $d^6$ -  $d^9$ , the relative strength of crystal field ( $\Delta$ ) and the exchange ( or pairing) energy ( $\Delta_{ex}$ ) as also the type of the crystal field, will play a role in determining the magnitude of the orbital angular momentum . We know that the exchange



energy is the energy required to force two electrons to pair in the same orbital. When  $\Delta_{\text{ex}} > \Delta$ , the configurations are referred to as 'high - spin' or 'spin free' and when  $\Delta_{\text{ex}} < \Delta$ , these are referred to as 'low - spin' (or 'spin - paired').

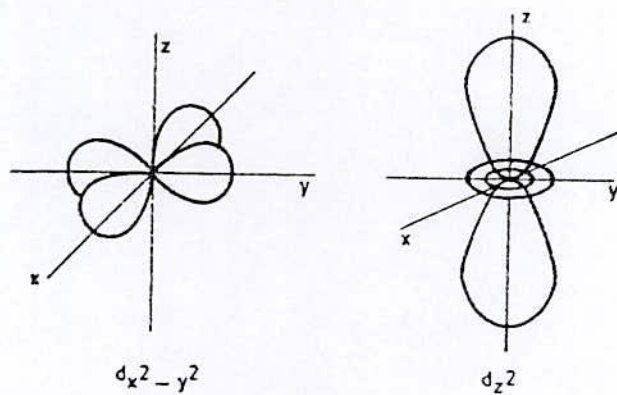


Fig .-3.7 The shape of the  $d_{x^2-y^2}$  and  $d_{z^2}$  orbital

**CHAPTER – 4**  
**PREPARATION OF NANOCRYSTALLINE ALLOY**

## 4.0 Preparation of Nanocrystalline Alloy

### 4.1 Methods used for Preparation of Nanocrystalline Alloy

There are various techniques in use to produce a metallic alloy in an amorphous state whose the atomic arrangement have no long-range periodicity. The methods are generally classified into two groups

- (i) The atomic deposition methods
- (ii) The fast cooling of the melt.

As we know, controlled crystallization from the amorphous state is the only method presently available to synthesize nanocrystalline alloys with superior soft magnetic properties. In this thesis work amorphous ribbons have been prepared by fast cooling of the melt.

#### 4.1.1 The Fast Cooling of the Melt

The molten alloy must be cooled through the temperature range from the melting temperature ( $T_m$ ) to the glass transition temperature ( $T_g$ ) very fast allowing no time for crystallization. The factors controlling  $T_g$  and crystallization are both structural and kinetic. Atomic arrangement, bonding and atomic size effect are related in the structural factors. The structural factors as discussed by Turnbull <sup>(4.1)</sup> are the nucleation, crystal growth rate and diffusion rate compared to the cooling rate. The methods using the principle of fast cooling of melt techniques are:

- (i) The gun techniques
- (ii) Single roller rapid quenching techniques
- (iii) Double roller rapid quenching techniques
- (iv) Centrifuge and rotary splat quenching techniques
- (v) Torsion catapult techniques
- (vi) Plasma-jet spray techniques
- (vii) Filamentary casting techniques



- (viii) Melt extraction techniques
- (ix) Free-jet spinning techniques
- (x) The melt spinning techniques

Among the techniques, the single roller rapid quenching technique is widely used to prepare amorphous ribbons.

## 4.2 Sample Preparation

### 4.2.1 Master alloy Preparation

Amorphous ribbons with the nominal composition  $\text{Nd}_3\text{Tb}_1\text{Fe}_{76}\text{Cu}_{0.5}\text{Nb}_1\text{B}_{18.5}$  was prepared in an arc furnace on a water-cooled copper hearth under an atmosphere of pure Ar. Their purity and origin of the constituent elements were Nd (99.9%), Tb (99.9), Fe (99.9 %), Nb (99.9 %), Cu (99.9 %) and B (99.9 %) as obtained from Johnson Matthey (Alfa Aesar Inc.). The required amounts of constituent elements were taken from pure metal bars or flakes, weighed carefully with a sensitive electronic balance and placed on the copper hearth inside the arc furnace. Before melting the furnace chamber was evacuated ( $10^{-4}$  torr), and flashed with Ar gas. The process was repeated several times to get rid of residual air and finally the furnace chamber were kept in an Ar atmosphere.

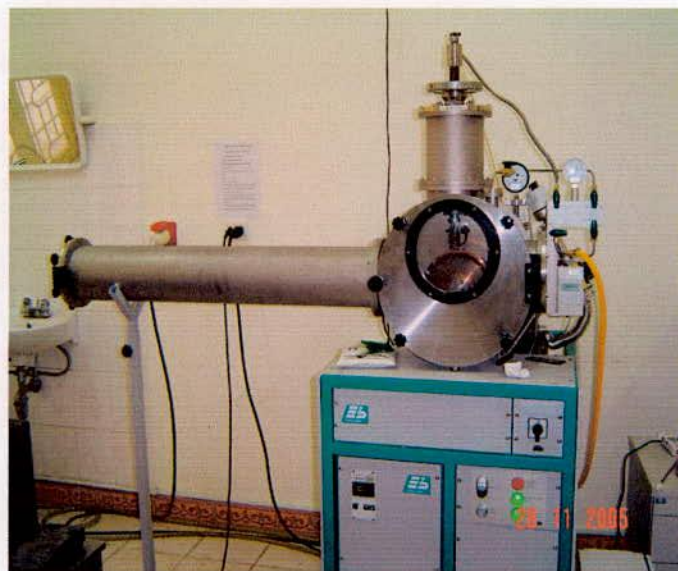


Fig. 4.1 Vacuum arc Melting Machine



A substantial amount of pure Titanium getter, placed inside of the chamber on the side of the copper hearth was melted first in order to absorb any oxygen present in the furnace chamber. The constituent elements were then melted in the shape of buttons. The arc melting facilities used to prepare the samples are installed at the Centre for Materials Science, National University of Hanoi, Vietnam. The arc furnace used in the preparation of master alloy is shown in Fig. 4.1.

#### 4.2.2 Preparation of ribbon by Melt Spinning Technique

Melt-Spinning is a widely used production method for rapidly solidifying materials as well as preparing amorphous metallic ribbon <sup>(4.2-4.3)</sup>. In order to prepare amorphous of  $\text{Nd}_3\text{Tb}_1\text{Fe}_{76}\text{Cu}_{0.5}\text{Nb}_1\text{B}_{18.5}$  alloy, a melt spinning facilities was used at the Centre for Materials Science, National University of Hanoi, Vietnam. The arc melted master alloy was crashed into small pieces and put inside the quartz tube crucible for re-melting by induction furnace using a medium frequency generator with a maximum power of 25 kW at a nominal frequency of 10 kHz.



Fig. 4.2 Melt-Spinning Machine



Fig. 4.2 shows the pictorial view of the melt-spinning machine. The quartz crucible has in its bottom part a rectangular nozzle tip of 8 mm length and 0.7 mm width. The position of the nozzle tip can be adjusted with respect to the copper wheel surface, so that the molten alloy was perpendicularly ejected onto the wheel surface from a distance of about 0.3 mm. The small pieces of the master alloy samples were inductively remelted inside the quartz tube crucible followed by ejecting the molten metal with an over pressure of 250 mbar of 99.9 % pure Ar supplied from an external reservoir through a nozzle onto a rotating copper wheel with surface velocity of 30 m/sec. The temperature was monitored by an external pyrometer from the upper surface of the molten alloy through a quartz window. The metal alloys were ejected at a temperature of about 150-250 K above the melting point of the alloy. The resulting ribbon samples had thickness of about 20-25  $\mu\text{m}$  and width of  $\sim 6$  mm. Processing parameters such as the thermal conductivity of the rotating quench wheel, wheel speed, ejection pressure, thermal history of the melt before ejection, distance between nozzle of quartz tube and rotating wheel, as well as processing atmosphere have influence on the microstructure and properties of melt-spun ribbons.

The lower pressure of 250 mbar as mentioned above stabilizes the turbulence between melt pull and rotating copper wheel enhancing the heat transfer resulting in a more uniform quenching. As a result, a more uniform ribbon microstructure can be obtained at relatively low wheel speed. With increasing wheel speeds for a given ejection rate, the increasing extraction rate results in thinner ribbons.

### 4.3 Important Factors to Control the Thickness of Ribbons

(i) Rotating speed:

- Angular velocity  $\omega = 2000$  rev/min
- Surface velocity  $V = 20$  m/s to 30 m/s

(ii) Gap between nozzle and rotating copper drum  $h = 200$  to 30  $\mu\text{m}$

(iii) Oscillations of rotating copper drum both static and dynamic have maximum displacement 1.5 to 5  $\mu\text{m}$ .

(iv) Pressure = 0.2 to 0.3 bar argon atmosphere.



- (v) Temperature of molten metals  $T_m \cong 1500^\circ\text{C}$ ; other wise quartz tube would be melted.
- (vi) A steady flow of the molten metal on the surface of the rotating drum needs to be ensured.

#### 4.4 Confirmation of Amorphousity of Ribbons

The amorphousity of the ribbons has been checked by X-ray diffraction using  $\text{Cu-K}_\alpha$  radiation using Philips (PW 3040) X 'Pert PRO XRD System located at Materials Science Division, Atomic Energy Centre, Dhaka (AECD). From the XRD pattern of the ribbon sample is no peaks are observed within the scanning range. Although there is a small hump is shown in diffraction pattern around  $2\theta = 45^\circ$ , but it cannot be regarded due to the crystalline effects. So from the over all pattern of the X-ray diffraction it is confirmed that both the samples are in amorphous state.

#### 4.5 X-ray Diffraction (XRD)

The German Physicist Wilhelm Roentgen discovered X-rays in 1895. X-rays are electromagnetic waves of short wavelengths in the range of  $10^{-2}$  to  $10^2 \text{ \AA}$ . Unlike ordinary light, these rays are invisible, but they travel in straight lines and affect photographic film in the same way as light. On the other hand, they were much more penetrating than light and could easily pass through the human body, wood, quite thick pieces of metal and other "opaque" objects.

The XRD provides substantial of information on the crystal structure. XRD is one of the oldest and effective tools for the determination of the atomic arrangement in a crystal. The wavelength ( $1\text{\AA}$ ) of an X-ray is the same order of magnitude as the lattice constant of crystals and it is this which makes X-rays so useful in structural analysis of crystal. When ever X-rays are incident on a crystal surface, they are reflected from it. The reflection abides by the Bragg's Law as given below

$$2d \sin \theta = n\lambda, \quad (4.1)$$

where  $d$  is the distance between crystal plane,  $\theta$  is the incident angle,  $\lambda$  is the wavelength of the X-ray and  $n$  is a positive integer. Bragg's Law also suggested that the diffraction is only possible when  $\lambda < 2d$ .

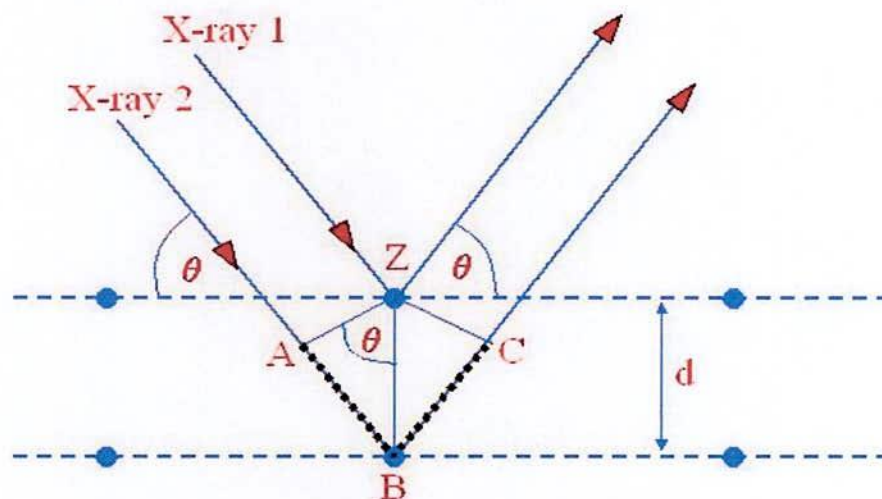


Fig.4.3: Bragg's diffraction pattern.

X-ray diffractograms of all the samples were recorded using monochromatic  $\text{Cu-K}\alpha$  radiation ( $\lambda = 1.54053 \text{ \AA}$ ) to ensure the formation of single-phase nature of the sintered product. XRD patterns information are: scanning speed  $2^\circ$ , chart speed 20 mm, starting from  $25^\circ$  and ending at  $95^\circ$ . Peak intensities are recorded corresponding to their  $2\theta$  values. The inter planner distance  $d$  was calculated from these  $2\theta$  values of the diffraction peaks using the Bragg's Law (In Fig. 4.3).

#### 4.5.1 X-ray Powder Method

Powder method is perhaps the most widely used X-ray diffraction technique for characterizing materials. The term 'powder' really means that the crystalline domains are randomly oriented in the sample. Therefore, when the 2-D diffraction pattern is recorded,



it shows concentric rings of scattering peaks corresponding to the various  $d$  spacing in the crystal lattice. The positions and the intensities of the peaks are used for identifying the underlying structure (or phase) of the material. Powder diffraction data can be collected using either transmission or reflection geometry, as shown in Fig. 4.4 below.

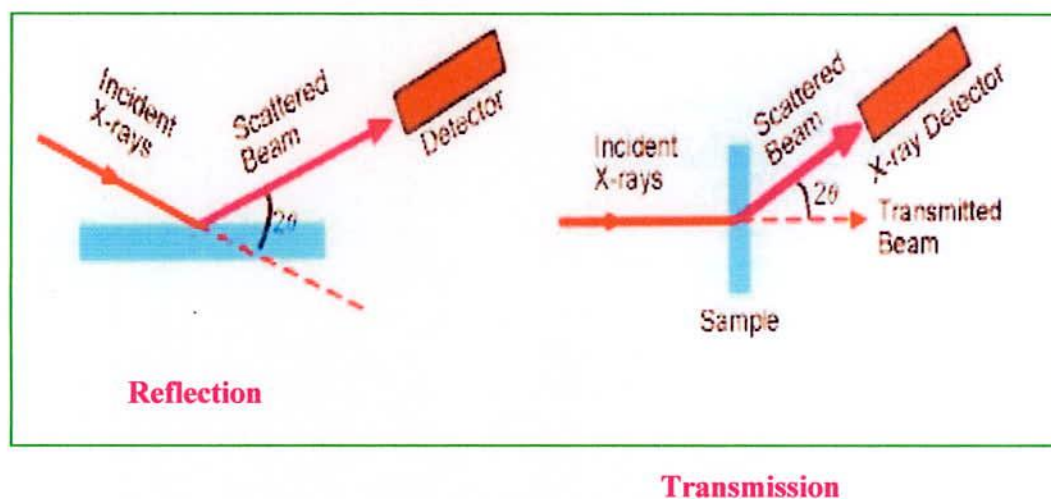


Fig.4.4 Reflection and Transmission geometry of powder diffraction

Because the particles in the powder sample are randomly oriented, these two methods will yield the same data. Powder diffraction data are measured using the Philips X'PERT MPD diffractometer, which measures data in reflection mode and is used mostly with solid samples, or the custom built 4-circle diffractometer, which operates in transmission mode and is more suitable for liquid phase samples.

#### 4.5.2 Experimental Technique for X-ray Diffractometer

X-ray diffraction (XRD) is a versatile non-destructive analytical technique for identification and quantitative determination of various crystalline phases of powdered or solid samples of any compounded. For each set of composition, ribbons are cut into several pieces; each of length 20 mm. Heat treatment was performed on the amorphous ribbons using a naber muffle furnace, where each piece of ribbon was wrapped by



aluminum foil separately. After heat treatment, samples were removed from the aluminum foil carefully and kept separately for XRD experiment. For XRD experiment each sample was set on a glass slides and fixed the sample by putting adhesive tape at the two ends of the sample.

After the pattern is obtained the value of  $2\theta$  is calculated for each diffraction line; set of  $2\theta$  values is the raw data for the determination of the lattice parameters of the unit cell. Fig. 4.5: Shows the block diagram of Phillips PW 3040 X'Pert PRO X-ray diffractometer.

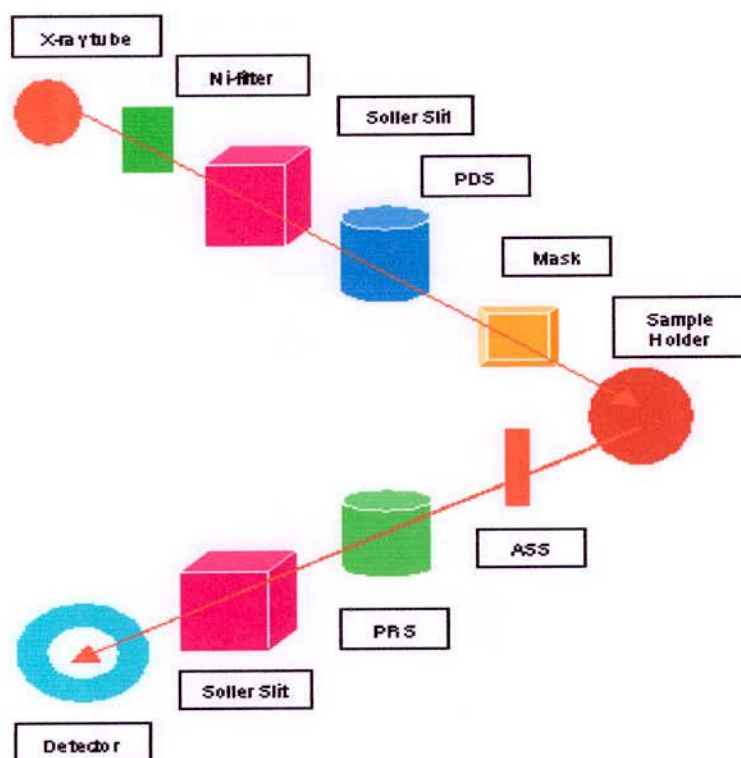


Fig. 4.5 Block diagram of the PHILIPS PW 3040 X'Pert PRO XRD system

A PHILIPS PW 3040 X'Pert PRO X-ray diffractometer was used for the lattice parameter determination in the Materials Science Division, Atomic Energy Centre, Dhaka. Fig.4.6 shows the inside view of the X'Pert PRO XRD system. The X'Pert Pro

- **Optics:** Focussing and parallel PreFix optics, programmable slits, tunable diffracted beam monochromator.
- **Detectors:** Xe proportional counter and solid state X'cellerator
- **Sample stages:** Single sample holder, 15-sample changer, sample spinning capability
- **Variable temperature capability:** Anton-Paar 77 to 725 K and 300 to 1475 K cameras
- **Software and databases:** ICDD PDF-2 database (2002). Hi-Score search-match software, X' Pert Plus crystallographic analysis software with Rietveld capability, ProFit line profile analysis software.
- **Instrument statistics:** The system uses Cu-K<sub>α</sub> radiation that has a wavelength of 1.54Å. Analysis are commonly run using a 40 kV 45mA X-ray tube voltage, a 0.04° solar slits, 1° divergence and antiscatter slits, and ½° (for powder) or ¼° (for clays) receiving slit.

### 4.5.3 Analysis of XRD Data

The XRD data consisting of  $\theta_{hkl}$  and  $d_{hkl}$  values corresponding to the different planes from which the following structural information of the nanocrystalline ribbon sample was evaluated.

- (i) Identification of phases
- (ii) Lattice parameter determination
- (iii) Average grain size determination
- (iv) Si- content determination in nanograins

#### (i) Identification of Phases

X-ray diffractometer has become a very popular and useful instrument for routine X-ray analysis of ribbon samples. In fact the diffractometer technique is often preferred to Debye-Scherrer technique owing to its several inherent merits. The most striking difference between the two methods is in the use of different intensity detection and measuring devices. XRD pattern of as-cast indicates just amorphous pattern of said

composition. The XRD patterns are identified as bcc  $\alpha$ -Fe(Si) solid solution, which are developed on the amorphous ribbon after heat treatment. The peak pattern is observed for all the samples at different heat treatment temperatures indicating the bcc  $\alpha$ -Fe(Si) phase, which is developed on amorphous ribbons after heat treatment. Present experiment reveals that 450°C is not sufficient temperature to start forming of crystalline nanograins of bcc Fe(Si) on the amorphous ribbon of the studied alloy composition.

### (ii) Lattice Parameter Determination

Lattice parameter of crystalline bcc Fe-Si nanograins has been determined for all the two different amorphous compositions at different heat treatment temperatures. Normally, lattice parameter of an alloy composition is determined by the Debye-Scherrer method after extrapolation of the curve. In this method, at least five fundamental reflections are required to determine lattice parameter. In the present case, only one reflection (110) is prominent in all XRD patterns and we would like to understand how the value of lattice parameter changes with annealing temperature. We have, therefore, determined the lattice parameter using only that particular reflection using equation  $2d \sin \theta = \lambda$  and  $a_0 = d\sqrt{2}$ , where  $\lambda = 1.54178 \text{ \AA}$  for  $Cu - K_{\alpha}$  radiation and  $a_0$  is the determined lattice parameter within an error estimated to be  $\pm 0.0001 \text{ \AA}$ .

### (iii) Grain Size Determination

The main aim (vital point) of the present study is to determine the nanocrystalline grain size for all the heat treated samples of the alloy composition by using Scherrer method. The XRD pattern of (110) reflection for different steps of heat treatment temperature of the alloy composition is used to calculate grain size. Grain size is determined using the following formula,

$$D_g = \frac{0.9\lambda}{\beta \cos \theta}, \quad (4.2)$$



where  $\lambda = 1.54178 \text{ \AA}$  for  $Cu - K_{\alpha}$  radiation and  $\beta = \text{FWHM}$  (full width at half maximum) of the peak in radian. Considering  $\beta$  in degree we get the following relation

$$D_g = \frac{79.5}{\beta \cos \theta} \quad (4.3)$$

All the values of grain size for every steps of heat treatment temperature of the alloy composition were determined. The FWHM of the peak is large at the early heat treatment temperature and with the increase of heat treatment temperature the value of FWHM becomes smaller which means that the grain size is increasing gradually.

#### (iv) Si-content in Nanograins

Crystalline nanograins were formed on the amorphous matrix of the ribbon in the process of heat treatment having the composition of Fe-Si. It is, therefore important to determine the concentration of Fe and Si in the nanograin. As because the alloy consists of Fe and Si and we have experimentally determined the lattice parameter of the alloy nanograin for the two compositions at different temperatures. It is easy to calculate the Si content in the nanograins from the data of Pearsons who was established the relationship between the lattice parameter as dependent on Si content in Fe-Si alloys covering a wide range of composition [5.2]. From the relationship, we have constructed a simple equation to calculate Si content from lattice parameter. The equation is

$$X = \frac{(a_0 - 2.8812)}{0.0022}, \quad (4.4)$$

where X is at.% Si in the nanograins,  $a_0$  is the determined lattice parameter of nanograins. Si-contents for the nanograins develop during the isothermal annealing at various temperatures have been calculated.

## 4.6 Thermal Treatment of the Amorphous Ribbon

In order to study nanocrystallization behavior by XRD and magnetic properties upon evaluation of nanocrystalline phase on amorphous matrix thermal treatment i.e. annealing is required to perform. For XRD, as prepared amorphous ribbon were cut into small pieces of about 2 cm lengths and for magnetic measurement such as permeability toroidal core were wound for annealing treatment. A laboratory built vacuum system made by quartz tube capable of evaluating up to  $10^{-5}$  torr was used for their purpose. The samples were put into the quartz tube and evaluated ( $10^{-5}$  torr) before it had been put inside the tabular furnace heated to a present temperature and kept for the time required to complete the annealing. In this way all the isothermal annealing as a function of time were performed.

## 4.7 SQUID Magnetometers

A SQUID (Superconducting Quantum Interference Device) is the most sensitive available device for measuring magnetization. Based on this sensitive device the so-called 'SQUID magnetometers' have been developed. SQUID magnetometers are used to characterize materials when the highest detection sensitivity over a broad temperature range and using applied magnetic fields up to several Tesla is needed. Nowadays, this instrument is widely used worldwide in research laboratories. The system is designed to measure the magnetic moment of a sample, from which the magnetization and magnetic susceptibility can be obtained. Therefore, SQUID magnetometers are versatile instruments that perform both, DC and AC magnetic moment measurement.

SQUID magnetometers are classified within the flux methods of measuring magnetization of a sample. Fig.3.6 illustrates schematically its principle: the measurement of the flux change through a pick-up coil system with a SQUID. This signal is proportional to the magnetic moment of a sample, which is magnetized by the magnetic field produced by a superconducting magnet.



### 4.7.1 Basic Components

The main components of a SQUID magnetometer are: (a) superconducting magnet (that must be acquired together its programmable bipolar power supply); (b) superconducting detection coil which is coupled inductively to the sample; (c) a SQUID connected to the detection coil; (d) superconducting magnetic shield. In the following a description of each one is given:

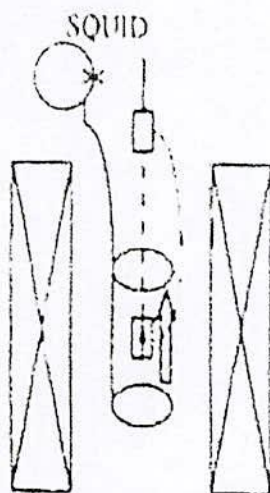


Fig 4.7 . SQUID magnetometer principle.

#### 4.7.1.1 Superconducting Magnet

A superconducting magnet is a solenoid made of superconducting wire. Fig.(4.7) shows a cut away view of a typical superconducting magnet used in a SQUID magnetometer. This solenoid must be kept at liquid helium temperature in a liquid-helium Dewar. The uniform magnetic field is produced along the axial cylindrical bore of the coil. Currently, superconducting solenoids that produce magnetic fields in the range 5-18 Tesla are commercially available. To operate a superconducting magnet requires an appropriate programmable bipolar power supply.



#### **4.7.1.2 Superconducting Detection Coil**

This is a single piece of superconducting wire configured as a second-order gradiometer (Fig. 3.8). This pick-up coil system is placed in the uniform magnetic field region of the solenoidal superconducting magnet.

#### **4.7.1.3 SQUID**

High sensitivity is possible because this device responds to a fraction of the flux quantum. The SQUID device is usually a thin film that functions as a extremely sensitive current-to-voltage-converter. A measurement is done in this equipment by moving the sample through the second-order gradiometer. Hence, the magnetic moment of the sample induces an electric current in the pick-up coil system. A change in the magnetic flux in these coils changes the persistent current in the detection circuit. So, the change in the current in the detection coils produce variation in the SQUID output voltage proportional to the magnetic moment of sample.

#### **4.7.1.4 Superconducting Magnetic Shield**

Superconducting magnetic shield is used to shield the SQUID sensor from the fluctuations of the ambient magnetic field of the place where the magnetometer is located and from the large magnetic field produced by the superconducting magnet.

### **4.7.2 Applications**

Using this kind of equipment one can measure: (a) The real and imaginary components of the AC magnetic susceptibility as a function of frequency, temperature, AC magnetic field amplitude and DC magnetic field value. (b) The DC magnetic moment

as a function of temperature, DC magnet: and time. Using a specially designed sample holder the magnetic moment as a function of angle can be measured.

High sensitivity is needed when samples with low intrinsic magnetic moment or low mass are measured. In thin films, for instance, the mass may be smaller than 1 microgram. These materials are therefore difficult to characterize using a extraction or vibrating sample magnetometer but not with a SQUID.

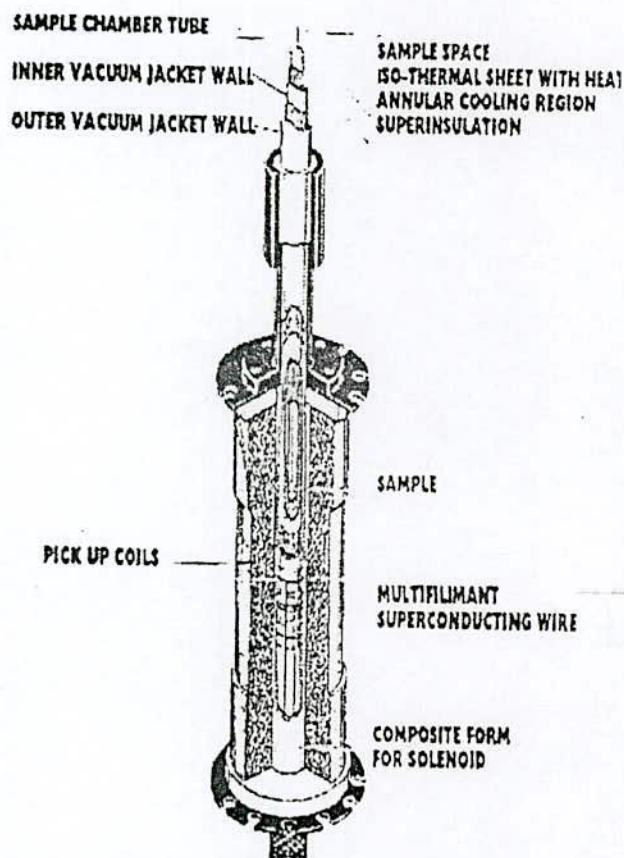


Fig 4.8 Cut view of a typical superconducting pick-up coils.

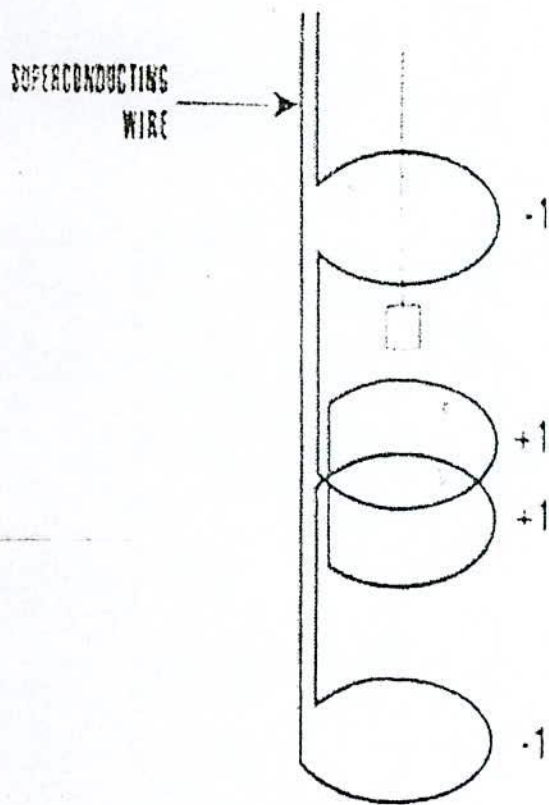


Fig 4.9 . Second-order gradiometer magnet.



### 4.7.3 Improved Sensitivity

The MPMS XL features the new reciprocating sample measurement system. Unlike DC measurements where the sample is moved through the coils in discrete steps the RSO measurements are performed using a servo motor which rapidly oscillates the sample, as shown in Fig. (above). These measurements have a sensitivity of  $5 \times 10^{-9}$  EMU magnetometer. Also for measurements of magnetic viscosity in permanent magnets, where small changes of magnetization as a function of time must be recorded, SQUID magnetometer is the best choice.

A shaft encoder on the servo motor records the position of the sample synchronous with the SQUID signal. The data received is fitted to an ideal dipole moment response. To ensure this assumption is applicable, samples need to be small: the calibration sample is a cylinder of 3 mm diameter and 3 mm height. Samples are of this size or smaller match an ideal point dipole to an accuracy of approximately 0.1%.

RSO measurements can be made in one of two configurations: Center or Maximum slope. Center scans use large oscillations (2 to 3 cm) around the center point of the pickup coils. These scans take a long time but the sample always remains properly located and a large number of measurements are recorded. These give the most accurate readings.

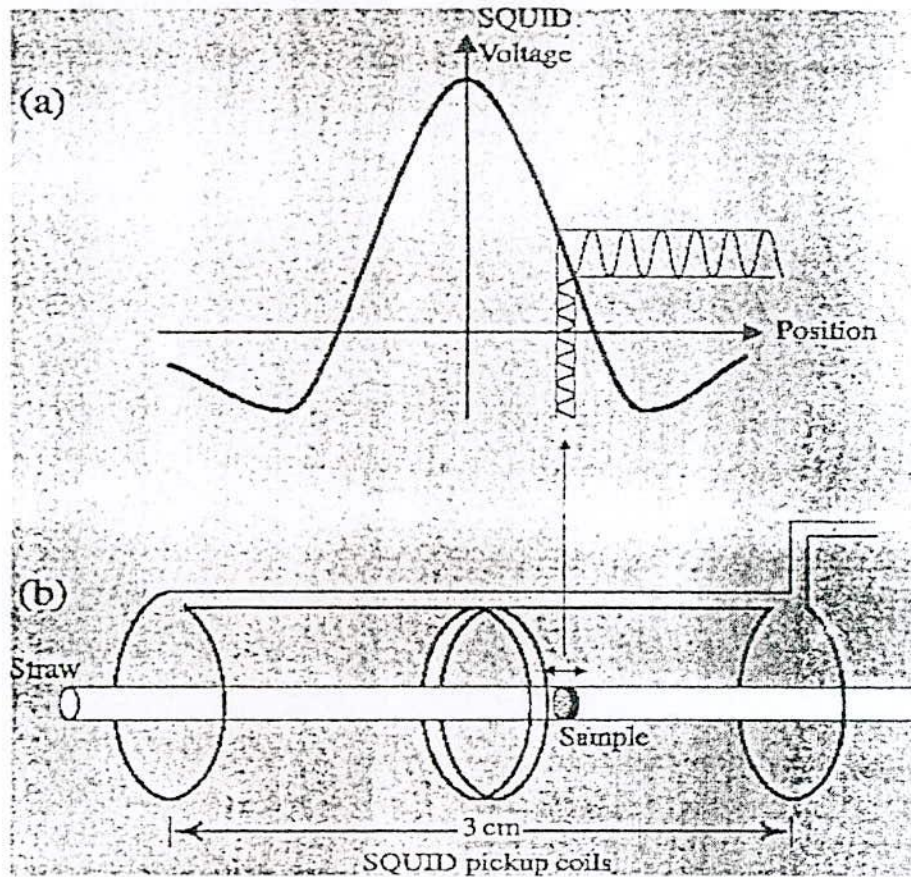
The Maximum Slope method oscillates the sample over a small region (2 mm) at the most linear part of the SQUID response (as shown in the Fig.-4.10). The magnetic field variation, however it also make these prevents the sample being subjected to significant measurement less accurate and susceptible to drift in the sample position.

### 4.7.4 Extended Temperature Capability

The MPMS XL features significant improvements in the temperature control system. Utilizing a new design for the helium flow impedance, the NIPMS XL has the



capability to operate continuously at temperatures below 4.2K for indefinite period of time - completely removing time limitations for making measurement in this temperature regime.



1 Fig 4.10 . Illustration of an RSO measurement with a small amplitude. (a) shows the ideal SQUID response for a dipole and (b) shows the movement of the sample within the SQUID pickup coils.

The new MPMS XL eliminates the operations associated with filling and recycling the He reservoir. Thus, the system solves the traditional problems of temperature instability and hysteresis associated with rapid boil off of liquid helium when warming through 4.2 K. The results are smooth monotonic transitions across 4.2 K during both warming and cooling temperature sweeps. All these capabilities are fully automated for precise systems control and user-friendly operation.

### **4.7.5 Enhanced Thermometry and Temperature Sweep Operation**

In addition to a redesigned impedance system, the MPMS XL uses a new thermometer design for improved temperature accuracy and precise thermal control. The new thermometry, designed and developed at Quantum Design, is installed in close proximity to the sample within the sensitive coil detection region. This improved design is combined with new temperature control capabilities to provide more accurate measurements of the sample chamber, even under extreme temperature changes.

The new Temperature Sweep mode of operation provides MPMS XL users with the ability to take magnetic measurements while sweeping the system temperature at a controlled rate – automatically – with no manual intervention. This mode provides a controlled, monotonic change in temperature during a measurement sequence at rates up to 10 K min. Measurements of temperature dependence over large temperature ranges, which previously required time consuming temperature stabilization, can now be made quickly and precisely using Temperature Sweep Mode.

### **4.7.6 Software Control / Automation**

A new software interface completes the flexibility and usability of the MPMS XL. Running under Microsoft Windows the state-of-the-art MPMS MultiVU software interface provides a level of control for system operation, graphics and data analysis previously unavailable. With MultiVu, simultaneously viewing data files in multiple formats is easily accomplished. Similarly, display of multiple graphs allows for easy comparison of results from different experiments. Operationally, MultiVu is a valuable tool in setting up and editing several measurement protocol files simultaneously.



## 4.8 Magnetization Measurement

Magnetization is defined as the magnetic moment per unit volume or mass of the substance. There are various ways of measuring magnetization of a substance. In the present thesis magnetization has been measured by using a Vibrating Sample Magnetometer (VSM) at room temperature, applying a wide range of magnetic field from  $-800,000 \text{ Am}^{-1}$  to  $+800,000 \text{ Am}^{-1}$ .

These measurements were carried out at Atomic Energy Research Institute, Savar. We use Hirst VSM 02 which is an automatic Vibrating Sample Magnetometer for characterization of soft and hard magnetic materials manufactured by HIRST Magnetic Instruments Ltd. A block diagram of a typical VSM system is shown in Fig. 4.11 The Hirst VSM system arrangement is shown in the Fig 4.12. The vibration and measuring unit of Hirst VSM is shown in Fig. 4.13

### 4.8.1 Principle of Vibrating Sample Magnetometer

Vibrating Sample Magnetometer developed by S. Foner<sup>(4.4-4.5)</sup> is a versatile and sensitive method of measuring magnetic properties and is based on the flux change in a coil when the sample is vibrated near it. The VSM is an instrument designed to continuously measure the magnetic properties of materials as a function of temperature and field. In this type of magnetometer, the sample is vibrated up and down in a region surrounded by several pickup coils. The magnetic sample is thus acting as a time-changing magnetic flux, varying inside a particular region of fixed area. From Maxwell's Law it is known that a time varying magnetic flux is accompanied by an electric field and the field induces a voltage in pickup coils. This alternating voltage signal is processed by a control unit system, in order to increase the signal to noise ratio. The result is a measure of the magnetization of the sample.



#### 4.8.2 Description and brief Working Principle of Hirst VSM02

Vibrating Sample Magnetometers, as the name implies, Vibrate the sample as part of the measurement process. This provides the Flux meter element of the system with the dynamic component which it requires to make the measurement. The applied field is changed so, at each measurement point the field is static and hence no eddy currents to cause problems.

The object is using a VSM or any other type of magnetic characterization of magnetization ( $J$ ) on the applied field  $H > J (H)$ . Once this is obtained, many useful parameters can be extracted from the data. VSM typically generate the applied field ( $H$ ) using an electromagnet or a super conducting solenoid for fields greater than 2.5-3 Tesla. The magnetic driven around its hysteresis curve by changing the applied field ( $H$ ) and the  $J$  signal is determined.

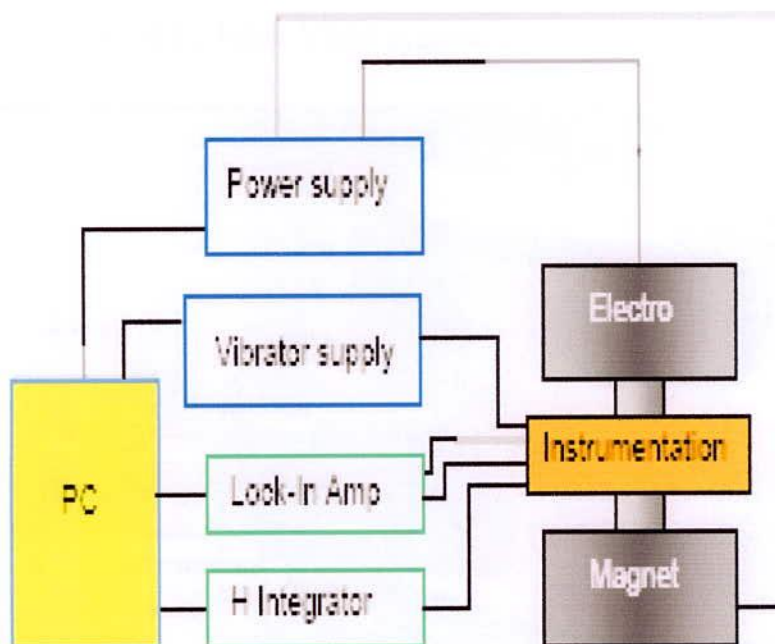


Fig. 4.11 Block diagram of a VSM system

In the VSM02 a conventional electromagnet is implemented with two independent coils driven by independent 1000W amplifiers. The current control on the coils utilizes Tran's conductance to ensure that constant current is supplied for a particular demand and to ensure that resistive changes due to heating do not cause the measurement to drift. The applied field (H) is measured using a hall element connected to a Guan meter (BGMOI).

The magnetization field (J) is determined by utilizing pick up coils. As with large iron poles and light inductances it is impossible to change the field quickly without causing unwanted effects. VSM measurements are a quasi-static process where the sample J field is determined when the applied field is static. As the applied field is static when J is determined, the J magnetization field is also static. Pick up coil work by Faradays Law of induction. Where  $e$  is the voltage induced,  $d\theta$  is the change in magnetic flux in time  $t$ . As the J field is static there is no  $d\theta$  so a pick up coil cannot work. To overcome this problem the sample is vibrated using a sinusoidal oscillation. This vibration generates the required change in flux with respect to time and produces a signal from the pickup coils.

As the sample is vibrating at a known frequency with known phase it is possible to use a lock in amplifier to extract the J value from the pick up coils output. This is also has huge advantages as lock-in amplifiers can discriminate against noise and pick out a tiny signal buried in noise. This gives VSM's the potential to have huge gain on the J measurement channel. In the VSM 02 the maximum J gain is approximately X 1,300,000. This allows very small samples, or samples with a small magnetic moment to be measured such as thin-films powders and inks.

### **4.8.3 Working Principle of Vibrating Sample Magnetometer**

If a sample of any material is placed in a uniform magnetic field, created between the poles of an electromagnet, a dipole moment will be induced. If the sample vibrates with sinusoidal motion a sinusoidal electrical signal can be induced in suitably placed pick-up coils. The signal has the



same frequency of vibration and its amplitude will be proportional to the magnetic moment, amplitude, and relative position with respect to the pick-up coils system. Figure 3.10 shows the block diagram of vibrating sample magnetometer.

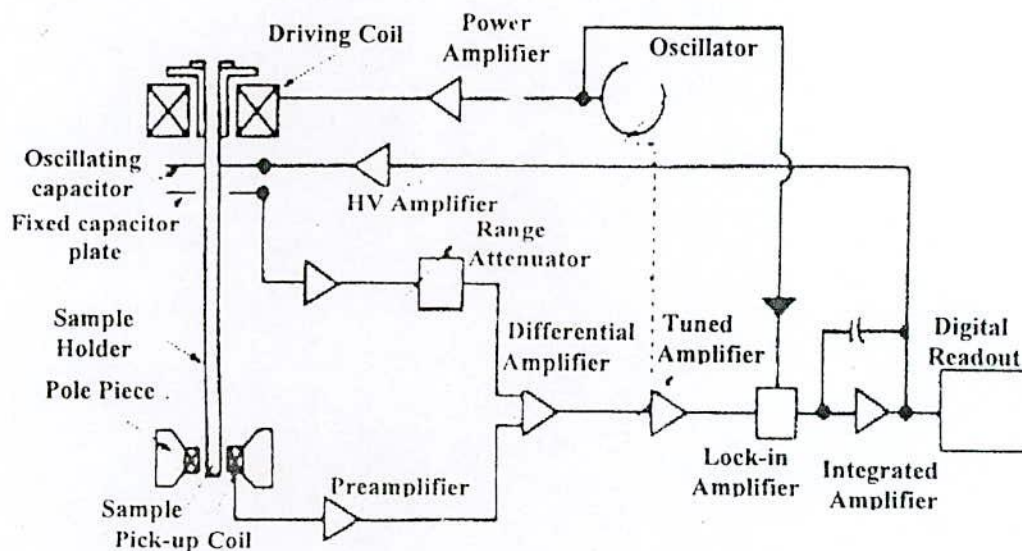


Fig. 4.14: Block diagram of vibrating sample magnetometer

The sample is fixed to a small sample holder located at the end of a sample rod mounted in an electromechanical transducer. The transducer is driven by a power amplifier which itself is driven by an oscillator at a frequency of 90 Hertz. So, the sample vibrates along the Z axis perpendicular to the magnetizing field. The latter induced a signal in the pick-up coil system that is fed to a differential amplifier. The output of the differential amplifier is subsequently fed into a tuned amplifier and an internal lock-in amplifier that receives a reference signal supplied by the oscillator



The output of this lock-in amplifier, or the output of the magnetometer itself, is a DC signal proportional to the magnetic moment of the sample being studied. The electromechanical transducer can move along X, Y and Z directions in order to find the saddle point. Calibration of the vibrating sample magnetometer is done by measuring the signal of a pure Ni standard of known saturation magnetic moment placed in the saddle point.

The basic instrument includes the electromechanical system and the electronic system (including a personal computer). Laboratory electromagnets or superconducting coils of various maximum field strengths may be used. For ultra-high magnetic fields a cryogen-free magnets can be also used. For the characterization of soft magnetic materials a pair of Helmholtz coils may be also used. As accessories a high temperature oven assembly and a liquid Helium cryostat is also used.

Technical specifications of VSM (typical figures)

Maximum sensitivity:  $5 \times 10^{-5}$  emu

Calibrated ranges from 100 to 0.01 emu full scale.

Stability of output signal: 0.05% of full scale per day.

Absolute accuracy: better than 2%

Angular variation of H: full  $360^\circ$  rotation  $\sim 0.5^\circ$

Maximum sample size: 7mm.

#### 4.9 Applications

Using a vibrating sample magnetometer one can measure the DC magnetic moment as a function of temperature, magnetic field, angle and

time. So, it allows to perform susceptibility and magnetization studies. Some of the most common measurements done are: hysteresis loops, susceptibility or saturation magnetization as a function of temperature (thermo-magnetic analysis), magnetization curves as a function of angle (anisotropy), and magnetization as a function of time.

**CHAPTER- 5:  
RESULTS AND DISCUSSION**



## 5.0 Results and Discussion

### 5.1 X-ray Diffraction (XRD) Analysis

For the study of diffraction are useful techniques to identify the various phases of the annealed nanocomposite magnetic materials crystallographic structural properties. X-ray diffraction (XRD), neutron diffraction and electron diffraction are useful techniques to identify the various phases of the time dependent annealed nanocomposite magnetic materials of the composition  $\text{Nd}_3\text{Tb}_1\text{Fe}_{76}\text{Cu}_{0.5}\text{Nb}_1\text{B}_{18.5}$  and  $\text{Nd}_4\text{Fe}_{76}\text{Cu}_{0.5}\text{Nb}_1\text{B}_{18.5}$ . X-ray diffraction studies of the samples were performed by using Philips X'PERT PRO X-ray Diffractometer using  $\text{Cu-K}_\alpha$  radiation in the range of  $2\theta = 30^\circ$  to  $80^\circ$  in steps of  $0.02^\circ$ . XRD patterns of the annealed samples (annealing temperature 923 K) are different annealing time 1, 3, 5, 10 & 20 minute for  $\text{Nd}_3\text{Tb}_1\text{Fe}_{76}\text{Cu}_{0.5}\text{Nb}_1\text{B}_{18.5}$  and  $\text{Nd}_4\text{Fe}_{76}\text{Cu}_{0.5}\text{Nb}_1\text{B}_{18.5}$  are presented.

#### 5.1.1 Time Annealing Effect of Structural Properties of $\text{Nd}_3\text{Tb}_1\text{Fe}_{76}\text{Cu}_{0.5}\text{Nb}_1\text{B}_{18.5}$

In order to determine crystallization products of  $\text{Nd}_3\text{Tb}_1\text{Fe}_{76}\text{Cu}_{0.5}\text{Nb}_1\text{B}_{18.5}$  at different stages of crystallization X-ray diffraction studies have been performed. The phases have been identified as  $\text{Fe}_3\text{B}$  and  $(\text{NdTb})_2\text{Fe}_{14}\text{B}$  by X-ray diffraction<sup>(5.1)</sup>. X-ray diffraction patterns for the samples annealed at 923 K for different annealing time are shown in Fig.-5.1 to Fig.-5.5. For the annealing time of 1 min soft phase  $\text{Fe}_3\text{B}$  has formed.

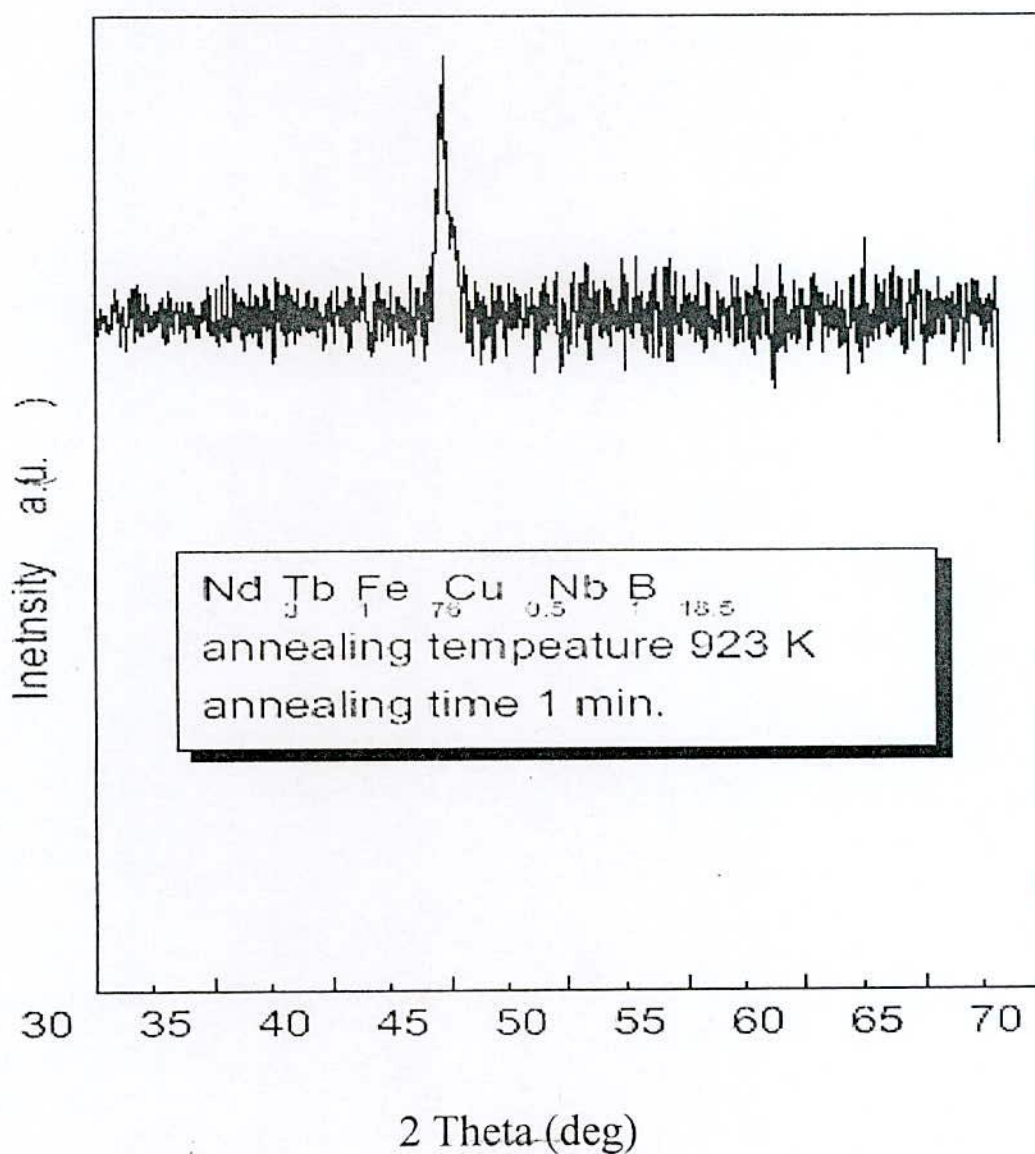


Fig. -5.1 X-ray diffraction patterns for the samples annealed at 923 K for the annealing time of 1 minute

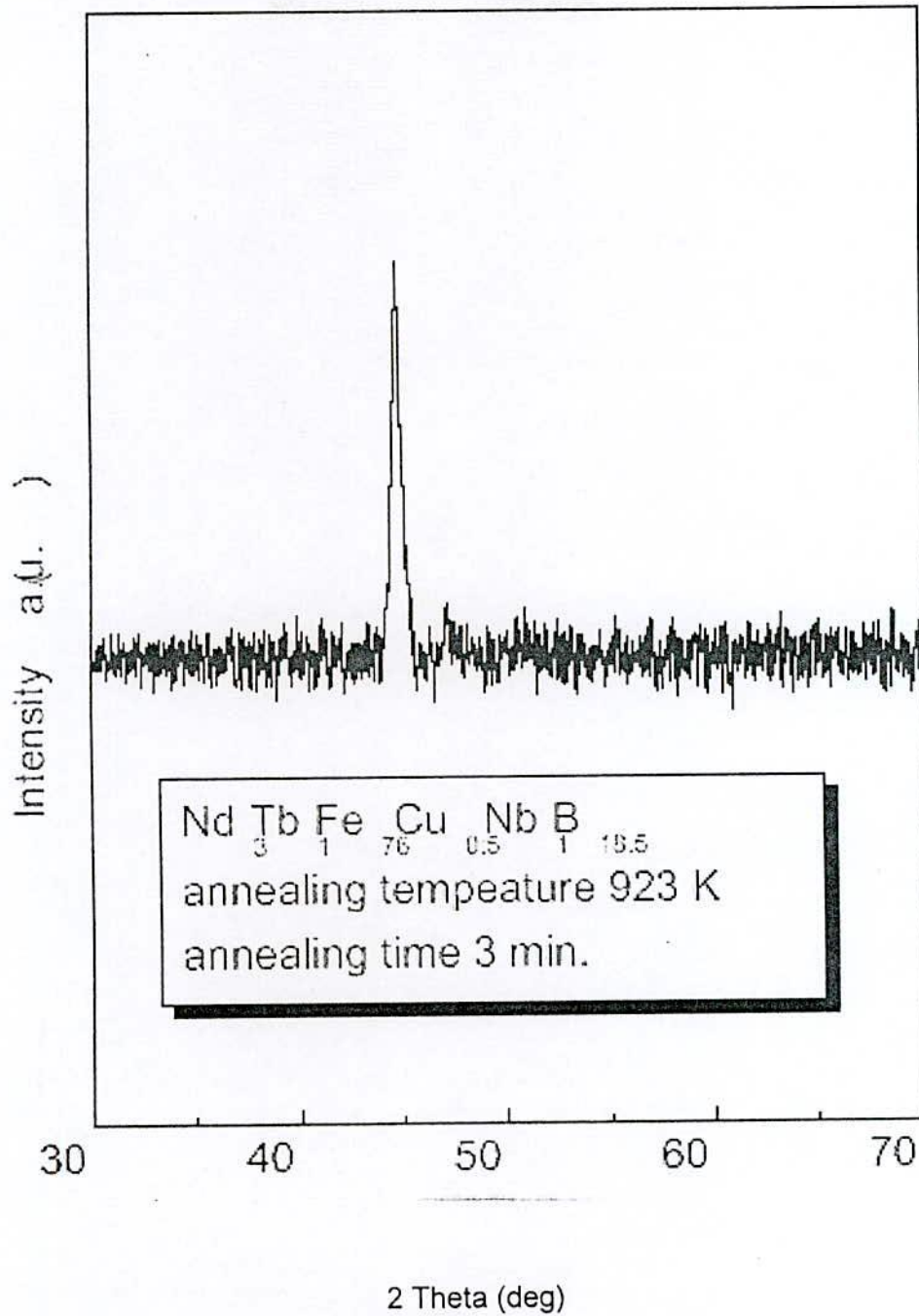
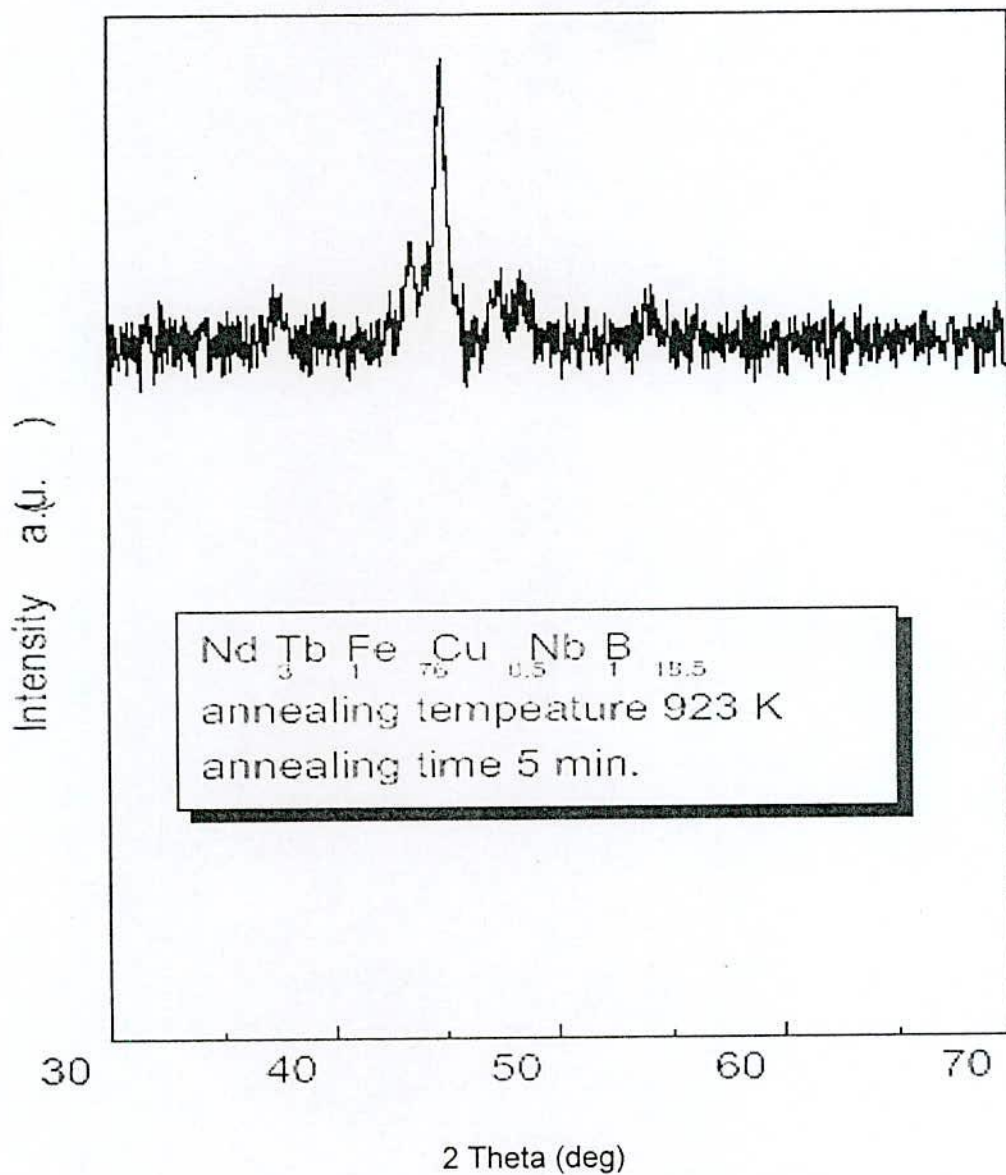


Fig.- 5.2 X-ray diffraction patterns for the samples annealed at 923 K for the annealing time of 3 minute





**Fig. - 5.3** X-ray diffraction patterns for the samples annealed at 923 K for the annealing time of 5 min.



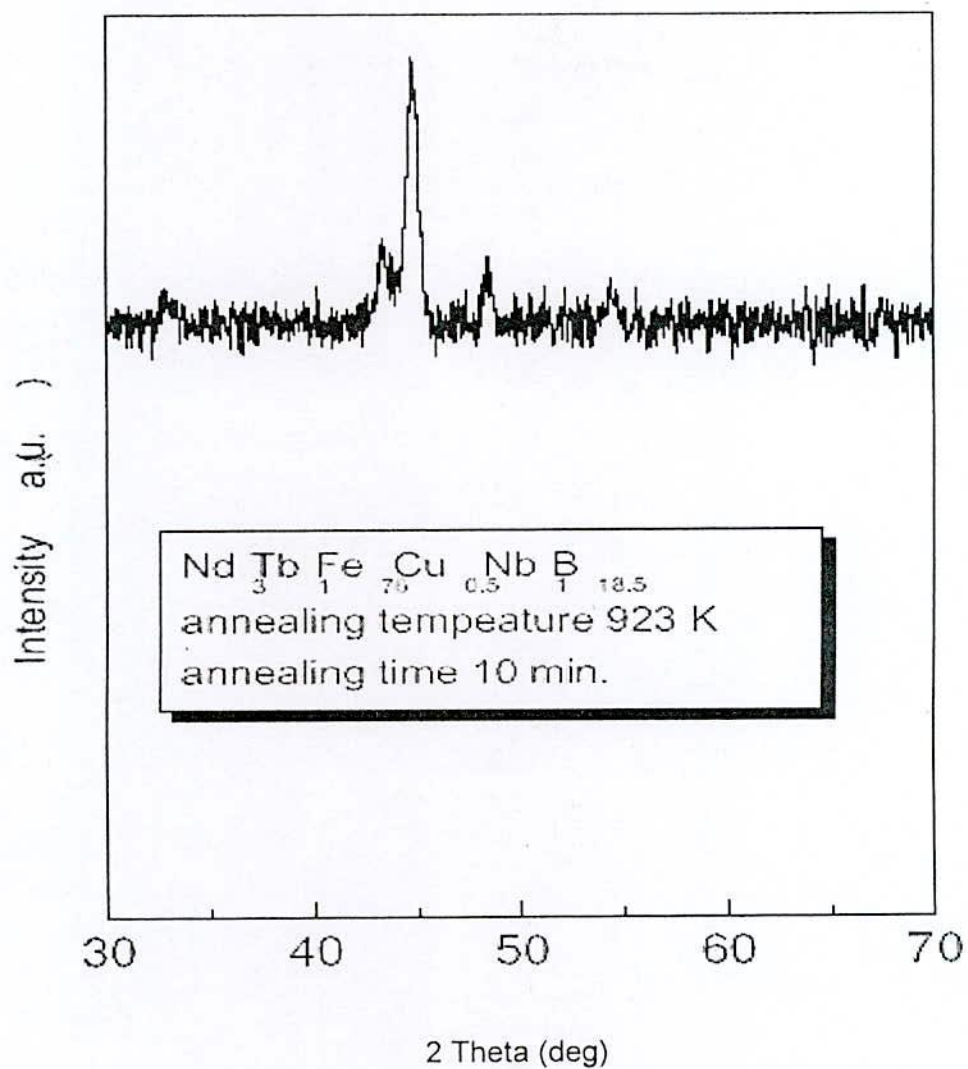


Fig. – 5.4 X-ray diffraction patterns for the samples annealed at 923 K for the annealing time of 10 minute

For the higher annealing time, hard magnetic phase  $\text{Nd}_2\text{Fe}_{14}\text{B}$  has formed though in a small amount in association with soft phase  $\text{Fe}_3\text{B}$ . It has been observed by Kneller and Hawig<sup>(1.1)</sup> that formation of only 10% of  $\text{Nd}_2\text{Fe}_{14}\text{B}$  is sufficient to enhance the coercivity significantly by exchange spring mechanism and therefore relative amount of hard phase is always very small than the soft phase in the initial stage of annealing. Relative amount of hard phase increases with the increase of annealing time and for the annealing time of 20 minutes the peaks of  $\text{Nd}_2\text{Fe}_{14}\text{B}$  phase are prominent. With the increase of annealing time relative amount of soft phase  $\text{Fe}_3\text{B}$  also increases. Grain size does not change significantly and remains on the average 16 to 18 nm as determined from FWHM of highest intensity peak. In order to observe the effect of Tb addition the X-ray diffraction patterns of the sample of composition  $\text{Nd}_4\text{Fe}_{76}\text{Cu}_{0.5}\text{Nb}_1\text{B}_{18.5}$  has been presented in Fig.- 5.6 to Fig.- 5.9. Though the difference in composition between these alloys is the substitution of 1 at.% of Tb in place of Nd the X-ray diffraction patterns are very much identical. This is because the coherent crystal structure of  $(\text{NdTb})_2\text{Fe}_{14}\text{B}/\text{Fe}_3\text{B}$  for the first composition and  $\text{Nd}_2\text{Fe}_{14}\text{B}/\text{Fe}_3\text{B}$  are very similar. For the later composition also first phase, which has been evolved is  $\text{Fe}_3\text{B}$  phase. With the increase of annealing time the hard phase  $\text{Nd}_2\text{Fe}_{14}\text{B}$  has evolved. All these compositions have exhibited qualitative increment of both soft and hard magnetic properties due to the evolution of nanoscaled grains evolved from amorphous precursor by appropriate annealing. Formation of the hard phase has been manifested in large coercivity for both the sample, which will be described in the following next section.



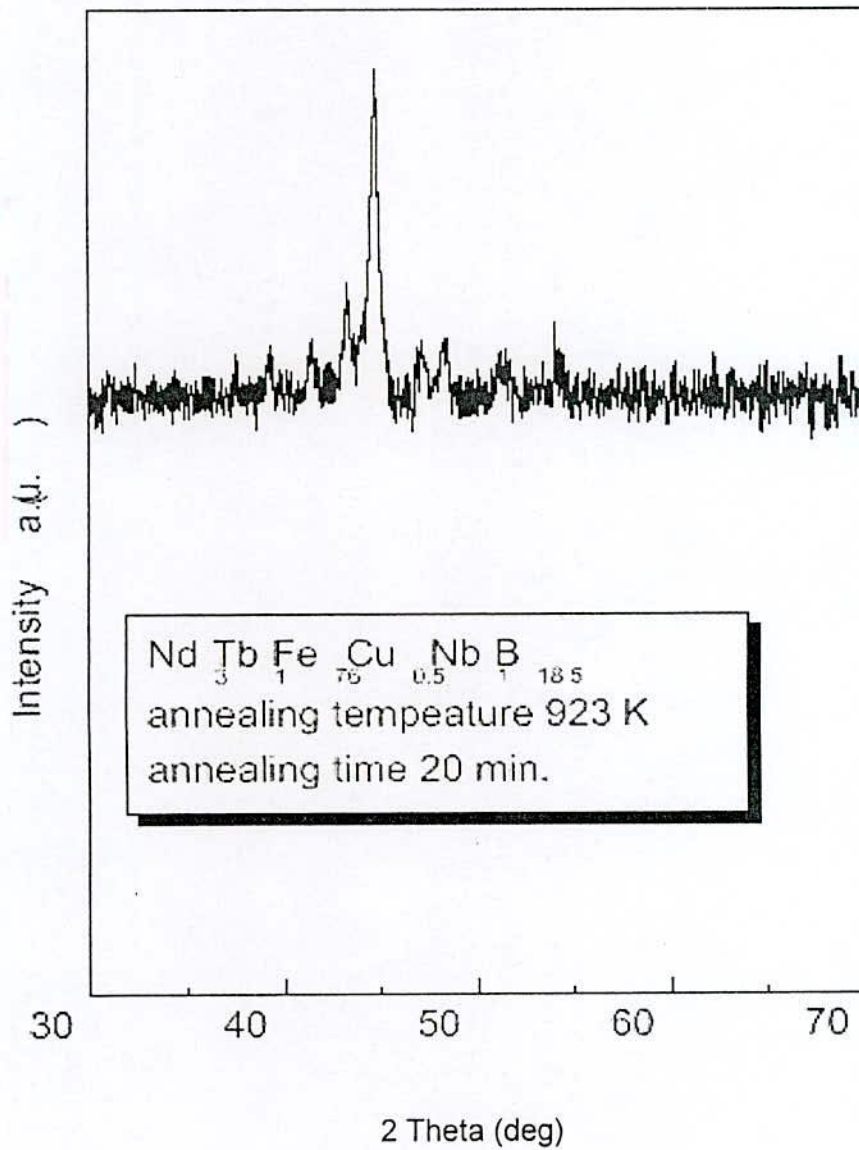


Fig. - 5. 5 X-ray diffraction patterns for the samples annealed at 923 K for the annealing time of 20 minute

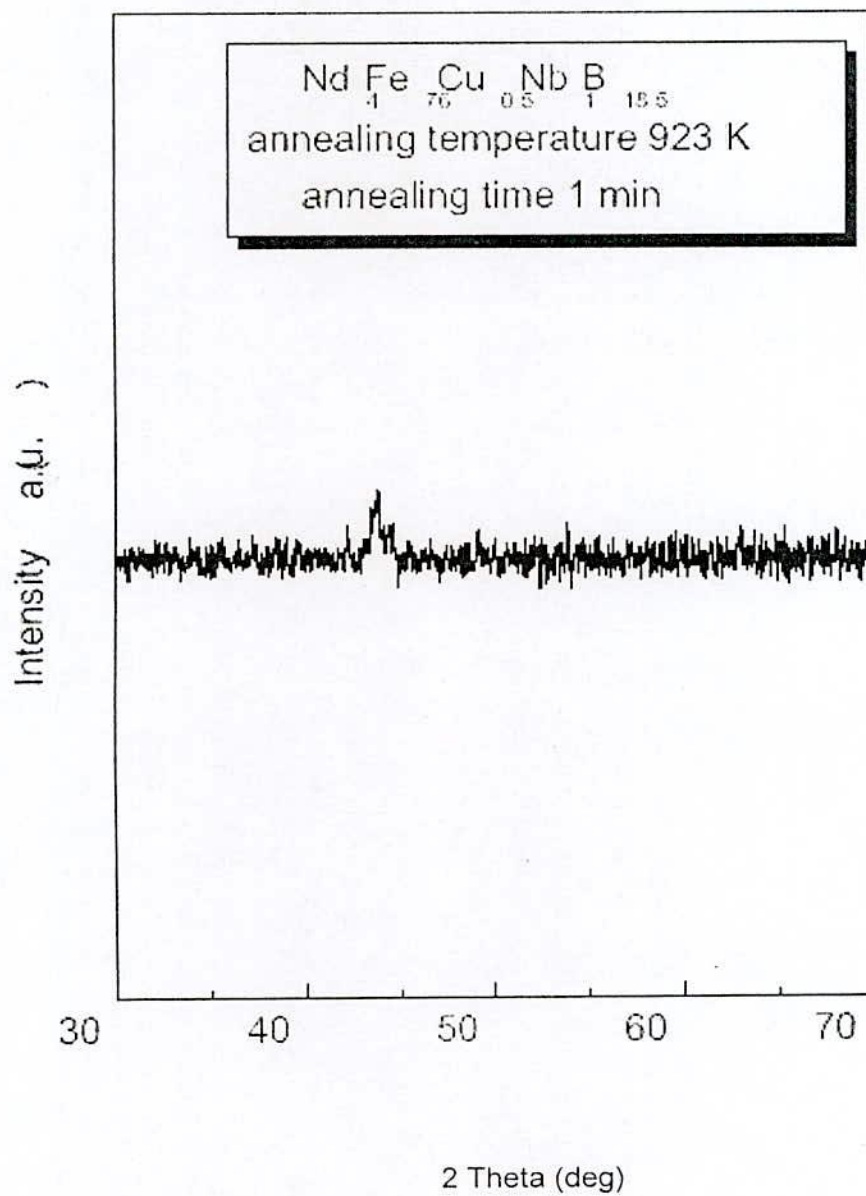


Fig.- 5.6 X-ray diffraction patterns for the samples annealed at 923 K for the annealing time of 1 minute

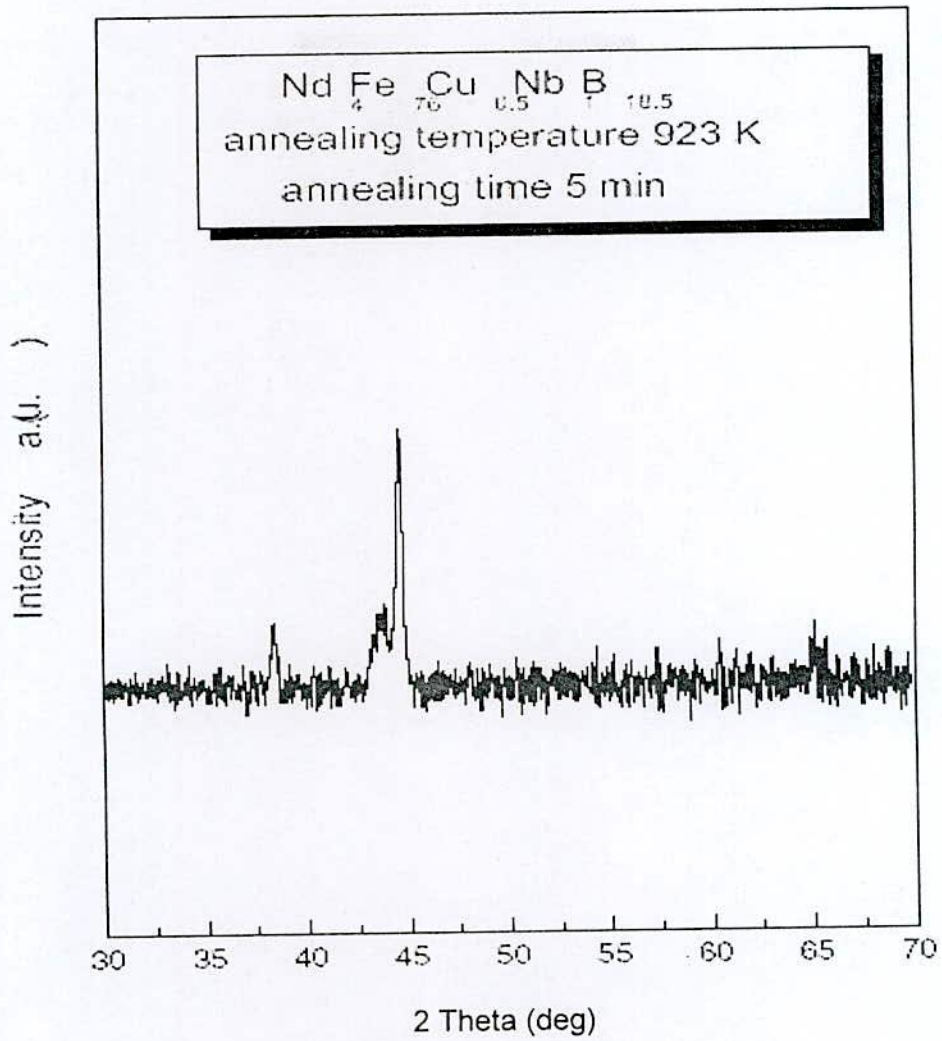


Fig. - 5.7 X-ray diffraction patterns for the samples annealed at 923 K for the annealing time of 5 minute



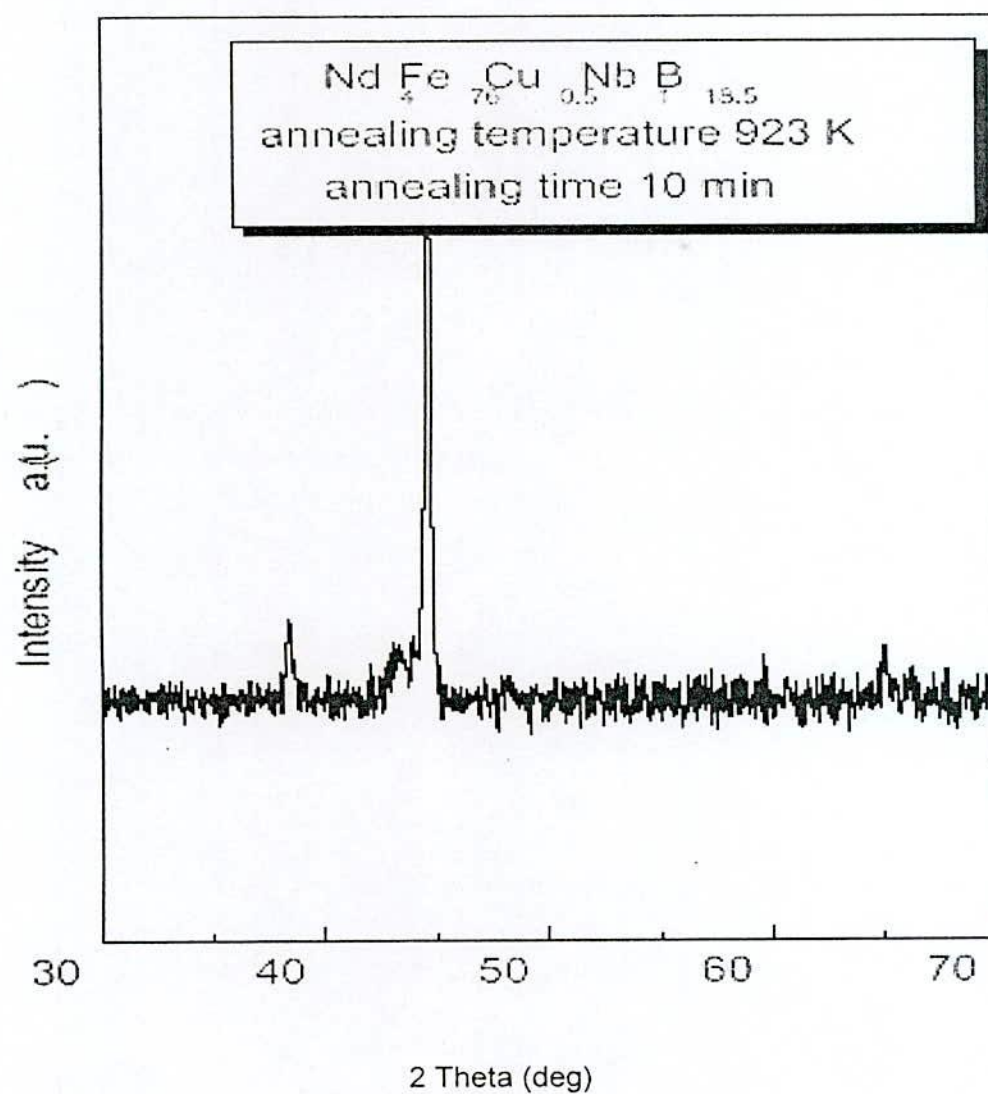


Fig. -5.8 X-ray diffraction patterns for the samples annealed at 923 K for the annealing time of 10 minute

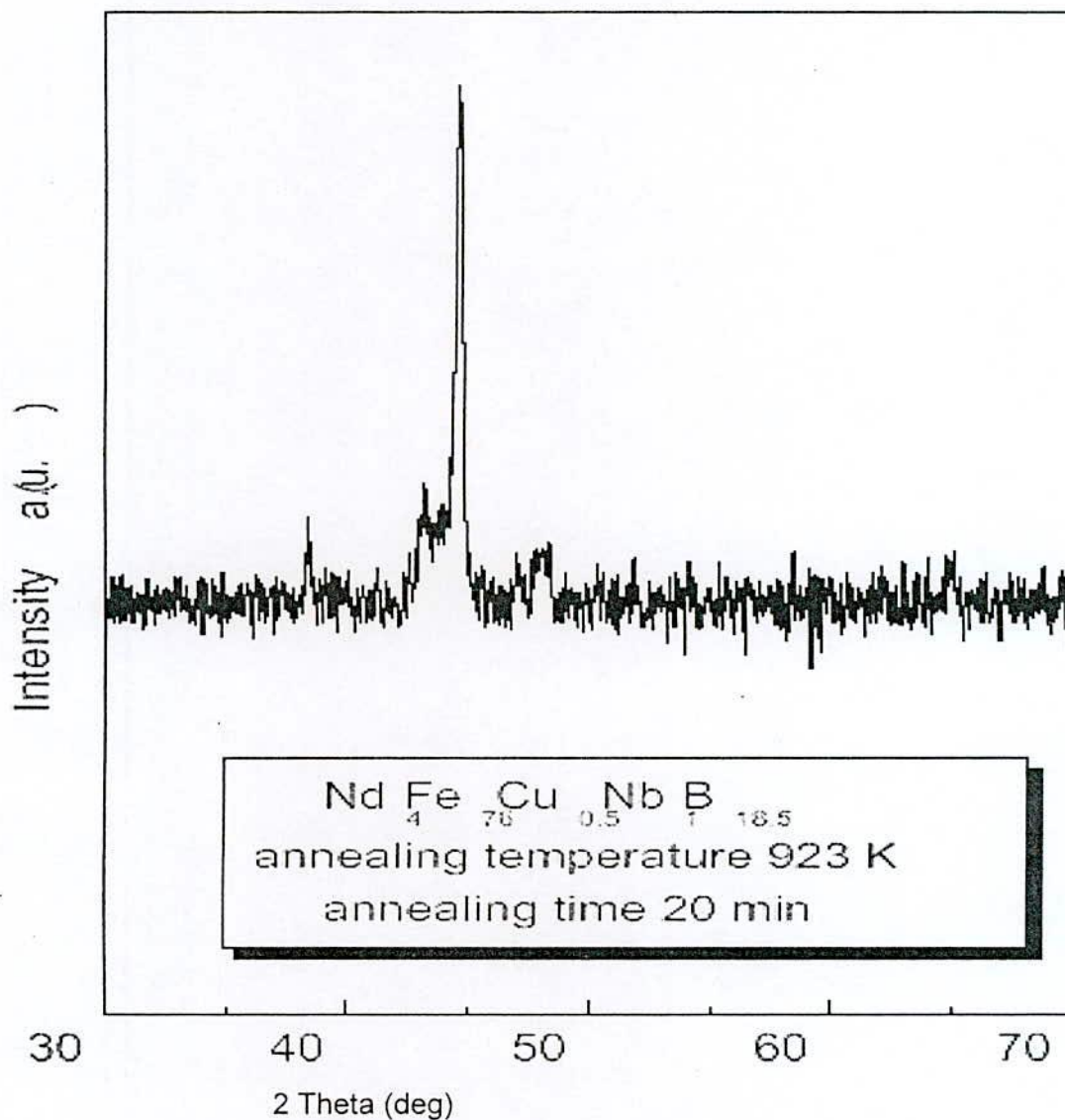
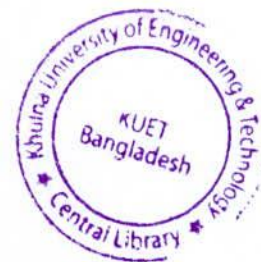


Fig.- 5. 9 X-ray diffraction patterns for the samples annealed at 923 K for the annealing time of 20 minute

### 5.1.2 Effect of Different Annealing Time of Hysteresis Parameter of $\text{Nd}_3\text{Tb}_1\text{Fe}_{76}\text{Cu}_{0.5}\text{Nb}_1\text{B}_{18.5}$ at Constant Annealing Temperature

Hysteresis loops obtained at 923 K for different annealing time have been presented in Fig.- 5.10. In Fig.-5.10, Y-axis values have been normalized by the maximum value of saturation magnetization. It may be noticed that saturation magnetization has not been achieved even after applying a maximum field of 3 Tesla. This is due to the high magneto-crystalline anisotropy, which is common for  $\text{R}_2\text{Fe}_{14}\text{B}$ . Values of saturation magnetization, coercivity, remanent ratio, and maximum energy product derived from the hysteresis loops have been presented in Table 5.1. When the sample is annealed at 923 K for 1 minute the sample is magnetically very soft and field dependence of magnetization gives line hysteresis. Highest value of coercivity about 4.76 kOe, remanent ratio about 0.699 and maximum energy product about 9.54 MGOe has been obtained for the sample annealed at 923 K for 5 minutes. In Fig.- 5. 10, there is no change in the shape of the hysteresis loops, which are convex like single phase permanent magnet up to the annealing time of 20 minutes, which indicates that the material is exchange-coupled up to the annealing time adopted in this experiment.

Hysteresis loops of  $\text{Nd}_4\text{Fe}_{76}\text{Cu}_{0.5}\text{Nb}_1\text{B}_{18.5}$  have been presented in Fig. -5.11. Similar pattern of behavior has been obtained for this composition also. But, since this alloy composition does not contain any Tb, which has very high anisotropic behavior, the values of coercivity are much less. It is notable to observe high remanent ratio for this composition than the former one.



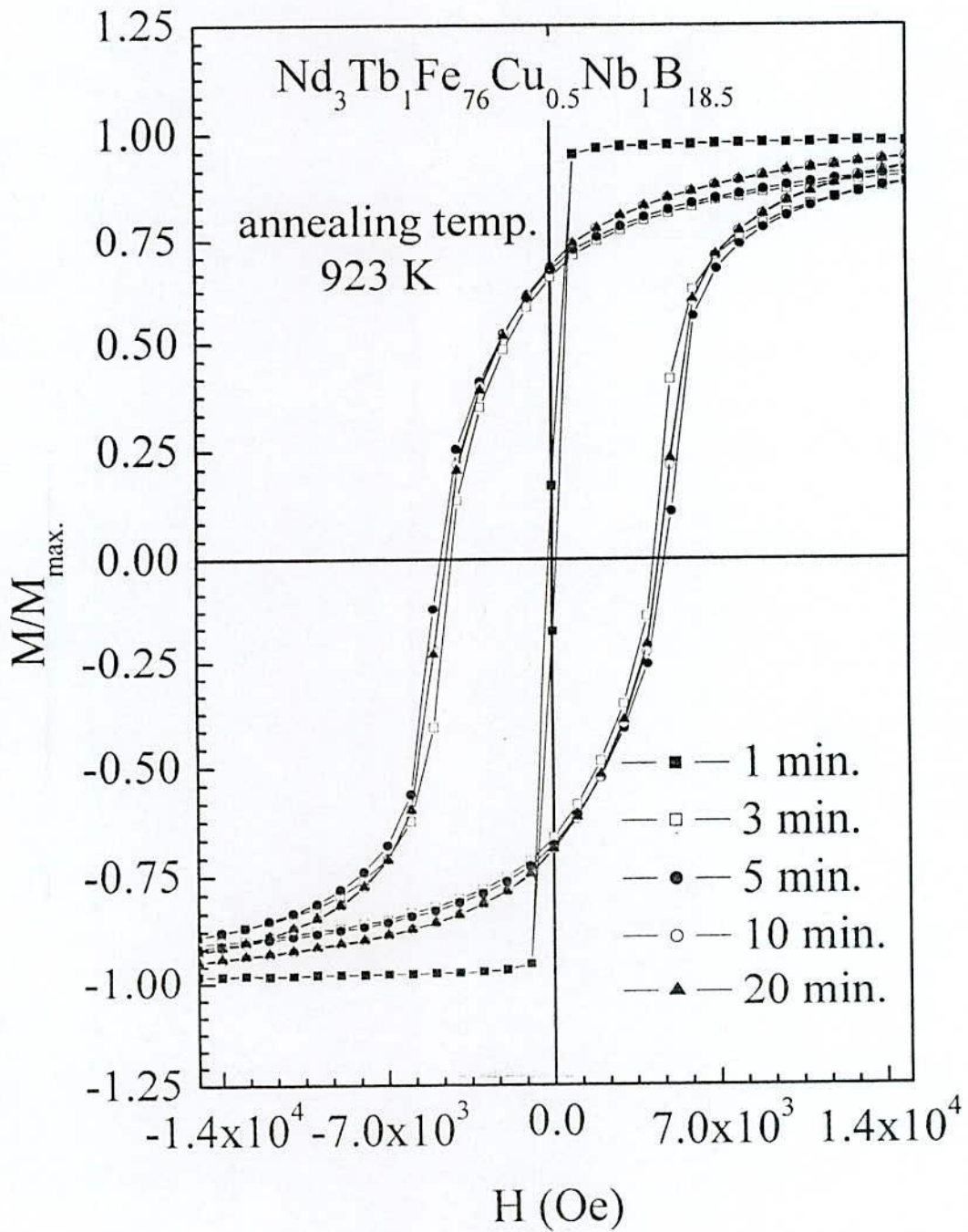


Fig. - 5.10 Hysteresis loops for the samples annealed at 923 K for different annealing time

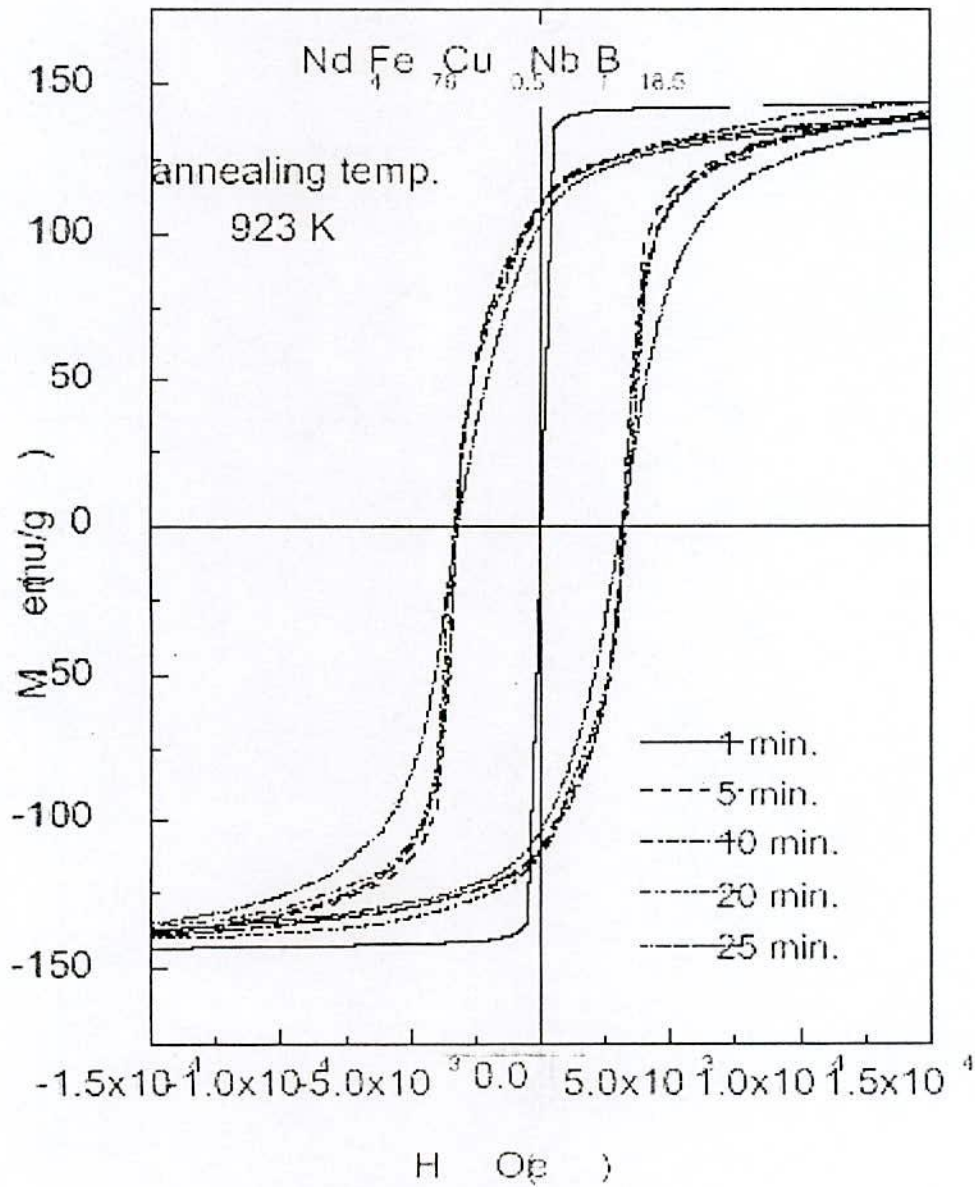


Fig.- 5.11 Hysteresis loops for the samples annealed at 923 K for different annealing time.

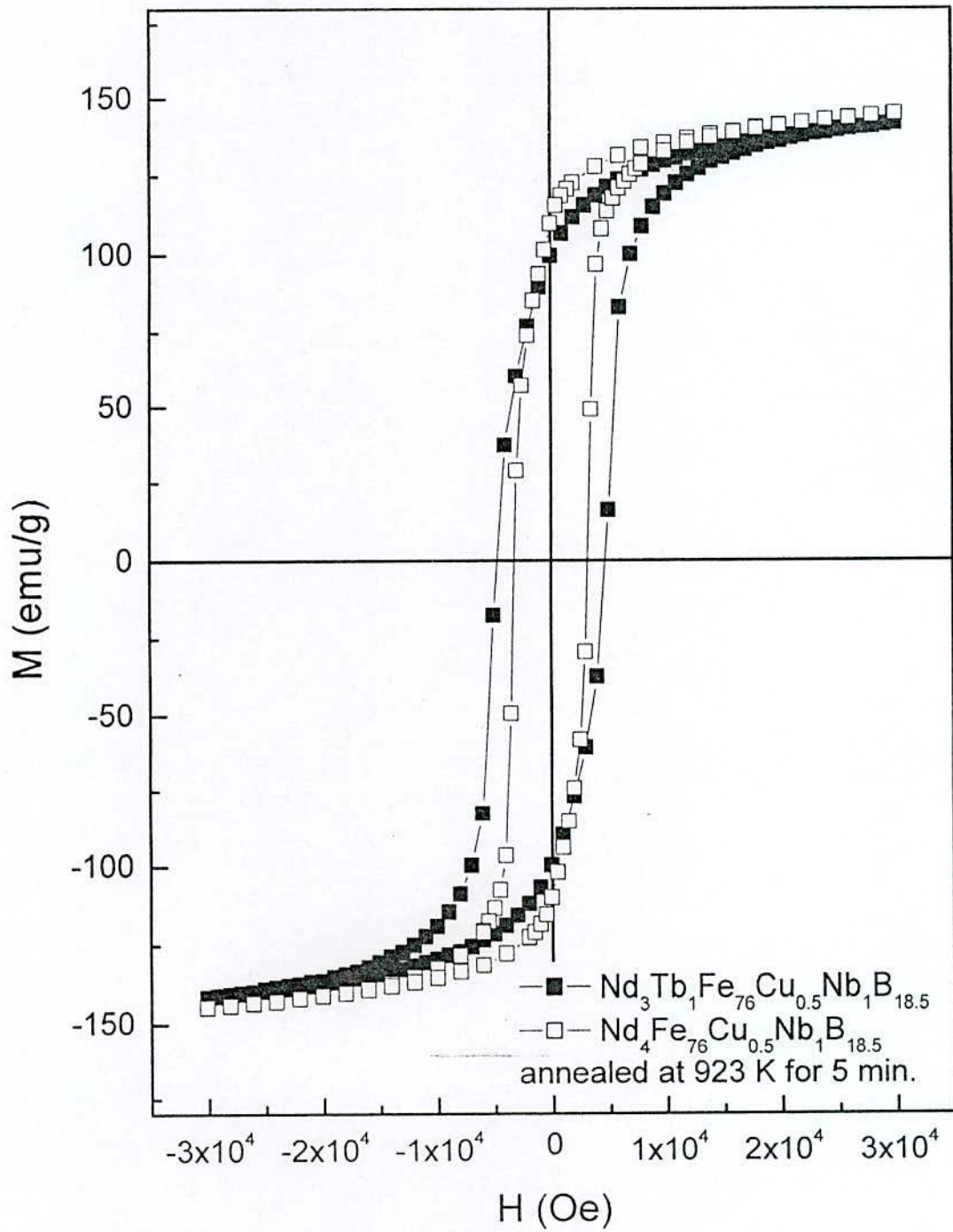


Fig.- 5.12 Comparison of hysteresis loops for the samples annealed at 923 K for annealing time of 5 minute



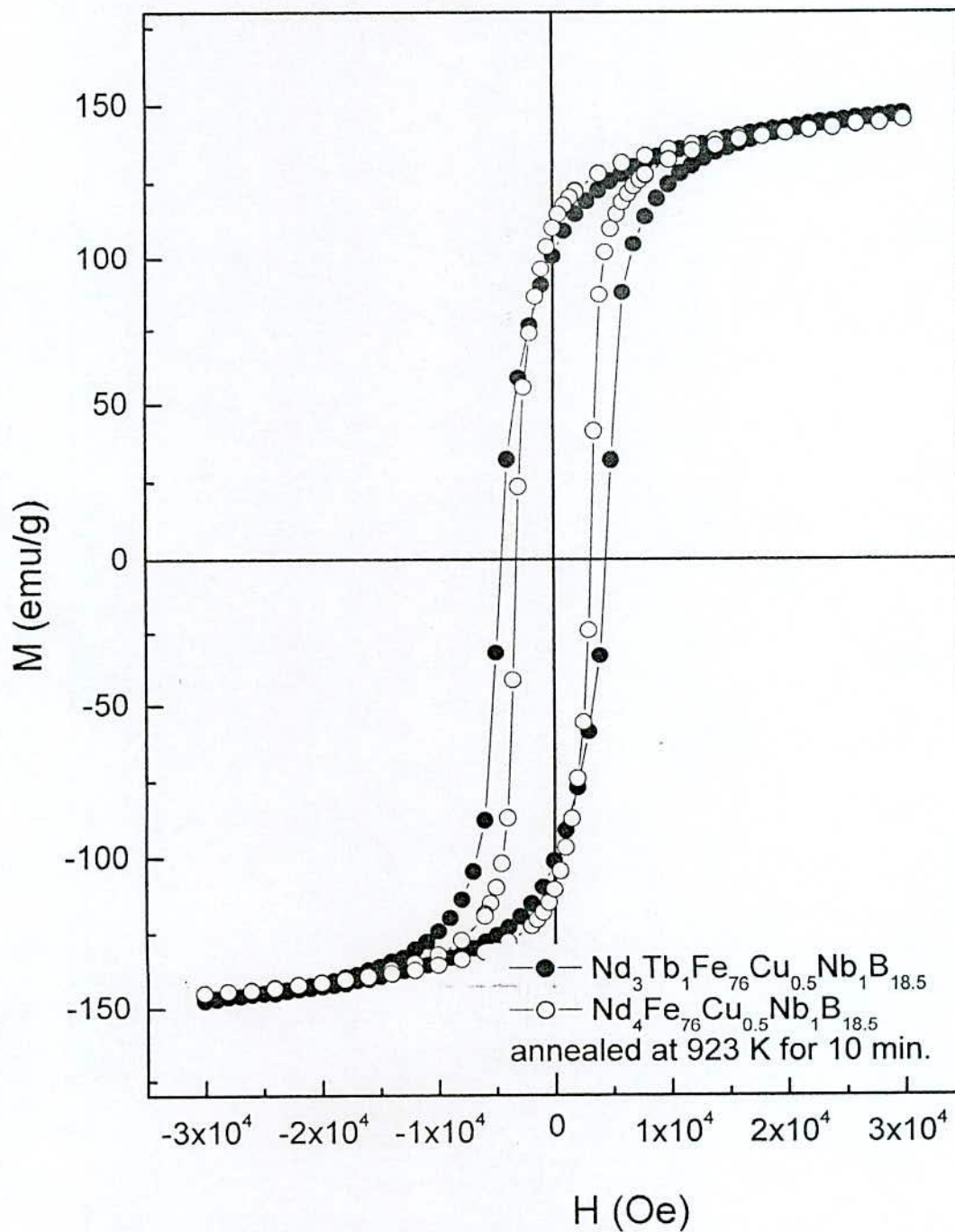


Fig. - 5.13 Comparison of hysteresis loops for the samples annealed at 923 K for annealing time of 10 minute

**Table;- 5.1** Hysteresis loop parameters for  $\text{Nd}_3\text{Tb}_1\text{Fe}_{76}\text{Cu}_{0.5}\text{Nb}_1\text{B}_{18.5}$  and  $\text{Nd}_4\text{Fe}_{76}\text{Cu}_{0.5}\text{Nb}_1\text{B}_{18.5}$

Hysteresis parameters for $\text{Nd}_3\text{Tb}_1\text{Fe}_{76}\text{Cu}_{0.5}\text{Nb}_1\text{B}_{18.5}$					
Anneal. temp. K	Anneal. Time min.	$M_s$ emu / g	$H_c$ kOe	$M_r/M_s$	$(BH)_{\max}$ MGOe
923	1	145	-	-	-
923	3	140	4.15	0.697	8.54
923	5	142	4.76	0.699	9.54
923	10	147	4.40	0.693	9.43
923	20	147	4.52	0.689	9.34

Hysteresis parameters for  $\text{Nd}_4\text{Fe}_{76}\text{Cu}_{0.5}\text{Nb}_1\text{B}_{18.5}$

Anneal. temp. K	Annealing time Min.	$M_s$ emu / g	$H_c$ kOe	$M_r/M_s$	$(BH)_{\max}$ MGOe
923	1				
923	5	145	3.18	0.760	8.99
923	10	145	3.18	0.753	9.21
923	20	145	3.30	0.753	8.37
923	25	144	3.18	0.730	6.92

Due to the combined effect of the high coercivity and low remanent ratio for the former composition and the low coercivity and high remanent ratio of the later composition lead to almost same order of magnitude of energy product,  $(BH)_{max}$ , which can be observed in Fig.-5.12 and Fig.- 5.13 and also in Table 5.1. It is known that the anisotropy field of Tb and Dy is the highest among all the rare earth elements. Therefore, presence of these two elements increase the overall anisotropy of the material as a result of which it leads to enhanced value of coercivity but at the expense of remanent ratio. From Fig.- 5.11, it can be further noticed the effect of over annealing condition for the sample annealed at 923 K for 25 minutes. The curve has assumed slightly concave shape which is a manifestation that the grains have been grown sufficiently large due to over annealing of the sample as a result of which it has been deviated from the convex nature of the hysteresis loop free from constriction effect.

In Fig.-5.12 and Fig.-5.13 hysteresis loops of samples of compositions  $Nd_3Tb_1Fe_{76}Cu_{0.5}Nb_1B_{18.5}$  and  $Nd_4Fe_{76}Cu_{0.5}Nb_1B_{18.5}$  have been presented. It is seen from Table-5.1 that the highest value of  $(BH)_{max}$  of  $Nd_3Tb_1Fe_{76}Cu_{0.5}Nb_1B_{18.5}$  has been obtained for the sample annealed at 923K for 10 minutes. In Fig.-5.12 and Fig.-5.13 the sample without Tb of composition  $Nd_4Fe_{76}Cu_{0.5}Nb_1B_{18.5}$  annealed at the same temperature i.e. 923K for 10 minutes have been presented for comparison. Coercivity, remanent ratio and maximum energy product of  $Nd_4Fe_{76}Cu_{0.5}Nb_1B_{18.5}$  are 3.30 kOe, 0.753 and 8.37 MGOe respectively. While the coercivity, remanent ratio and maximum energy product of  $Nd_3Tb_1Fe_{76}Cu_{0.5}Nb_1B_{18.5}$  are 4.40kOe, 0.693 and 9.43MGOe.



Through an enhancement of coercivity takes place due to the higher anisotropy field when Nd is partially substituted by Tb, remanent ratio is decreased due to antiferromagnetic coupling between rare earth and transition metal<sup>(5.2)</sup>. The magnetization of light rare earth (LRE) sublattice couples ferromagnetically to the magnetization of the transition metal sublattice. The opposite is true for the heavy rare earth (HRE) elements rendering these latter materials ferromagnetic. It may be pointed out here that the anisotropy field of Nd<sub>2</sub>Fe<sub>14</sub>B is 150 kOe (12 MA/m) and Tb<sub>2</sub>Fe<sub>14</sub>B (28 MA/m)<sup>(5.2)</sup>. combined effect of antiferromagnetic coupling between Fe and Tb and higher anisotropy field of Tb<sub>2</sub>Fe<sub>14</sub>B led to the enhancement of coercivity and reduction of remanent ratio, which in turn has resulted in lower value of maximum energy product.

Fig.- 5.14 shows room temperature (300 K) hysteresis loop and some minor recoil loops along the demagnetization branch for the sample annealed at 923 K for 3 minutes. In Fig.-5.15, the area of the recoil loops normalized to the area of half of the major hysteresis loops are plotted as a function of the reverse field H. The areas have been extracted by numerical integration of the recoil curves of Fig.-5.14. The development of the loop area is due to the decoupling of the magnetic moment between hard and soft phase. In Fig.-5.15, the recoil area shows a pronounced maximum at the field where the largest number of hard phase grains switch magnetization direction. Recoil loops are small having high recoil permeability. When the reverse field is lower than the critical field magnetization which returns from the demagnetizing field is very close to the starting value. The areas of the loops at these stages are also negligible. As the demagnetizing field approaches the critical field, areas of the loops increase. Near the coercive field area of the loop is highest.

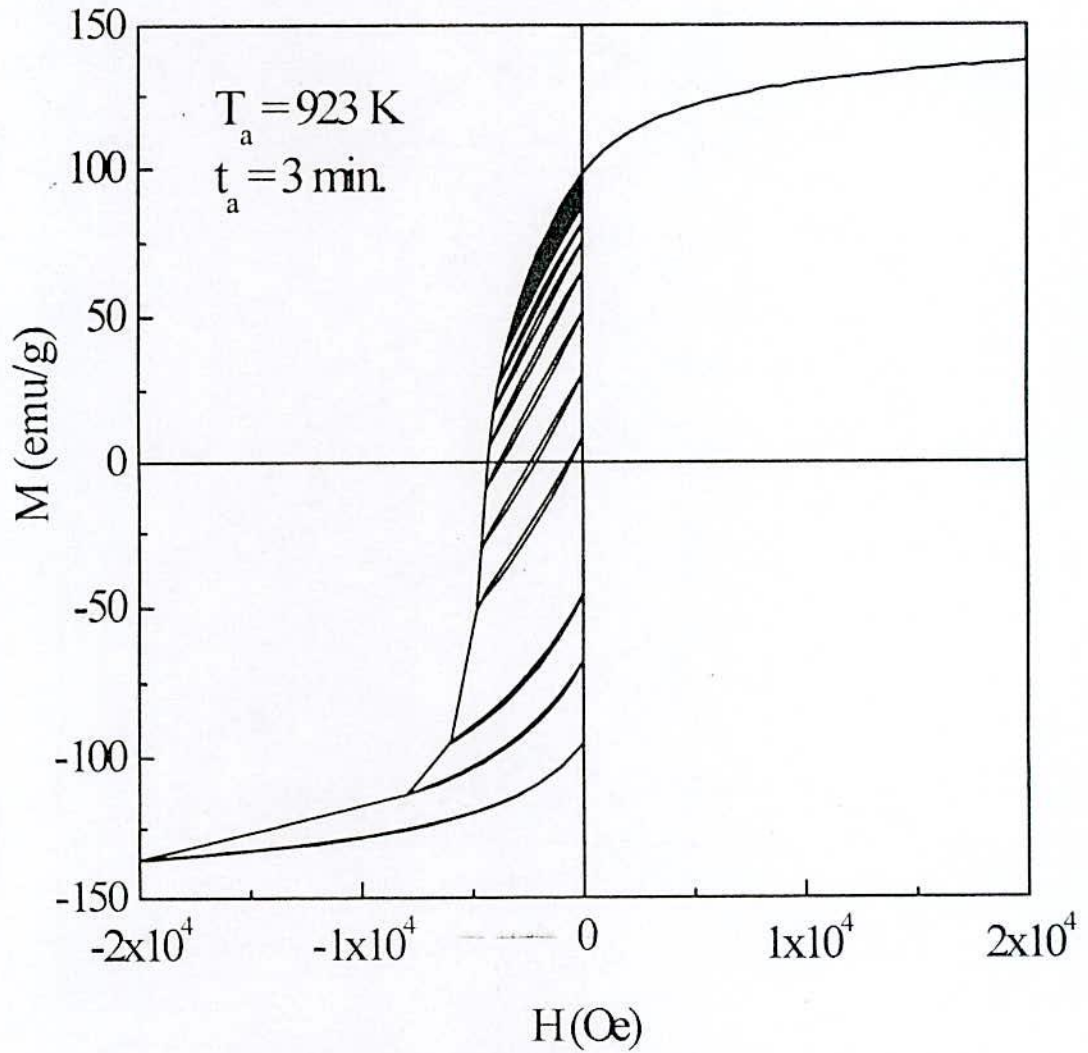


Fig.- 5. 14. Recoil hysteresis loops for the sample annealed at 923 K for 3 minutes.

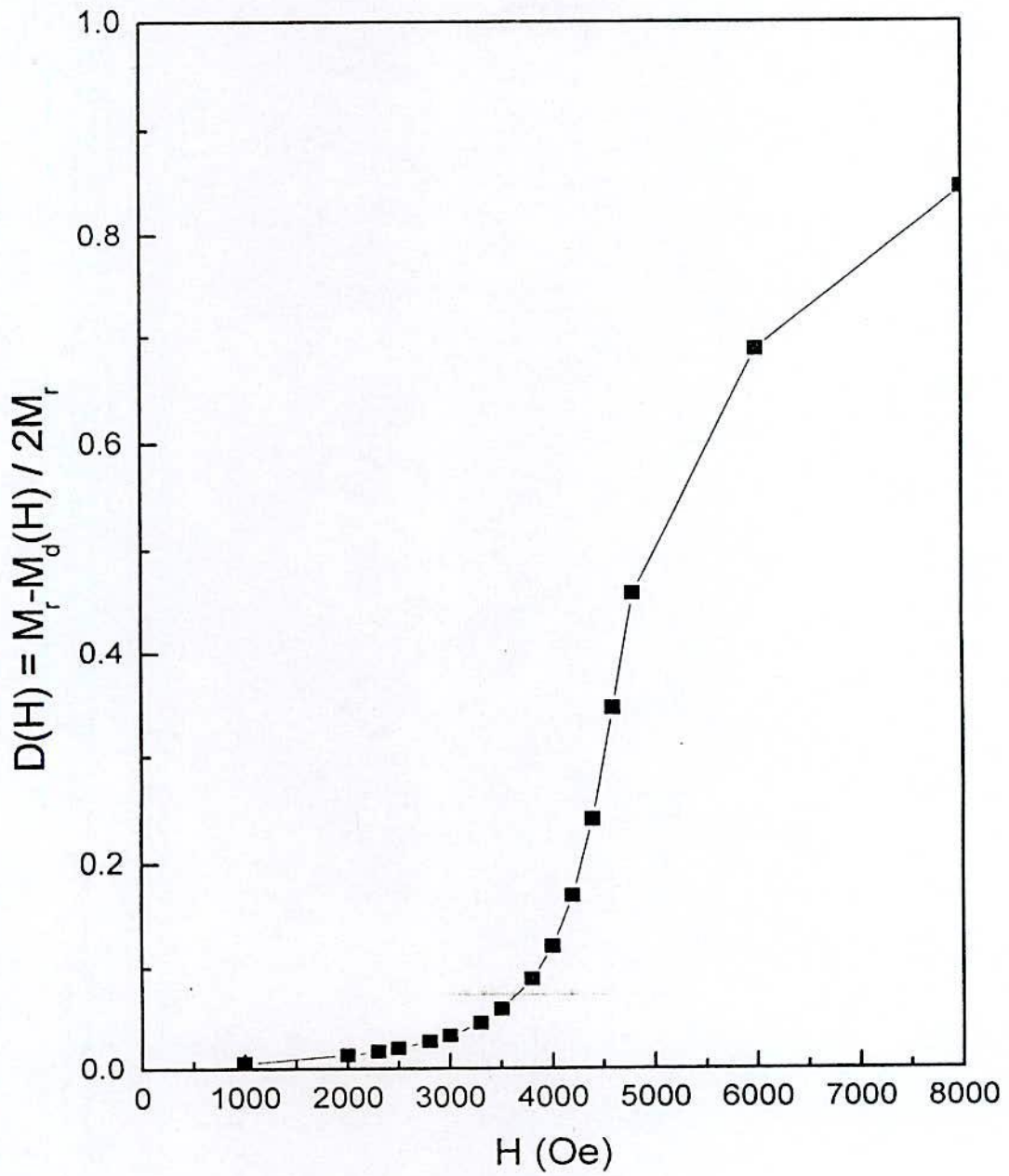


Fig.- 5.15 Variation of irreversible component of magnetization  $D(H)$  with reverse field.



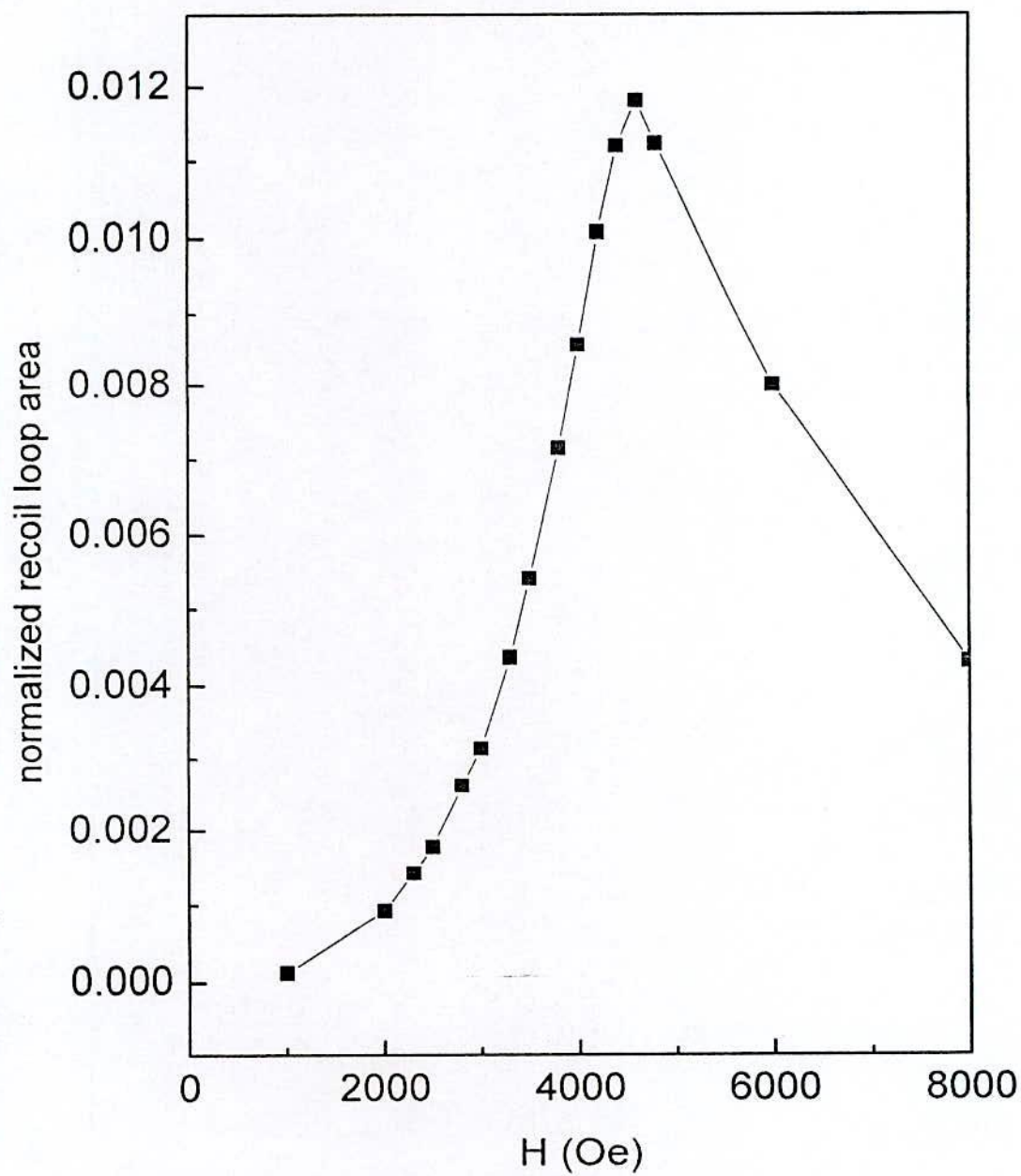


Fig. - 5.16 Variation of normalized recoil area with reverse field

This field amounts to 4600 Oe for the sample annealed at 923 K for 3 minutes. As pointed out by Kang *et. al.* <sup>(5.3)</sup> the peak in the recoil area is coincident with the coercivity of the hard component while the departure from zero recoil area at low reverse fields corresponds to the inter-phase exchange field,  $H_{ex}$ . In Fig. -5.15, the reduced quantity  $D(H) = \frac{M_r - M_d(H)}{2M_r} = -\frac{\Delta M_{irrever}(H)}{2M_r}$  is plotted vs. H, where  $M_d(H)$  is the dc field demagnetization remanence i.e. the remanence acquired after saturation in one *direction* and subsequent application of a dc field H in the opposite direction and  $M_r$  is the saturation remanence. In Fig.-5.15 provide information about the stability of the reversible state and about the critical field of irreversible changes of the magnetization. For the sample annealed at 923 K, the D(H) versus H curve is characterized by relatively sharp change of D(H) at the critical field where onset of irreversible change in the hard phase takes place, which has been obtained from the derivative of the D(H) vs. H curve and found as 4000 Oe. In Fig.-5.16, the normalized recoil area versus field shows a pronounced maximum at the field (4000 Oe), where the largest number of hard phase grains switch magnetization direction. At the critical field, i.e. at the field where onset of irreversibility takes place, the area enclosed by the recoil loop is maximum and recoil loop does not trace the major demagnetization curve.

**CHAPTER – 6**  
**CONCLUSIONS**



## 6.0 Conclusions

The phenomenon of remanence enhancement in isotropic nanocrystalline permanent magnets has been studied since the 1970's. Magnetic initial permeability of nanocrystalline / amorphous ribbon strongly depends on annealing temperatures and times. Short time annealing above the crystallization temperature leads to the improvement of soft magnetic properties and is better than that for long time annealing. The best magnetic properties have been observed for the optimized annealed condition. At lower annealing temperature, enhancement of permeability takes place due to the structural relaxation. Permeability drops to a lower value during the initiation of crystallization. Enhanced initial permeability is of the order of  $\approx 10^{-4}$  and reduction of relative loss factor is of the order of  $\approx 10^{-6}$ , which have been achieved at optimized annealing condition of respective compositions. This has been achieved because at this stage local anisotropy is averaged out by exchange coupling between nanograins embedded in the residual amorphous matrix.

The effect of remanence enhancement is accounted for by the exchange coupling between grains of nanometer size. They derived a relationship between the microstructure and the magnetic properties that predicts how to reach a significant enhancement. Kneller and Hawig also estimated the microstructure parameters of this new kind of material, for example, the distribution of soft-magnetic phase and hard-magnetic phase and the fraction of soft-magnetic phase, indicating the possibility of developing nanocomposite permanent-magnetic materials. Below the model of Kneller and Hawig is presented in a brief way.

A survey on the magnetic properties of some well-known materials of both categories in Table-5.1 indicates that the saturation polarization  $J_s$ , is for most k-materials considerably lower than for many m-materials, whereas the coercivity  $H_{CM}$  of k-materials may exceed, by far the value  $M_s/2$ . Moreover, the best of the k-materials contain about 25wt% or more of a rare earth metal, which add to their price and raises serious problems with respect to chemical stability, while most m-materials are much reactive and rather inexpensive.

Therefore it is tempting to consider composite materials consisting of two suitably dispersed and mutually exchange – coupled phases, one of which is of the k-type thus providing a high enough nucleation field for irreversible magnetization reversal, and the other is an m-type material with  $M_s$  as high as possible, in order to attain a high average saturation. In addition the m-material may envelop the k-phase regions in order to prevent their corrosion.

At first, the critical dimension of the phase are estimated and later on the corresponding models of microstructures are discussed. On that basis, typical magnetic properties of such composites are derived. Finally it is shown how a material of this kind may be realized technologically and that its magnetic behavior corresponds entirely to the predictions of the theory.

A partial substitution of Nd by Tb led to the enhancement of coercive field up to a value of 4.76 k Oe for the sample annealed at 923 K for 5 minutes. Recoil hysteresis loops are characterized by high recoil permeabilities and small recoil loop area which indicates that the samples are exchange coupled. At low temperature, temperature dependence of hysteresis loops are governed by spin reorientation of the easy axis of  $\text{Nd}_2\text{Fe}_{14}\text{B}$  below 200K, field dependence of magnetization is discontinuous at low field leading to constricted hysteresis loop.



## REFERENCES

**CHAPTER-1**

- 1.1 Herzer, G.; "Grain structure and magnetism of nanocrystalline ferromagnets"; IEEE Trans. Magn. 25(1989) 3327-3329.
- 1.2 Herzer, G.; "Grain size dependence of coercivity and permeability in nanocrystalline ferromagnets"; IEEE Trans. Magn. 26(1990) 1397-1402.
- 1.3 S. Manjura Hoque, M. A. Hakim, F. Alam Khan, and M. A. Asgar; "Crystallization behavior and magnetic softness of devitrified Fe-based metallic glasses"; Proceeding of 9<sup>th</sup> Asia Pacific Physics Conference; Hanoi 2004.
- 1.4 S. Manjura Hoque, M. A. Khan and N. Chau; "Ultra-Soft magnetic properties of devitrified  $Fe_{75.5}Cu_{0.6}Nb_{2.4}Si_{13}B_{8.5}$  alloy"; Materials Chemistry and Physics; 101 (2007) 112.
- 1.5 Hakim, M. A. and Hoque, S. M. ; "Effect of structural parameters on soft magnetic properties of two phase nanocrystalline alloy of  $Fe_{73.5}Cu_1Ta_3Si_{13.5}B_9$ "; J. Magn. Magn. Mat.; 284(2004)395.
- 1.6 Hadjipanayis, G. C. and Gong, W.; "Magnetic hysteresis in melt-spun Nd-Fe-Al-B-Si alloys with high remanence"; J. Appl. Phys.; 64(1988) 5559-5561.
- 1.7 Schrefl, T., Fidler J. and Kronmüller, H.; "Remanence and coercivity in isotropic nanocrystalline permanent magnets"; Phys. Rev. B49(1994) 6100-6110.
- 1.8 Manaf A., Leonowicz M., Davies H. A. and Buckley R. A.; "Effect of grain size and microstructure on magnetic properties of rapidly solidified  $Fe_{82.4}Nd_{13.1}B_{4.5}$  alloy"; J. Appl. Phys. 70(1991) 6366-6368.
- 1.9 Coehoorn R., de Mooij D. B., Duchateau J. P. W. B. and Buschow K. H. J. J; de Phys. 49(1988) 669.
- 1.10 Manaf A., Buckley R. A. and Davies H. A.; "New nanocrystalline high-remanence Nd-Fe-B alloys by rapid solidification"; J. Magn. Magn. Mater. 128(1993) 302-306.
- 1.11 Withwanawasam L., Hadjipanayis G. C. and Hause R. F.; "Enhanced remanence in isotropic Fe-rich met-spun Nd-Fe-B ribbons"; J. Appl. Physics; 75(1994) 6646-6648.

- 1.12 Kneller E. F. and Hawig R.; "The exchange-Spring magnet; a new material principle for permanent magnets"; IEEE Trans. Magn. 27(1991) 3588.
- 1.13 Sagawa M., Fujimura S., Yamamoto H., Matsuura Y.; "Permanent magnet materials based on rare earth-ion-boron tetragonal compounds"; IEEE Trans. Magn. Mag-20 (1984) 1584-1589.
- 1.14 Kans K., Lewis L. H., Jiang J. S. and Bader S. D.; "Recoil hysteresis of Sm-Co/Fe exchange spring bilayers"; J. Appl. Phys. 98(2005) 113906(1)-(6).

## CHAPTER-2

- 2.1 Kneller E. F. and Hawig R.; "The exchange-Spring magnet; a new material principle for permanent magnets"; IEEE Trans. Magn. 27(1991) 3588-3600.
- 2.2 Meiklejohn W. H. and C. P. Bean; Phys. Rev., Vol. 102, p. 1413, 1956; Phys. Rev., Vol. 105, p. 904, 1957.
- 2.3 Kneller E. and Y. Khan; J Metastllkde, Vol. 78, p. 825, 1987.
- 2.4 Croat J. J.; J. Magn. Magn. Mat., Vol.24, p. 125, 1981.
- 2.5 Croat J. J., J. F. Herbst, R. W. Lee and F. E. Pinkerton; J. Appl. Phys.; Vol. 55, p. 2078, 1984.
- 2.6 Becker J. J.; J. Appl.. Phys., Vol. 55, p. 2067, 1984.
- 2.7 Buschow K. H. J., D. B. de Mooij and H. M. van Noort; J. Less Common Metals; Vol. 125, p. 135, 1986.
- 2.8 Buschow K. H. J., D. B. de Mooij and R. Cochoorn; J. Less common Metals; Vol. 145, p. 601, 1988.
- 2.9 Cochoorn R., D. B. de Mooij, J. P. W. B. Duchateau and K. H. J. Buschow; J. de Phys.; Vol. 49, p. 669, 1988.
- 2.10 Cochoorn R., D. B. de Mooij, and C. De Waard; J. Magn. Magn. Mat.; Vol. 80, p.101, 1989.
- 2.11 Brown Jr W. F.; Rev. Mod. Phys., Vol. 17, p.15, 1945.
- 2.12 Kondorskij E.; J. Phys. USSR; Vol.2 p.161, 1940.



### CHAPTER-3

- 3.1 Turgut Z., M. Q. Huang, K. Gallagher, S. A. Mayelich and M. E. Mc Henry; J. Appl. Phys. (1997) **81** 4039.
- 3.2 Turgut Z., N. T. Nuhfer, H. R. Pichler and M. E. Mc Henry, J. Appl. Phys., (1999) **85** 4406.
- 3.3 . Dirne F. W. A and M. Brouha, IEEE Trans. Magn., (1988) **MAG-24** 1862.
- 3.4 de Wit H. J., J. Magn. Magn. Mat., (1989) **79** 167.
- 3.5 Yoshizawa Y., K. Yamauchi, T. Yamane, H. Sugihara, J. Appl. Phys. (1988) **64** 647.
- 3.6 Duwez P., R. H. Willens and W. Klement; J. Appl. Phys., (1960) **31** 1136.
- 3.7 Simpson A. W. and D. R. Brandley; Phys. Stat. Sol. (b) (1971) **43** 291.
- 3.8 O' Handley R. C., J. Megusar, S. W. Sun, Y. Hara, N. J. Grant; J. Appl. Phys. (1985) **57** 3563.
- 3.9 Duwez P., J. Am Inst. Metal Eng. (1951) **191** 765.
- 3.10 Duwez P., R. H. Willens, W. Klement; J. Appl. Phys., (1960) **31** 1136.
- 3.11 Duwez P., Trans. Am SOC Met. (1967) **60** 607.
- 3.12 Duwez P., Ann Rev. Mat. Sci. (1976) **6** 83.
- 3.13 Mader S., Nowick As. Appl. Phys. Lett. (1965) **7** 57.
- 3.14 Tsuei C. C., P. Duwez, J. Appl. Phys., (1960) **37** 435.
- 3.15 Yoshizawa Y., S. Oguma and K. Yamauchi, J. Appl. Phys. (1988) **64** 6044-6046.
- 3.16 Yoshizawa Y., K. Yamauchi, T. Yamane and H. Sugihara, J. Appl. Phys. (1988) **64** 6047.
- 3.17 Kojima A., H. Horikiri, Y. Kamamura, A. Makino, A. Inoue, T. Matsumoto; Mat. Sci. Eng. (1994) **A179/A180** 511.
- 3.18 Mizoguchi T., IBM Research report, (1976) **RC 6054**.
- 3.19 Alben R., J. I. Budnic and G. S. Gargill;  $\alpha_{111}$  Metallic Glasses, "American SOC. for metals" (1978) **PP.304**.
- 3.20 Herzer G.; "Handbook of Magnetic Materials; K. H. J. Buschow (ed.), Elsevier Science, Amsterdam, 1997, p.417.

- 3.21 Yoshizawa Y. and K. Yamauchi, "Fe-based soft magnetic alloys Composed of ultrafine grain structure", Mater. Trans. JIM. (1990a) **31** 307.
- 3.22 Hono K. and T. Sakurai, "Atom probe studies of nanostructured alloys", Appl. Surf. Sci. (1995) **87/88** 166.
- 3.23 Hono K., K. Hiraga, Q. Wang, A. Inoue, T. Sakurai, "The Microstructure Evolution of Fe<sub>73.5</sub> Si<sub>13.5</sub> B<sub>9</sub>Nb<sub>3</sub> Cu<sub>1</sub> nanocrystalline soft magnetic material", Acta Metal. Mater. (1992) **40** 2137.
- 3.24 Koster U., M. Schonemann, Blank-Bewersdorff, S. Brauer, M. Sutton and G. B. Stephenson; Mat. Sci. Eng. (1991) **A133** 611.
- 3.25 Warlimont H., Mater. Sci. Eng. (1988) 99.
- 3.26 Herzer G.; In: Proc of Int. Symp. On 3d Transition- Semi Metal Thin Films. Magnetism and Processing (Japan SOC for the promotion of Science, Committee, Sendai, Japan) (1991) **131** 130.

#### CHAPTER-4

- 4.1 Turnbull, IEEE Trans. Magn. (1990) **26** 1397-1402,
- 4.2 Coey J. M. D and H. Sun, J. Magn. Magn. Mater. (1991) **87** L251.
- 4.3 Schnitzke K., L. Schultz, J. Wecker and M. Katter; Appl. Phys. Lett., (1990) **57** 2853.
- 4.4 Foner S., Rev. Sci. Instr. (1959) **30** 548.
- 4.5 Foner S., Rev. Sci. Instr. (1955) **27** 578.

#### CHAPTER-5

- 5.1 E. Kondorskij; J. Phys. USSR, Vol.2, p161, 1940.
- 5.2 Sagawa M., Fujimura S., Yamamoto H. and Matsuura Y.; "Permanent magnet materials based on the rare earth-ion-boron tetragonal compounds"; IEEE Trans. Magn. Mag-20 (1984) 1584-1589.
- 5.3 Kang K. , L. H. Lewis, J. S. Jiang and S. D. Bader, J. Appl. Phys. **98** (2005) 113906.

**PUBLICATION**

---



# NUCLEAR SCIENCE AND APPLICATIONS

Volume 16

Number 1

June 2007

## EDITORIAL BOARD

Chief Editor	:	Dr. Shafiqul Islam Bhuiyan
Members	:	Dr. Farid Uddin Ahmed
	:	Sohela Akhter
	:	Dr. Swapan Kumar Biswas
	:	Dr. Shahana Afroz
	:	Md. Sheher Ali
	:	Dr. S. M. Firoz Hasan
	:	Dr. Md. Saidul Islam
	:	Dr. A. K. M. Abdul Hakim
	Member-Secretary	:



**Bangladesh Atomic Energy Commission**

**Paramanu Bhaban**

E-12/A, Agargaon, Sher-e-Bangla Nagar, Dhaka-1207.

## Variation of Magnetic Properties with Annealing Time of Tb Substituted Exchange-Biased $\text{Nd}_2\text{Fe}_{14}\text{B}/\text{Fe}_3\text{B}$

S. Manjura Hoque<sup>1\*</sup>, Abu Hanif Ansari<sup>2</sup>, Shibendra Shekhar Sikder<sup>2</sup>  
M. A. Hakim<sup>1</sup>, and F. A. Khan<sup>3</sup>

<sup>1</sup>Materials Science Division, Atomic Energy Center, Dhaka-1000, Bangladesh

<sup>2</sup>Department of Physics, Khulna University of Engineering and Technology, Khulna

<sup>3</sup>Department of Physics, Bangladesh University of Engineering and Technology, Dhaka

### Abstract

Hard Nanocomposite samples of the composition  $\text{Nd}_{3.5}\text{Tb}_1\text{Fe}_{76}\text{Cu}_{0.5}\text{Nb}_{1.2}\text{B}_{18.5}$  exhibited exchange-spring behavior for a wide range of annealing temperatures and time. Amorphous flakes have been synthesized by melt spinning system and annealed in the quartz tube under a vacuum of  $10^{-5}$  mbar pressure to observe the variation of magnetic properties with annealing condition. Highest value of coercivity around 4.76 kOe has been obtained for the sample annealed at 923 K for 5 minutes. Recoil hysteresis loop have been measured along the major demagnetization curve to observe the extent of springness for the sample annealed at 923 K for 3 minutes. Recoil loops are small having high recoil permeability. Irreversible component of magnetization was found to have very small value below the critical field.

PACS: 5.50.Ww; 75.60.Jk; 75.60.Ej

**Keywords:** Recoil hysteresis, Exchange spring, Nanostructured materials, Coercivity, Hysteresis loops

### 1. Introduction

Nd-deficient  $\text{Nd}_2\text{Fe}_{14}\text{B}/\text{Fe}_3\text{B}$  based nanocomposite alloys [1-6] are characterized by their exchange-spring behavior resulting in remanent ratio greater than 0.5, which is highly desirable for permanent magnetic materials. Magnetic properties of exchange spring magnets are governed by the soft and hard magnetic phases that develop under appropriate annealing condition. High reduced remanence characteristic to these materials arises from exchange coupling of magnetic moments across the interface between two phases. Besides high reduced remanence such systems possess high energy product  $(\text{BH})_{\text{max}}$  and a reversible demagnetization curve, which has been called as exchange-spring behavior. This causes the magnetic moments of both the phases to remain in the same direction. It has been demonstrated earlier by Knefler and Lawig [1] that the enhancement of remanence and coercivity by this mechanism is mainly governed

by the crystallite sizes of both phases in particular the soft phase, which can be controlled by dopants and/or additives and also by controlling heat treatment. Compared to single phase  $\text{Nd}_2\text{Fe}_{14}\text{B}$ , nanocomposite  $\text{Nd}_2\text{Fe}_{14}\text{B}/\text{Fe}_3\text{B}$  based alloys are economic and corrosion resistant. Various dopants and substituents have been used to enhance the value of coercivity. A partial substitution of Nd by heavy rare earth elements like Tb increases the anisotropy field,  $H_A$  which enhances the coercive field, but decreases strongly the remanence due to its antiferromagnetic coupling between rare earth and the transition metal [2]. Tb addition has previously been used to increase the coercivity of  $\text{Pr}_2\text{Fe}_{14}\text{B}$  due to higher anisotropy field of  $\text{Tb}_2\text{Fe}_{14}\text{B}$  [3].

Studies [4-6] of macroscopic reversible and irreversible magnetic behavior in nano-crystalline exchange coupled two-phase permanent magnetic materials demonstrate relatively steep recoil curves, which possess recoil permeabilities five times greater than

\*Corresponding author